

https://dspace.org/

Potential Source for the Alluvial Gold Deposit in the Kapoeta Area, Eastern Equatoria State, South Sudan

Bali, Francis Khamis Alex

2023-10

University of the Witwatersrand, Johannesburg

https://hdl.handle.net/10539/41961

Bali, Francis Khamis Alex. (2023). Potential Source for the Alluvial Gold Deposit in the Kapoeta Area, Eastern Equatoria State, South Sudan. [Master's dissertation, University of the Witwatersrand, Johannesburg]. https://hdl.handle.net/10539/41961

Downloaded from a DSpace repository. https://dspace.org/

POTENTIAL SOURCE FOR THE ALLUVIAL GOLD DEPOSIT IN THE KAPOETA AREA, EASTERN EQUATORIA STATE, SOUTH SUDAN

By

Francis Bali

(1606415)

A Dissertation submitted to the Faculty of Science, University of the Witwatersrand, in fulfilment of the requirements for the degree of Master of Science.



Supervisor: Prof. Judith Kinnaird
Co-supervisor: Prof. Tsehaie Woldai

School of Geosciences
University of the Witwatersrand
Private Bag 3
2050 Wits
South Africa
2023
2023, Johannesburg, South Africa

Declaration

I, Francis Bali, declare that this dissertation is my own work. It is being submitted for the Degree of Master of Science at the University of the Witwatersrand, Johannesburg. It has not been submitted before for any degree or examination at any other Institution of high learning.



Francis Bali

On the 27th day of October 2023 at Braamfontein, Johannesburg

Abstract

This study concentrates on the integrated approach of applying geochemical, and remote sensing data combined with field investigation to understand the source of the alluvial gold deposit in the Kapoeta area.

The use of an integrated technique approach proves effective in mapping and outlining areas of potential gold mineralisation in Kapoeta. Kapoeta has been known for its endowment of gold deposits for quite some time. Landsat-8 (OLI) and SRTM-DEM satellite images were employed during this study to map lithological units and highlight areas of hydrothermal alteration and structural trends in Kapoeta to understand the potential source for the widely distributed alluvial gold in the area. The several image-processing techniques employed were effective in mapping the lithological units and outlining the major structural trends in the area. Mapping the hydrothermal alteration zones was challenging because of the overburden that masks most parts of the Neoproterozoic juvenile metavolcano-sedimentary sequences. Secondly, the vegetation cover is another factor affecting the mapping of the lithological units around the Didinga Hills and Dongotona mountains. Structural mapping identified four main trends N-S, NNW-SSE, NW-SE, and NE-SW. The image interpretation, together with geochemical occurrence and anomaly map showing Cu, Co, Ni, and Cr, shows that N-S and NNW-SSE are the potential controls on mineralisation in the area.

The whole-rock geochemical data plotted on the TAS discrimination diagrams shows that the rocks analysed are dominantly tholeiitic with minor calc-alkaline units. Trace elements normalised to the primitive mantle show low concentrations of Zr, Hf, Nb and Ta. The REE normalised chondrite values indicates general enrichment of LREE elements relative to HREE with a negative Eu anomaly. On the tectonic discrimination diagrams, the results indicate that the rocks of Greater Kapoeta belong in a marine environment related to a spreading centre, oceanic island, oceanic ridges, and floor. The distribution of Cu, Co, Cr and Ni and their high concentration suggest that these elements are the potential pathfinders for gold in the area.

The study concludes the following: Based on the remote sensing, field observations and geochemical data indicates that the gold mineralisation of Kapoeta is orogenic in nature with a strong element of epigenetic characteristics, however, a syngenetic origin cannot be ruled out. The host lithologies may vary from quartz veins to schists, amphibolites, quartzo-feldspathic gneisses, and ultramafics and the marbles related to the N-S, NNS-W-SSE and NW-SE trending shear zones that limit the greenstone belt.

Dedication

I dedicate this work to my Late mum Edina Poni Martin and my beloved Wife Alma A. Gillo without whom I would never reach this far……

Acknowledgements

My sincere gratitude and acknowledgement in the first place is directed to the following personalities: To Prof. Judith Kinnaird, who gave me the opportunity to join this programme. To Prof. Tsehaie Woldai, the co-supervisor for this project, thank you for all the valuable time you dedicated to discussing several aspects of this project and the valuable contribution you made based on your expertise in geological remote sensing, image interpretation and structural analysis, I wish our path cross again in the nearest future.

I am generally greatly indebted to all the members of the geology and mining department at the University of Juba who directly or indirectly contributed to the success of this work. Special gratitude goes to Thomas Oromo, the head of the department of geology and mining, the late Joseph Lagu, who passed on shortly before the completion of this report, and Abure Pakistano for their support during field work. I would like to extend my gratitude further to the late Dr David Evuk, who unfortunately also passed on in the same month when this work was about to be completed. Your fruitful discussion on the regional geology of East and NE Africa and tectonics was commendable. Big thanks to Prof Cosmas Pitiya Kujjo for his contribution and support. The dean of the School of Natural Resources and Environmental Studies, Prof Salah Jubara, whose efforts made it possible for me to get all the necessary documents to visit the Kapoeta area. Dr Lazarus and Denis Abbe, thank you for your time, effort, and aid with the use of some remote sensing software.

I am very grateful to Dr Andu Ezibon for his support that made this project possible, and to the entire staff of the ministry of the Mining, Republic of South Sudan; in particular, I wish to mention James Kundu, Michael Carlo, and Bol John for their support with reference materials about the area. Gratitude is also directed to H.E. Louis Lobong Lojore, the governor of Eastern Equatoria State, who, without hesitation, gave the security clearance and approval for conducting the fieldwork in Kapoeta. My gratitude is also extended to the government of Kapoeta East, Kapoeta South, and Budi counties for the administrative support. Special thanks go to the commissioner of Kapoeta South and the chief in the area, Mr. Juma, the county director at Narus, Simon Lomuria and Kal Peter for their tireless effort in coordinating with the chiefs and natives during the field visits. I would also like to extend my gratitude to the staff of the school of Geosciences, who directly contributed to this project's success, from sample preparation to geochemical analysis. Special gratitude is directed to my family for putting up with my travels and absence; to my dear friends, Victoria Cosmas, for your financial support to start this journey, Subhy Jogot, Gabriel Matut and Baba James for emotional support. Special thanks also go to the family of El Tayeb Mahmoud, the family of Hussein, Prof El Hadi Adam, Al Tayeb Shaffi, Mohammed Bashar, and the Sudanese community with whom I had a wonderful time in Johannesburg. let the brotherhood continue.

Contents

Declaration ..... **I**
Abstract ..... **II**
Dedication ..... **III**
Acknowledgements ..... **IV**
Contents ..... **V**
List of Figures ..... **VIII**
List of Tables ..... **XIII**
Nomenclature/List of Abbreviations and Symbols ..... **XIV**
Chapter 1 ..... **1**
Introduction **1**
1.1 Background 1
1.2 Aims and Objectives of the project. 2
1.3 Literature Review 2
Chapter 2 The Study Area **4**
2.1 Location and Accessibility 4
Chapter 3 Regional and Local Geology **5**
3.1 Introduction 5
3.2 Regional Geology 6
3.3 Geology of the Study Area 9
3.3.1 Archaean Basement Complex 9
3.3.2 Karasuk Supergroup 10
3.3.3 Alkaline Intrusions of E and NE Africa 11
3.3.4 Tertiary Extrusive Rocks 12
3.3.5 Umm Ruwaba Formation 12
3.3.6 Superficial Deposits? 13
Chapter 4 Methodology **14**
4.1 Introduction 14
4.2 Remote Sensing and Interpretation 14
4.3 Pre-processing of satellite images 15
4.4 Image Processing 16
4.4.1 Colour Composite Images 16
4.4.2 Band Ratio 16
4.4.3 Principal Component Analysis (PCA) 18
4.4.4 Minimum Noise Fraction (MNF) 20

4.4.5 Supervised Classification 20
4.4.6 SRTM-DEM 20
4.4.7 Lineament Extraction 21
4.5 Field Work and Sampling 23
4.6 Geochemistry 23
4.7 Reinterpretation of Data 23
Chapter 5 Results 24
5.1 Remote Sensing and Interpretation 24
5.1.1 Colour Composite Images 24
5.1.2 Band Ratio 26
5.1.3 Principal Component Analysis (PCA) 27
5.1.4 Supervised Classification 29
5.2 Geological mapping 29
5.2.1 Undifferentiated Basement Complex 30
5.2.1 Gneisses 32
5.2.2 Amphibolites 33
5.2.3 Schists 34
5.2.4 Meta-Rhyolite 35
5.2.5 Marbles 36
5.2.6 Quartzite 37
5.2.7 Quartz Veins 38
5.2.8 Gabbro 38
5.2.9 Acidic Intrusions 39
5.2.10 Basalts and Rhyolite Bodies 40
5.3 Structural Interpretation 40
5.3.1 Lineament Extraction 40
5.3.2 Folds, Faults and Joints 42
5.3.3 NNW-SSE and N-S Structures 43
5.3.4 NW-SE Trends 44
5.3.5 NE-SW Structures 46
5.4 Mineralisation 48
5.4.1 Placer Gold 49
5.4.2 Primary Gold 50
5.5 Geochemistry 53
5.5.1 Whole-rock Geochemistry 53
5.5.2 Trace Element Variations 58

5.5.3 Magmatic Series Determination 62
5.5.4 Tectonic Classification 63
Chapter 6 Discussion and Conclusion 65
6.1 Introduction 65
6.2 Remote Sensing and Image Interpretation 65
6.2.1 Lithological Mapping 65
6.2.2 Lineament Mapping 68
6.2.3 Hydrothermal Alteration Zone Identification 69
6.2.4 Regional Correlation and Tectonics 70
6.3 Field Relationships and Regional Geology 72
6.4 Geochemistry 76
6.4.1 Protolith of the Metavolcano-sedimentary Assemblages 76
6.4.2 Pyrite Enrichment 78
6.4.3 Pathfinder elements for the gold occurrence 79
6.4.4 Tectonic Model 82
6.5 Gold Mineralisation 85
6.5.1 Origin of Gold in Greater Kapoeta 85
6.5.2 The implication of gold mineralisation in the Didinga Hills 87
6.5.3 Source of Metal 88
6.5.4 Source of Fluid 88
6.5.5 Structural Control 88
Chapter 7 Conclusion 90
7.1 Recommendation 91
References 92
9.1 Appendix II: List of samples and their locations 112

List of Figures

Figure 2.1: Map showing the location of South Sudan on the African Continent. The yellow square shows the study area and the area shaded in green is the outline of the Karamoja region of NE Uganda. 4

Figure 3.1: Map showing the extent of the Saharan Metacraton, the area shaded; the boundary between Arabian Nubian Shield and Sahara Metacraton is defined by the Keraf–Kabus–Sekerr suture; the Oubanguides orogenic Belt separates the Sahara Metacraton from the Congo Craton to the south. (After Abdelsalam et al., 2002). 6

Figure 3.2: Regional map outlining the major lithological units and major structural trends in East Africa (modified after Vail 1988; update based on Belgian Geologic al Survey 1982; Westerhof et al., 2014 maps). 8

Figure 4.1: Flow Chart illustrating the satellite image processing procedure. 15

Figure 4.2: Landsat 7 ETM band ratio result (A) Band ratio 4/2, (B) band ratio 6/7, (C) band ratio 6/5. 18

Figure 4.3: PCA pan-sharpened single bands **(A)** PCA-2 bright reflections are alluvial fans around the mountains, and unconsolidated sediment, dark colour reflection to the north-east are the extrusive igneous bodies **(B)** PCA-4, yellow demarcation is ultrabasic-basic rocks and marbles, blue is an alluvial fan, and unconsolidated sediments **(C)** PCA-5 highlighted in red are ultramafic, gabbro and rhyolite, green highlights are vegetation. 20

Figure 4.4: Flow chart showing the workflow for lineament extraction. 21

Figure 4.5: Landsat 8 OLI pan sharpened PCA 1 showing **(A)** visual interpretation lineaments extraction and **(B)** Automatic lineaments extraction. 22

Figure 5.1: Landsat 8 OLI image Band combination 432 in RGB natural colour composite; Green indicates vegetation cover; **(A)** brown to dark brown to the northeastern corner of the map indicates the extrusive rocks; **(B)** the ultramafics and metavolcanic bodies have the same tone; **(C)** the bright yellow colour represents undifferentiated gneisses and schists covered by sediments; **(D)** alluvial fans shown as bright at the foot of the outcrops; **(E)** Umm Rwaba Formation is shown in light or bright colours to the NW of Didinga Hills; **(F)** Undifferentiated basement complex**: (G)** Older Basement..... 24

Figure 5.2: Landsat 8 OLI image Band combination 257 FCC in RGB; **(A)** brownish colour highlights extrusive bodies; **(B)** basic-ultrabasic bodies; **(C)** undifferentiated gneisses and schists; **(D)** White = alluvial sediments; **(E)** Yellowish to orange = Umm Rwaba Formation; **(F)** Blue and purple indicates undifferentiated Basement Complex rocks; **(G)** Older basement; **(H)** Green represents vegetation cover. 25

Figure 5.3: Landsat 7 ETM image band combination 741 in RGB 25
Figure 5.4: Landsat 7 ETM image band combination 257 in RGB 26
Figure 5.5: Landsat 8 image 7/5: 6/4: 4/2 band ratio composite in RGB; **(A)** Dark blue with the hue of red defines the extrusive bodies; **(C)** Basic body **(D)** Green vegetation; light purple Karasuk Supergroup assemblages; **(E)** orange corresponds to Old Basement Complex **(F)** pinkish to orange corresponds to undifferentiated gneisses **(G)** Umm Rwaba Formation **(H)** alluvial sediments. 27
Figure 5.6: Landsat 7 ETM Principal Component Analysis PC2, PC5, PC4 in RGB; **(A)** Green = Extrusive bodies; **(B)** purple defines basic and ultrabasic rocks; **(C)** reddish to reddish-orange defines metasedimentary rocks; **(D)** vegetation cover appears aqua or turquoise; **(E)** Yellow = alluvial sediments. 28
Figure 5.7: Landsat 8 MNF combination in RGB 234; **(A)** Extrusive bodies are displayed in bright colour pink **(B)** light blue=Umm Rwaba **(C)** Navy blue mixed with maroon=undifferentiated gneisses **(D)** Old basement complex; **(E)** shades of green=vegetation cover. 28
Figure 5.8: Supervised classification of Landsat 8 showing seven classes of geological features and vegetation in green. 29
Figure 5.9: Geological map of the study area showing main lithological units of the Karasuk Supergroup (KSG). The boundaries are hypothetical due to the sedimentary cover. Map created using Landsat 8 OLI image of the study area, field data (modified after Belgian Mineral Exploration Project (1983). 30
Figure 5.10: Field photographs showing typical outcrops in the Didinga Hills **(A)** Massive rounded dome-shape cliffs of the Didinga Ranges **(B)** diorite southeast of the Didinga ranges along the road to Lotuke **(C)** Charnockite fragment with very coarse-grained texture behind the school in Isoke **(D)** Massive dome-shape outcrop of either Charnockite or the associated rocks in the area around Isoke. 31
Figure 5.11: Field photos of some of the variety of gneisses observed in Kapoeta **(A)** Quartz-feldspathic gneiss with amphibolite band along the Kapoeta-Narus road in Kawokono **(B)** and **(C)** Quartz-feldspathic gneiss in Khor Jeep with some elements of migmatisation **(D)** Biotite gneiss south of Singatha river around Namurunyang. 32
Figure 5.12: Samples of amphibolites derived from an igneous protolith **(A)**. Amphibolite contains almandine garnet **(B)** Meta-andesite **(C)** meta-basalt with boudinage structure south of Buno stream **(D)** amphibolite with garnet 33
Figure 5.13: Field images of the variety of amphibolite **(A)** and **(B)** Amphibolite capped unconformably by marble at Nakwasigira **(C)** Thin bed of amphibolite approximately 5 m wide associated with banded marble east of Moruarangani Hill. 34

Figure 5.14: Field photos showing **(A)** Chlorite schist around Buno streams along the Kapoeta-Narus highway and **(B)** Quartzo-feldspathic schist around Anakanak streams east of Kapoeta town. 35
Figure 5.15: Field photo showing meta-rhyolite fragment about 150 m east of Moruarangani Hill, Namurunyang area..... 36
Figure 5.16: Field photos showing banded marble of Kapoeta; **(A)** Marble with thin layers of amphibolite **(B)** Banded marble around Namurunyang; **(C)** Marble with a boudin of quartz **(D)** Evidence of shear effect in marble **(E)** Tofani (Swiss cheese-like weathering) east of Moruarangani Hill; **(F)** Marble lying unconformably on amphibolite near Nakwasigira. 37
Figure 5.17: Field photos of vein quartz **(A)** Quartz vein showing pyrite and oxidation from Moruarangani area a few kilometres south of Kapoeta town **(B)** quartz vein with pyrite after slicing the sample for thin section. 38
Figure 5.18: Field photo showing boulders of massive gabbro 2 km south along Buno stream bed. .. 39
Figure 5.19: Field photos of volcanic rocks **(A)** Basaltic lava flow at Loyoro stream **(B)** Rhyolitic lava with a green mineral forming a phenocryst or amygdale **(C)** a contact between basalt overlying rhyolite at Loyoro stream **(D)** Rhyolitic boulder with vesicles at Napeikeng Hill about two kilometres behind the county headquarters **(E)** outcrops of basalt west of Narus around Lapachol **(F)** Rhyolite boulder with quartz. 40
Figure 5.20:Rose diagram showing the main structural trends mapped using **(A)** Visual interpretation extraction method from SRTM hillshade image **(B)** Visual interpretation from PCA 1 HVS enhance Landsat 8 Image **(C)** PCA 1 HVS sharpened automatic extraction. 41
Figure 5.21: Field photos showing fold structures in banded marble around Moruarangani, approximately 10 km south of Kapoeta town. 43
Figure 5.22: Geophysical data of South Sudan showing the study area **(A)** Bouguer anomaly acquired from a horizontal gradient in the northeast-southwest direction indicating northwest-oriented geological structures; **(B)** Basement topography determined from employing an analytic signal to gravity data. Locations of the Central African Shear Zone (CASZ) and the Aswa Shear Zone are shown as study areas in the yellow box; MG: Muglad Basin; Melut Basin (After Kujjo et al., 2019). Near-surface basement areas are highlighted in red, and deeper segments are defined by blue. 46
Figure 5.23: SRTM-DEM map showing major structures and trends in the Greater Kapoeta area with the sun elevation angle at 35°; **(A)** Hill-shade from illumination from 315° (NW-SE); **(B)** illumination direction 45° (NE-SW); **(C)** illumination trend 90°(E-W); **(D)** illumination direction 360° (N-S)..... 48
Figure 5.24: Field photographs showing workings /activity of the artisanal mining of alluvial gold deposits **(A)** Artisanal mining pit at Kaitap **(B)** site where overburden has been removed for panning **(C)** Two Toposa girls panning gold at Buno stream bed **(D**) shows gold nuggets in the red square

recovered from alluvial sediment from Buno stream **(E)** overburden and basement rocks **(F)** Open pit where the overburden is recovered using an excavator pan with the Didinga Hills on the horizon **(G)** Three Toposa girls in Kawokono recovering sediments deposited between marble boulders to be panned for gold. 50
Figure 5.25: Landsat colour composite image of Kapoeta showing the occurrence and anomalies of Cu, Zn, and Cr elements. 51
Figure 5.26: Primitive mantle-normalised trace element plots of amphibolites of Kapoeta (normalisation values after Sun and McDonough, 1989). 58
Figure 5.27: Multi-element plot of trace elements relative to primitive mantle normalised data based on McDonough and Sun 1995. AN-1A=amphibolite; B-3= amphibolite; B-5= amphibolite; B-10= amphibolite; B-12= amphibolite; B-22= amphibolite; BUN-2= amphibolite; B-14= Gabbro. 59
Figure 5.28: Chondrite normalised REE plots for the various rock types **(A)** Chondrite normalised REE for the amphibolites **(B)** Chondrite normalised diagram for the schists. **(C)** Chondrite normalised REE metavolcanics (normalised factors after Nakamura, 1974). 61
Figure 5.29: Discrimination diagrams showing the affinities of the analysed samples **(A)** AFM diagram of Irvine & Baragar, 1971; **(B)** SiO_2-K_2O diagram of Peccerillo and Taylor 1979; **(C)** The A/NK versus A/CNK diagram (Shand, 1943) **(D)** Molar Na_2O – Al_2O_3 – K_2O ternary diagram. 62
Figure 5.30: The chemical classification and nomenclature of plutonic rock using the total alkalis versus silica **(A)** Total Alkali-Silica diagram (TAS) Cox et al. (1979) **(B)** Total Alkali-Silica (TAS) diagram (after Le Bas et al. 1986) **(C)** FeOt – MgO ternary plot that serves to discriminate between calc-alkaline and tholeiite series **(D)** La/10 Y/15 and Nb/8 discrimination ternary diagram (after Cabanis and Lecolle 1989). 63
Figure 6.1: Landsat 8 OLI image band combination 457 in RGB for hydrothermal zone mapping 70
Figure 6.2: Schematic diagram suggesting the evolution of the East African Orogen (Arabian Nubian Shield) (After. Kröner and Stern, 1994). 74
Figure 6.3: **(A)** Geological map showing Aswa Shear Zone and the related structures in northeast Uganda produced from the structural analysis of airborne geophysical data and geological maps published by Westerhof et al. (2014) and Nyakecho and Hagemann (2014) showing the distribution of various lithological units. **(B)** 3D illustration depicting E–W to NE–SW shortening that accompanied Neoproterozoic oblique collision between East and West Gondwana that led to the evolution of the Aswa Shear Zone as an NW-trending sinistral strike-slip shear zone and the related NW-SE (after: Katumwehe et al., 2015). 75
Figure 6.4: Discrimination diagram to infer the tectonic setting of the metavolcanic of Greater Kapoeta according to **(a)** Mullen (1983) **(b)** Pearce et al. (1977). 77

Figure 6.5: Upgrading of arsenic in pyrite and arsenopyrite. Initial fluids have 100 ppm As and ten mol % CO_2. Fluids were equilibrated with sulphur-bearing basalt before reacting with pyrite ores (initial pyrite with an As:S ratio of 0.01). The solid line represents arsenic concentrations in pyrite, and the dashed line, (As) concentrations in arsenopyrite (Xing et al. 2019). The maximum amount of Au for corresponding arsenic concentrations in pyrite is plotted based on the empirical solubility limit of Reich et al. (2005). 80
Figure 6.6: Schematic tectonic setting of orogenic and other gold deposit types. The orogenic gold deposits may be hosted in metamorphosed fore-arc and back-arc terranes of active continental margins and along the sheared margins to continental arc batholiths (Goldfarb & Groves 2015). 83
Figure 6.7: Cross-sections through the Northern Mozambique belt. (Modified from Shackleton, 1986) 84

List of Tables

Table 3.1: Simplified major litho-stratigraphic units of study area. 9
Table 3.2: Rock types of Karasuk Supergroup from South Sudan and Uganda 11
Table 4.1: Landsat 8 OLI and Landsat 7 ETM spectral band characteristics used in the study (USGS) . 14
Table 5.1: Main tectono-thermal events registered in South Sudan (Hunting 1976) 42
Table 5.2: List of major oxides and Trace elements concentration result of the selected samples of metavolcano plutonic rocks from the Kapoeta area. South Sudan..... 55
Table 5.3: Rare Earth Elements (REE) of fourteen (14) samples from Kapoeta Area 57
Table 6.1: Basic statistics of trace element concentrations of selected metals in analysed samples from Kapoeta. 81

Nomenclature/List of Abbreviations and Symbols

ANS: Arabian Nubian Shield

EAO: East African Orogeny

DEM: Digital Elevation Model

ETM: Enhance Thematic Mapper

GTK: Geologian Tutkimuskeskus (Finnish: Geological Survey of Finland)

ICP-MS: Inductively Coupled Plasma Mass Spectrometry

MB: Mozambique Belt

MG: Muglad Basin

MNF: Minimum Noise Fraction

MT: Melut Basin

OLI: Operational Land Imager

PCA: Principal Component Analysis

REE: Rare Earth Elements

SRTM: Shuttle Radar Topography Mission

TIRS: Thermal Infrared Sensor

XRF: X-Ray Fluorescence

Chapter 1 Introduction

1.1 Background

Gold deposits in metamorphic terranes can be classified as orogenic or reduced intrusion-related gold deposits (Groves et al., 1998; Groves et al., 2003). Orogenic gold deposits dominantly form in greenstone belts, at or above the brittle-ductile transition, with weakly reduced, low-salinity fluids and with near-neutral pH values at approximately 300°C (Groves et al., 1998; Groves et al., 2005; Tomkins 2013). Current issues in the study of gold deposits include the source of the ore-forming fluids, the precise tectonic setting and age of mineralisation, and the specific depositional mechanisms for gold (Groves et al., 2003; Tomkins, 2013). The first two controversies are mainly due to the abundance of isotope and fluid inclusion data (Goryachev and Pirajno, 2014; Molnár et al., 2016) and the lack of ore minerals subjected to high-precision geochronological analysis (Harlan et al., 2017). However, information about the transport and deposition of gold and its fluid evolution can be obtained using detailed petrogenetic analyses and trace element data of pyrite (Craig et al., 1998; Zhang et al., 2014). On the other hand, gold morphology and chemistry and any inclusion can tell the origin of the deposit; it will not indicate where the gold was transported from.

Gold occurrences have been reported from several localities of the Precambrian Basement-occupied region of Equatoria in South Sudan (Unpublished report: Hunting, 1980; Belgian Mineral Exploration Mission 1982). The work of the Belgian Geological Survey Mineral Exploration Mission in the late 1970s and early 1980s identified several placer gold deposit sites. Placer deposits represent important depositories of the Earth's crustal endowment and extracting them contributes significantly to global gold output (Youngson et al., 2006). The Witwatersrand gold deposit, for example, is hosted in a quartz pebble conglomerate. However, identifying the source and potential host rock for the placer gold mineralisation in the area is equally important.

This study is mainly focused on the eastern side of Kapoeta, covering parts of Kapoeta's south and east county and the aims and objectives are listed below. Indigenous and non-local artisanal miners have been involved in gold mining activities for years. Their activities focus on the placer gold deposits from the riverbeds and those deposited in the plains. There are no documented reports of how much gold is produced annually and how long it has been produced. Based on this fact, it is impossible to quantify the local diggers' volume of gold production from this region over the years. However, the Belgian Geological Survey Mineral Exploration (1980) estimates that artisanal miners' gold produced from this region from the placer deposit between 1979 to 1983 amounts to approximately 100-200 kg per annum. As for the whole country, one of the main factors is the recurring civil wars in the region since

1955, which have hampered any systematic geological mapping of the country and limited any monitoring policy to work for artisanal activities. Other factors include the absence of meaningful exploration bodies and the subsequent development of industrial-scale mining in the area.

1.2 Aims and Objectives of the project.

The study aims to identify the potential source for the alluvial gold mineralisation in the Kapoeta area using an integrated geology approach and remote sensing techniques. Special attention will be paid to the meta volcano-sedimentary assemblages. The objectives of the study are: (a) To conduct geological mapping of the study area, (b) To document structural elements and their dynamics in the area, (c) To undertake a petrographic study of selected vital rock types, d) To conduct a whole-rock geochemical analysis of the various lithological units in the area and to understand the potential source rock for gold mineralisation, and (d) To establish the nature and character of the mineralisation and its structure setting.

1.3 Literature Review

The geology of the study area is poorly understood. Limited geological investigations exist -which is attributed to the following reasons: (I) the protracted civil war prior to the independence of the country in 1955, hinder geological operations to be carried out in the area, and (II) the remote and lack of good roads in this part of Sudan (before independence) made it impossible to access the area from Juba, the then regional capital of the southern region.

Hunting (1976) studied the rocks of the eastern extremity of South Sudan and referred to these lithologies as the Karasuk Supergroup, and their extent northwards, Almond (1969) described this unit as metamorphosed to amphibolite facies. The work of the Belgian Mineral Exploration Mission of late 1980s was the first attempt to study this region's geology and mineral potential. It serves as the basis for understanding the geological framework of this area. The Belgian Mineral Exploration Mission (1979-1985) produced a geological map identifying several lithologies mainly associated with the Karasuk Supergroup, Nubian Sandstone Formation, Umm Rwaba Formation, and the Tertiary extrusive rocks.

An exploration project by the Belgian Geological Survey (1979-1983) produced a geological map of the area on a 1:250,000 scale (Unpublished report: Belgian Geological Survey Mineral Exploration Mission 1983). The map covers approximately 11,000 km^2. The project began with stream sediment geochemistry and a detailed assessment of previously traced mineralisation of economic interest. The overall objective was to assess the mineral potential of the region. The expedition discovered alluvial and eluvial gold occurrences and other metal anomalies such as copper, chromium, and cobalt. In a

recent review, an overview of gold systems in Uganda by Nyakecho and Hagemann (2014) described the gold occurrence of the Karamoja belt, a shared environment with Kapoeta.

Chapter 2 The Study Area

2.1 Location and Accessibility

The study area is situated at the southeastern extreme of South Sudan which falls within the Eastern Equatoria region of Equatoria (Figure 2.1). It lies between latitude 4°10'0"- 4°45'0'' N and longitude 33°00'0"- 34°00'0" E, occupying an area of more than 1000 Km^2. The area covered by this study includes Greater Kapoeta, Didinga Hills and Dongotona mountains. The area can be easily access by plane or road from Juba or Kenya through Nadapal-Kapoeta highway. Accessibility to the study sites for sample collection was limited by insecurity from the cattle raiders, thorny bushes, and bad roads.

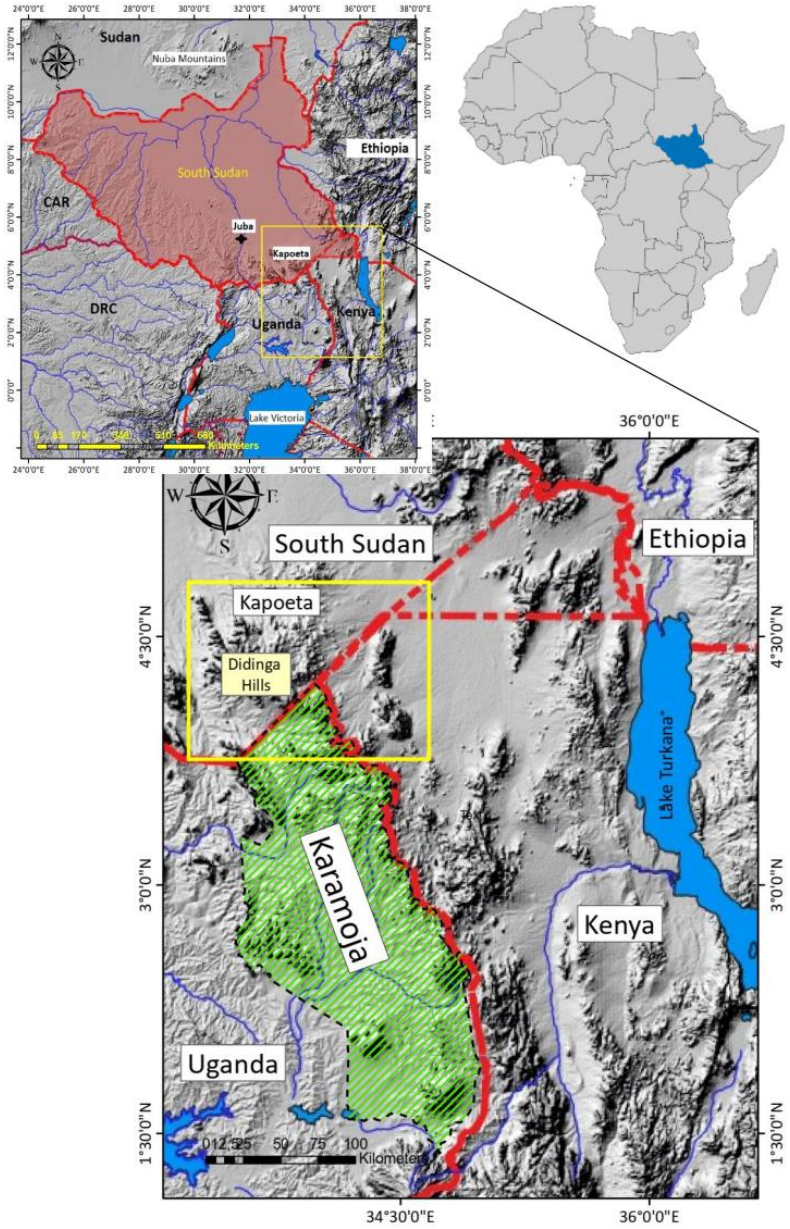

Figure 2.1: Map showing the location of South Sudan on the African Continent. The yellow square shows the study area and the area shaded in green is the outline of the Karamoja region of NE Uganda.

Chapter 3 Regional and Local Geology

3.1 Introduction

The Precambrian basement of East Africa consists of the Archean reworked pre-Neoproterozoic crust known as the Sahara Metacraton (Abdelsalam et al., 2002) to the northwest, occupying the area northeast of Uganda, northwest Kenya, and most of South Sudan Basement Complex stretching westward beyond the Aswa Shear Zone and the juvenile Neoproterozoic East African Orogenic Belt terranes to the east (Figure 3.1). These two distinct terranes are separated by north-trending arc-continental lithospheric-scale suture zones (Keraf–Kabus–Sekerr Suture) resulting from Neoproterozoic collisional events with the Saharan Metacraton (Figure 3.1) (Abdelsalam et al., 2011). Though geological, geochronological, and isotopic data are scarce from this part of the Metacraton (south-eastern extremity of South Sudan), Abdelsalam et al. (2002) argue that they are grossly like those from the northern part of the Metacraton. Along this boundary, high-grade metamorphic rocks of the Saharan Metacraton are juxtaposed against low-grade metavolcano-sedimentary juvenile Neoproterozoic rocks of the East African Orogen (Kuster et al. 2008). The southern boundary of the Sahara Metacraton to the Congo Craton is poorly mapped; however, it has been proposed to partially coincide with the Aswa Shear Zone (Unrug, 1996; Abdelsalam et al., 2002). The Saharan Metacraton is characterised by medium to high-grade metasedimentary rocks, gneisses, migmatites, and smaller exposures of granulites, but low-grade volcano-sedimentary rocks are not uncommon (Abdelsalam, 2002). The occurrence of low-grade volcano-sedimentary sequences within the medium-to high-grade gneissic terranes has been regarded as problematic in that the former are like those of juvenile Neoproterozoic rocks of the Arabian-Nubian Shield (Abdelsalam et al., 2002). Vail (1983, 1985) proposed separating these exposures from the Arabian-Nubian Shield. Two structural orientations dominate the Saharan Metacraton: an older ENE–WSW trend and a younger N–S trend (Abdelsalam et al., 2002). Most of these trends are reported in Sudan, Central Africa, Chad and probably as far as Cameroon. In South Sudan, little has been done to relate these structures to the recognised tectono-thermal events in the region. However, based on lithology and orientation Leggo (1974) was able to trace some of these structures from northern Uganda into South Sudan, which suggests they are probably related to the Watian (2.880 Ga) and Aruan (2.550 Ga) events.

The East African Orogen (EAO) is known to be the largest Neoproterozoic–Cambrian orogenic belt on Earth (Patchett and Chase, 2002; Fritz et al., 2013). It came into existence as a result of the collision of amalgamated Neoproterozoic (900 - 550 Ma) arc terranes of the Arabian Nubian Shield (ANS) with the Archean Sahara Metacraton and Congo–Tanzania Cratons to the west (west Gondwana) and the Azania and Afif terranes to the east (East Gondwana) (see Fritz et al., 2013). This Pan-African Belt is

traditionally subdivided into the northern part, known as the Arabian-Nubian Shield (ANS), and the Mozambique Belt (MB), which defines its southern segment (Stern, 1994). The former included juvenile Neoproterozoic crust formed by the amalgamation of several arc/back-arc basin systems, involving abundant ophiolites, arc volcanic and plutonic sequences, and immature sedimentary rocks metamorphosed to greenschist facies (Stoeser and Camp 1985; Vail 1985; Kroner et al. 1987a; Stern, 1994, 2002; Johnson and Woldehaimanot, 2003; Kröner and Stern, 2005; Johnson et al., 2011). The latter (Mozambique Belt) is defined by the reworking of pre-Neoproterozoic crust, which is essentially made up of medium- to high-grade gneisses, migmatites and voluminous granitoids (Kröner and Stern, 2005; Fritz et al., 2005; Collins, 2006; De Waele et al., 2006a; Viola et al., 2008; Bingen et al., 2009).

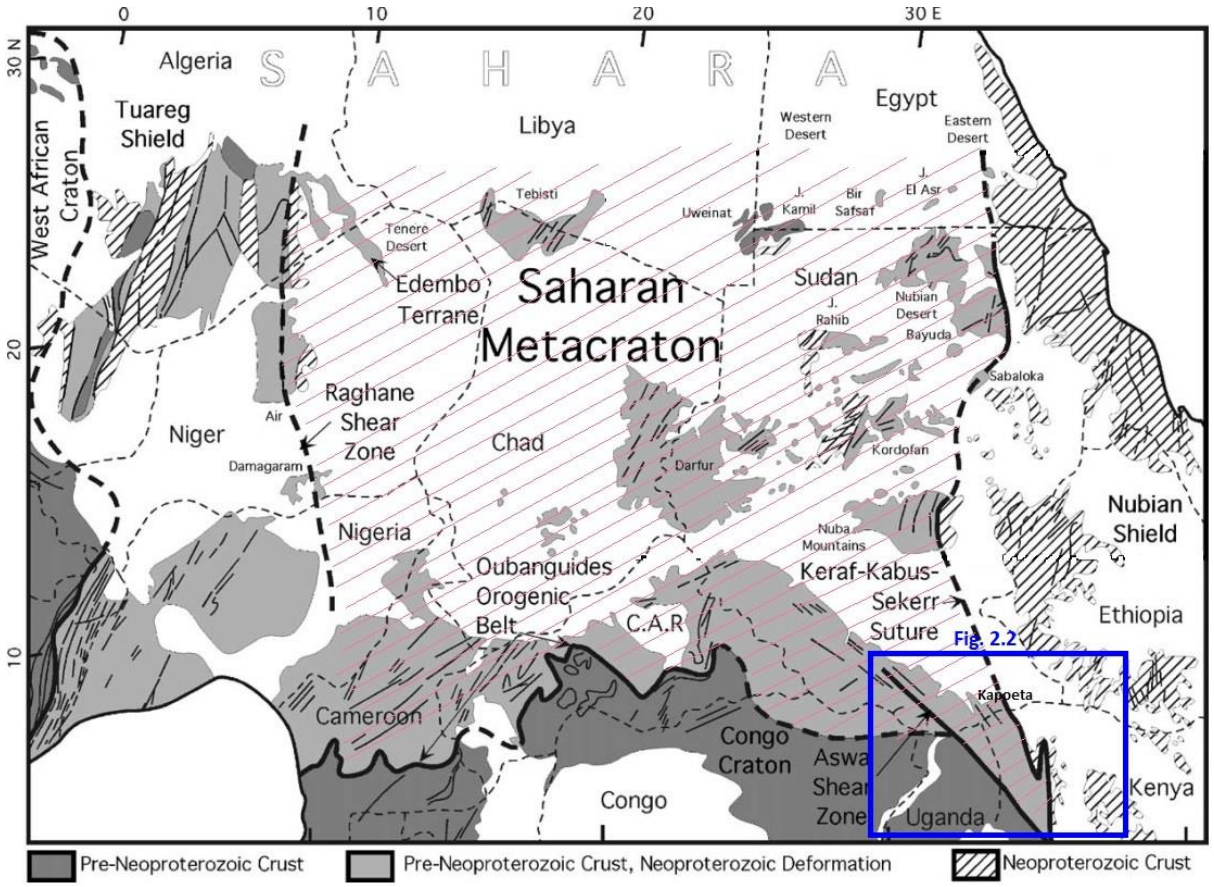

Figure 3.1: Map showing the extent of the Saharan Metacraton, the area shaded; the boundary between Arabian Nubian Shield and Sahara Metacraton is defined by the Keraf–Kabus–Sekerr suture; the Oubanguides orogenic Belt separates the Sahara Metacraton from the Congo Craton to the south. (After Abdelsalam et al., 2002).

3.2 Regional Geology

The geological configuration of the Eastern Equatoria region of South Sudan occupies a vital position in the geological framework of East Africa. It provides the link between the elements of the East African Orogen (EAO, Stern, 1994) and their relationship to the older pre-Neoproterozoic crust defined by Abdelsalam et al. (2002) as the Sahara Metacraton. This portion of South Sudan constitutes part of the north-western Mozambique Belt terrane (Figure 3.2). Various authors have used several

classification schemes to divide the Mozambique Belt into smaller terranes. Mosley (1993) subdivided the Mozambique Belt into three tectonic terranes, each separated by ductile shear zones in which the Karamoja Belt and the Pokot area constitute the western sector to which the study belongs. The Pokot area of western Kenya and Karamoja of eastern Uganda are composed of an amalgamation of reworked Archaean basement and juvenile Pan-African lithologies (Westerhof et al., 2014). Their development occurred over a protracted time interval (0.900 Ga to 0.470 Ga), amid which at least six different tectono-thermal events can be registered (Key et al. 1989).

Westerhof et al. (2014) further divided the Karamoja Belt into (I) the Karasuk-Pokot (east) and (II) the West Karamoja (west). The subdivision of the belt is based on the contrast in geodynamic evolution (e.g., grade of metamorphism) and prominent lithologies. A collage of reworked Archaean basement and juvenile lithologies of Pan-African age underlies the Karasuk-Pokot area of western Kenya and Karamoja of eastern Uganda. The juvenile rocks of the Pan-African event were congregated in the Karasuk Supergroup (Vail 1983, 1988).

The recently completed Mapping Project by the GTK Consortium (2009−2012) concluded that the Karamoja Belt of eastern Uganda is not confined to the narrow border zone underlain by the reworked Archaean basement and rocks of the Karasuk Supergroup (Figure 3.2). West of the current Karasuk thrust front, but still east of the Aswa Shear Zone, several 'Watian' (DGSM 1966) charnockite/ granulite complexes are exposed, which were hitherto regarded to be Archaean in age, related to the 'Basement Complex' of northern Uganda. According to the work of Hunting (1976), the Precambrian basement of the southeastern extreme of South Sudan makes up the northern extension of the Karamoja Belt of eastern Ugandan and western Kenyan.

Many workers have suggested that the boundary between the terrains of the EAO (ANS and MB) is transitional or interfingers (Holmes, 1951; Vail, 1976; Kazmin et al., 1978; Kebede et al., 1999; Fritz et al., 2013). However, the geographical extent varies from one researcher to another. Holmes (1951) concluded that the Ugandan-Kenyan segment (Karamoja Belt) is transitional between the Arabian-Nubian Shield and the Mozambique Belt. Fritz et al. (2013) suggested the ANS merges with the MB in SE Kenya, in a region bounded by continental Africa in the west and Azania in the east. Due to the lack of detailed mapping and chronological studies in the South Sudanese part of the EAO, it is not easy to draw a clear boundary between the ANS and MB. However, based on lithological continuity, it is arguable that this transitional zone is not limited to southern Kenya, as concluded by (Fritz et al., 2013; Holmes 1951). Instead, it can be extended northward into the South Sudan Eastern Equatoria region.

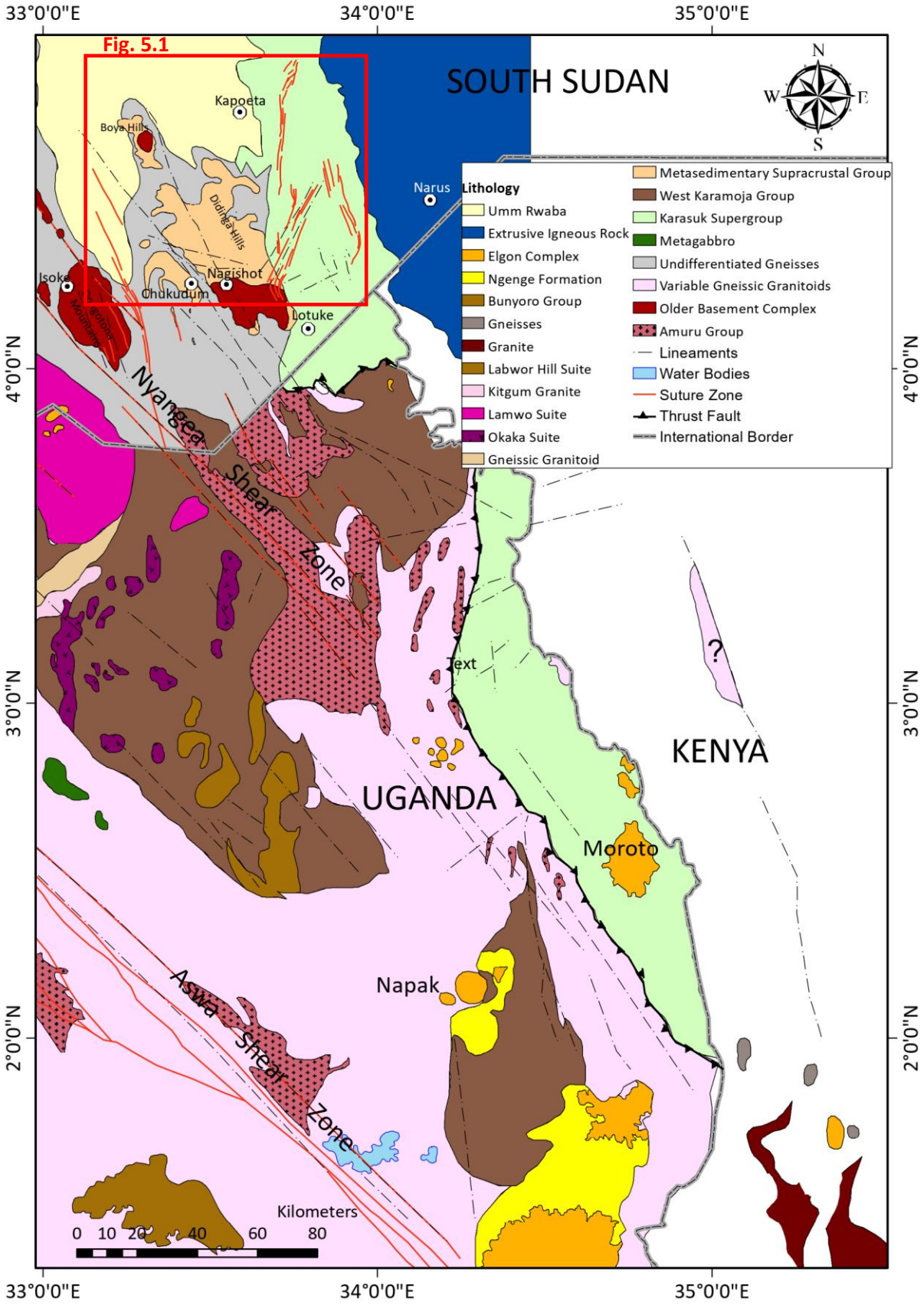

Figure 3.2: Regional map outlining the major lithological units and major structural trends in East Africa (modified after Vail 1988; update based on Belgian Geologic al Survey 1982; Westerhof et al., 2014 maps).

3.3 Geology of the Study Area

The lithostratigraphy of Greater Kapoeta, Didinga Hills, and Dongotona mountains can be divided into four (4) major lithotypes based on relative age and structure. Major lithological units are summarised in Table 3.1; (i) Undifferentiated Basement Complex of Archaean age-related to the reworked pre-Neoproterozoic terrane of the western Mozambique Belt and Sahar a Metacraton, (ii) the Karasuk Supergroup, (iii) Tertiary alkaline intrusive and East Africa Rift related extrusive, (iv) The late Tertiary Umm Rwaba Formation and (v) Superficial Deposits (Figure 3.2).

Table 3.1: Simplified major litho-stratigraphic units of the study area.

No.	Age	Lithology	Formation
1	Recent	Alluvial deposits	Superficial deposits
2	Tertiary to Quaternary	unconsolidated sediments	Umm Rwaba
3	Tertiary	Basalts and the associated volcanics	East Africa Rift Volcanics
4	Basalts and the associated volcanics	East Africa Rift Volcanics	Basalts and the associated volcanics
6	Proterozoic (Neoproterozoic)	Metavolcanic-sedimentary, granites (alaskite) and basic, ultrabasic bodies	Karasuk Supergroup (Westerhof et al., 2014)
5	Archaean	Charnockites, gneisses, migmatites, Metasedimentary supracrustal Group	Basement Complex

3.3.1 Archaean Basement Complex

An unpublished report, of the Belgian Minerals Exploration Mission (1982) divides the Archaean crystalline Basement Complex rocks into (i) the older nucleus (the Dongotona Mountains, part of the southern Didinga Hills, and part of the Boya Hills) and (ii) the younger Basement. Vail (1988) defines the Didinga Hills areas as metasedimentary supracrustal rocks. Fritz et al. (2013) further classified this region as late- to post-orogenic granitoids. These lithologies occupy the region from Boya Hills, and Didinga Hills, stretching westward to the Dongotona mountains. The lithological character constitutes elements of the Sahara Metacraton and western Mozambique Belt and can be correlated to the basement of the Northern Uganda terrane, related to the Aruan tectonism event (MacDonald, 1966). According to Almond (1969); Cahen et al. (1984), the area is dominated by granulites, charnockites, Migmatitic gneisses and hornblende schist, which were strongly reworked during the Pan-African (Figure 3.2), which includes metasedimentary supracrustal rocks of Vail, (1988), surrounding the older nucleus and the undifferentiated basement (Figure 3.2).

Remapping of Uganda's geology and mineral resources was conducted between 2008 to 2012 by the Finnish Geological Survey-based consortium (GTK) (Westerhof et al., 2014) in conjunction with the Geological Survey and Mines Department of Uganda, offers updated data on the diversity in Northern Uganda terrane (Figure 3.2which can be inferred in South Sudan.

3.3.2 Karasuk Supergroup

The Karasuk Supergroup (Westerhof et al., 2014), a name dedicated to the Karasuk Hills of northeastern Uganda, was initially known as the Karasuk Series (Vail, 1983, 1988). The term Karasuk was used in East Africa by Macdonald (1961) and Almond (1969) and has been applied to the Mozambique Belt of Eastern Africa (Holmes, 1951). It constitutes a W- to NW-verging stack of thrust piles, demonstrated, among others, by tectonic repetition of sequences (Westerhof et al., 2014). This Neoproterozoic terrane is regarded as part of the western margin of the Mozambique Belt (Holmes 1951; Almond, 1969), stretching north from NE Uganda and NW Kenya, and occupies a broad area covering the southeastern extremity of South Sudan and extends northwards as far north as Daga Post (HUNTING 1976; Belgium Mineral Exploration Project (BMEP) 1982; Vail 1988b) (Figure 3.2). The Karasuk Supergroup has been thrust over the Karamoja Group. Rocks in both stratigraphic groups strike between N–S and N10^{o}E and display a vertical to sub-vertical dip (Baguma, 2001). This terrane is termed the Cherangani Group in the Pokot region of western Kenya (Petters, 1991). Some authors prefer the collective term Karasuk-Cherangani metasedimentary rocks, but in the context of this study, the term Karasuk Supergroup prevails. Westerhof et al. (2014), divided the rock units of the Pokot and Karasuk into; altered (reworked) Archaean Basement, ophiolites related to Neoproterozoic Mozambique Ocean, metasedimentary rocks from a post-Rodinia passive margin, and syn-collisional meta-sedimentary and magmatic arc rocks. Westerhof et al. (2014) described the Karasuk Group of the Pokot area of western Kenya as constituting a W- to NW-verging stack of thrust piles, exhibited in recurring tectonic sequences. They are discordantly underlain by a series of Archaean or Early Proterozoic age basement rocks well-exposed SE of Mnoropus (see Fig. 2; Belgian Mineral Exploration Project, 1981). An unconformity with grey brownish-white gneiss rests on a complex series of migmatised basic gneisses. The underlying basement can be grouped as the Karamoja Group. In Uganda, they form the Amuru Group and the Morungole massive western Karamoja Group, which can be traced northward into South Sudan (Westerhof et al., 2014).

Generally, the rocks of Karasuk Supergroup are distinguished from the high-grade metamorphosed Archaean crystalline basement of the Northern Uganda Terrane by a thrust plane and 'Schuppen' zones of gneisses with flaggy feature and para-autochthonous and allochthonous tectonic fragments (Westerhof et al., 2014).

The lithologies of the Karasuk Supergroup are genetically an assemblage of both sedimentary and igneous origin, and their source might have come from either East or West Gondwana (Westerhof et al., 2014). Generally, rocks of the Karasuk Supergroup are confined between the Sahara Metacraton forming an interface with the Didinga ranges to the west and the extrusive bodies to the east of the study area; they fall within the greenschist to amphibolite facies regional metamorphism (Table 3.2).

Other lithologies include amphibolites, biotite-hornblende gneisses, marbles, quartzites, chlorite and graphite schists, altered granites, ultrabasic rocks and metagabbro (Almond, 1969).

The metasedimentary rocks within the Karasuk Supergroup comprise predominantly of metamorphosed assemblage of sediments laid down in a passive margin with meta-arenites and meta-carbonates dominating the bottom and near-shore marginal parts of the succession with metapelites in the more distal and deeper parts of the basin (Westerhof et al., 2014).

Table 3.2: Rock types of Karasuk Supergroup from South Sudan and Uganda

Lithology unit	**Percentage in Uganda** (Westerhof et al., 2014; Almond, 1969)	**Rock types**
Hornblendic rock	(45%)	Amphibolites, hornblende-gneisses, and hornblende-schists
Mica gneisses	(43%)	Leucocratic-biotite gneisses, sometimes migmatised; muscovite and graphite-gneisses
Metacalcareous	(10%)	Marbles, calc-silicate gneisses
Quartzites	(< 1%)	Sheared and unsheared
Basic and ultrabasic rocks	(< 1%)	Metagabbros, serpentinites, talc, tremolite and chlorite-schists

Several felsic intrusions were mapped by the Belgian Mineral Exploration Project (1980, 1982, 1983). These include the alaskite, syntectonic granite and pegmatitic bodies. The granite body is massive and occurs in the form of boulders. According to the Belgian Mineral Exploration Project, the syntectonic granite is found west of Lobur. The alaskite occupies the Kawokono anticline's core and is associated with the Kawokono marble exhibiting progressive phases of cataclasis and alteration. The alaskite is characterised by a graphic micro-texture between quartz and micro-perthitic K-feldspar (Belgian Mineral Exploration Mission, 1982). According to the Belgian Mineral Exploration Project (1980), the pegmatitic bodies are found in the Lokadoka riverbed, occurring as small intrusions which appear to be associated with the gneissic complexes. Most of the pegmatitic bodies are concordant with the gneissic foliation.

3.3.3 Alkaline Intrusions of E and NE Africa

Several alkaline intrusions are documented in East and NE Africa, few intrusions, including ring complexes, occur in South Sudan. A group of about fourteen of these alkali rings complexes (Vail, 1985) occupies an N-S band of the country of about 850 km in extent along the Sudan-Ethiopian-South Sudan frontier between the Blue Nile (Abbai) valley and northern Uganda (Vail, 1989). All the known Sudanese alkaline ring complexes are anorogenic, usually subvolcanic, unmetamorphosed igneous intrusions, ranging from a few hundred metres to as much as 20 km in diameter (Vail 1985).

In South Sudan, several intrusions were reported in the southeastern Equatoria region, along the White Nile's upper reaches (Andrew et al. 1955; Vail 1985). Lotuke Mountain is among the twelve

alkaline intrusions found in the extreme southeastern South Sudan, together with two other occurrences around Nagishot and east of Kapoeta (Vail 1978; Hunting Geology and Geophysics, 1980; Andrew et al. 1955, Uganda Geol. Surv. Karamoja map 1967; unpublished map by Belgium Mineral Exploration Project ca 1980). Lotuke occurs along the border of Uganda overlooking Mount Zulia, which is thought to be genetically related. Both are approximately 7 km in diameter and form circular shapes that rise about 2,700 and 2,149 m above sea level.

The mineralogy is characterised by abundant K-feldspar, nepheline of different proportions, brown biotite, blue-green amphibole (probably arfvedsonite), and aegirine augite. The minor minerals are euhedral sphene, apatite, zircon, and leucite (Belgian Mineral Exploration, 1983). The two alkaline complexes, Mount Lotuke and Zulia, comprise granite-syenite complexes, of which Zulia, just across the Uganda border, contains syenites and foid syenites (Uganda Geol. Surv. Karamoja map 1967). Mount Lotuke syenite is not adequately studied but is part of the Cenozoic (Neogene) magmatism related to the Elgon Alkaline Province (Westerhof et al., 2014).

3.3.4 Tertiary Extrusive Rocks

These lavas are believed to be genetically linked to the East African Rift System described in northern Kenya and Ethiopia. These volcanics are widely distributed in East Africa, covering most of Ethiopia and Eritrea and extending to the Gadaref region of Sudan. According to Walsh and Dodson (1969), they are mainly augite and analcime basalts, olivine basalts, phonolites, nephelinites, rhyolites and andesites. The lavas stretch north to the Pibor area and eastward into north-western Kenya, overlying part of the Karasuk Supergroup rocks, though there is no evidence of samples from drilling to verify that. The thickness of the flows in South Sudan is unknown, whereas, in Ethiopia, these lavas are more than 3000 m thick in places. They were extruded simultaneously with the formation of the Rift Valley, whereas in Sudan, they are much thinner. Whiteman (1971) suggested that the lava flow is thinning from the centre, which could be the case in South Sudan. He also argued that although marked on the map as Tertiary volcanics, not all these rocks are of this age. For example, dating of potassic basalts from the Fareig volcanics intruded into Nubian Sandstone at the slight bend of the Nile at Fareig, north of Dongola, yielded an age of 88 ±8 million years, which is Upper Cretaceous rather than Tertiary (Whiteman, 1971), which suggests multi-episodic events. New geological and geochronological information identified four major episodes of regionally significant volcanism and rift formation. These episodes began at approximately 10 Ma (Chernet et al., 1998).

3.3.5 Umm Ruwaba Formation

The Tertiary to Quaternary Umm Ruwaba Formation cover most part of South Sudan extending from the north southward to Juba and southeast up to Kapoeta. The Umm Ruwaba is made up of

unconsolidated sands, locally gravelly, clayey sands, and clays containing characteristic carbonate nodules or calcretes. The sediments are poorly sorted, and the thickness vary from place to place (Yassin et al. 1984, NCDRWRS-TNO-DGV 1989, Senden 1989, GRAS 1995, Salama 1997, GRAS 2004, SMEC 2013, Gauff Ingenieure 2018), and were presumably underlying the Sudd Region and were probably laid down as proto-Nile deposits accumulated in this great subsiding area, which was even then, perhaps, occupied by lakes and marshes (Whiteman, 1966). Like elsewhere in South Sudan and Sudan, where the Umm Ruwaba Formation exists, no outcrops are known, and the lithologies are known only from borehole logs. Tectonically, the Umm Ruwaba Formation appears to be undisturbed since deposition. Hence, the sediments are characterised by a horizontal-lying sequence of unsorted or unconsolidated sediments as mentioned above. The sediments are believed to be of fluviatile and lacustrine origin and were deposited in a series of interlocking land deltas and fans (Whiteman 1966).

3.3.6 Superficial Deposits

In the Kapoeta area, the surficial deposits include alluvial deposits along the banks of major stream channels and in stream beds. The alluvial deposits are restricted to water channels such as those along the bank of the river Nile. The aeolian deposits represent a thin blanket laid unconformably on the basement terrane. The thickness varies from place to place depending on the terrain.

Chapter 4 Methodology

4.1 Introduction

This study adopted an integrated approach involving several methods and data sets. The methods used include remote sensing field validation and laboratory work mainly for geochemical analysis.

4.2 Remote Sensing and Interpretation

The satellite images used in this study include Landsat 8 OLI/TIRS, Landsat 7 ETM and Shuttle Radar Topographic Mission (SRTM) Digital Elevation Model (DEM) images. The two Landsat (8 OLI and 7 TM) images were acquired from US geological survey (USGS) website under ID Nos LC08_L1TP_171057_20170115_20170311_01_T1, LE07_L1TP_171057_20000125_20170213_01_T1. The abbreviation (OLI) stands for Operational Land Imager, which can provide an image at 30-metre resolution multispectral and 15 metres panchromatic bands. It comprises the first eight (8) bands of Landsat 8. The (TIRS) refers to a Thermal Infrared Sensor, which provides images at 100 metres resolution (Table 4.1).

Table 4.1: Landsat 8 OLI and Landsat 7 ETM spectral band characteristics used in the study (USGS)

Landsat 8 OLI			Landsat 7 TM		
Bands	**Wavelength (μm)**	**Resolution**	**Bands**	**Wavelength (μm)**	**Resolution**
B1	0.43-0.45	30			
B2 Blue	0.45 – 0.51	30	B1	0.441 – 0.514	30
B3 Green	0.53 – 0.59	30	B2	0.519 – 0.601	30
B4 Red	0.64 – 0.67	30	B3	0.631 – 0.692	30
B5 NIR	0.85 – 0.88	30	B4	0.772 – 0.898	30
B6 SWIR 1	1.57 – 1.65	30	B5	1.547 – 1.749	30
B7 SWIR 2	2.11 – 2.29	30	B6	2.064 – 2.345	30
B8 Panchromatic	0.50 – 0.68	15	B7	2.08 - 2.35	30
B9 CIRRUS	1.36 - 1.38	30	B8	0.52 - 0.90	15
B10 Thermal Infrared (TIRS) 1	10.60 - 11.19	100			
B11 Thermal Infrared (TIRS) 2	11.50 - 12.51	100			

Both OLI and TIRS are instruments onboard the Landsat 8 satellite. The Enhanced Thematic Mapper Plus (ETM) is an improved version of the Thematic Mapper instruments sensors onboard Landsat 4 and Landsat 5 (https://www.usgs.gov/landsat-missions/landsat-7).

The Landsat 8 and the Landsat 7 ETM image captured on 15 January 2017 and 15 January 2000 are of path 171, raw 57, with 0% cloud cover acquired from the United States Geological Survey

(www.earthexplorer.usgs.gov). Moreover, the SRTM Digital Elevation Model (DEM) with a resolution of 30m was obtained from the same website.

Figure 4.1 shows the flow-chart adopted in the processing of remotely sensed datasets. The image processing strategy followed involves the use of colour composite images, band ratioing, principal component analysis (PCA), minimum noise fraction (MNF), unsupervised classification, supervised classification and hillshade. The image processing software used includes the Environment for Visualizing Images version (ENVI) version 5.3, ArcMap 10.6 and QGIS version 3.20.1-Odense, at different levels and purposes.

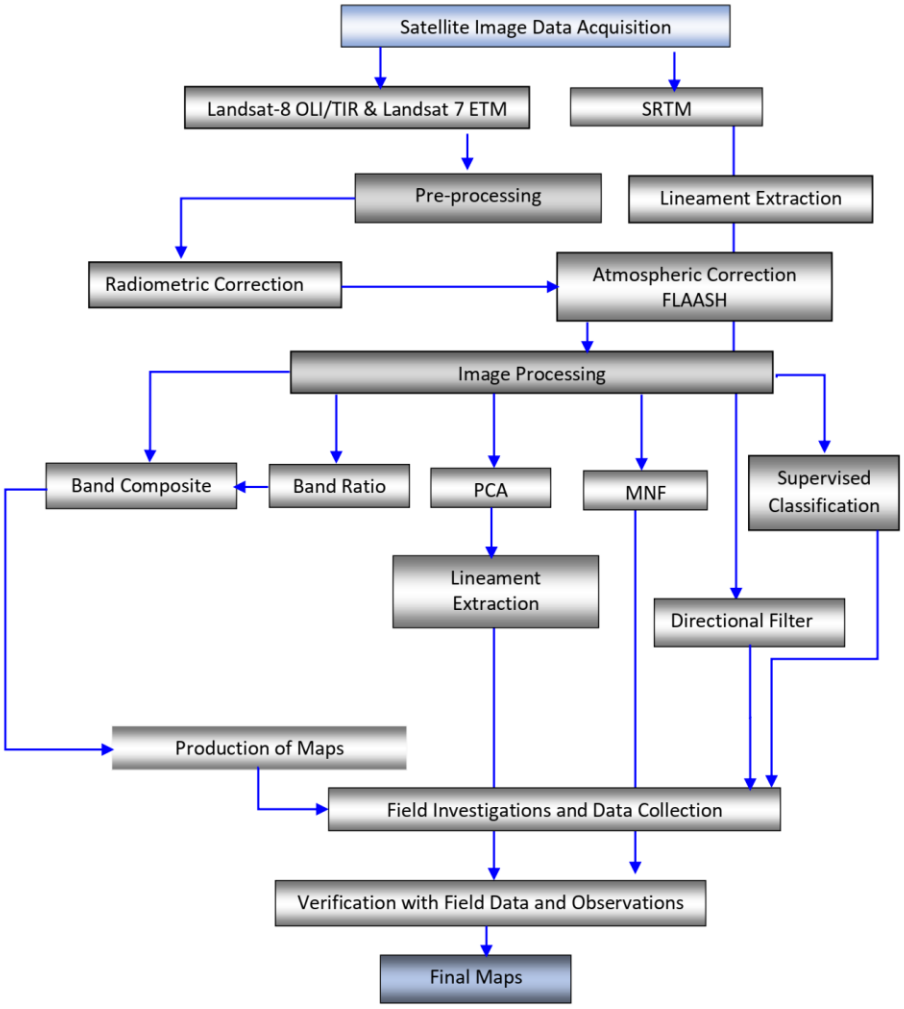

Figure 4.1: Flow Chart illustrating the satellite image processing procedure.

4.3 Pre-processing of satellite images

Table 4.1 shows the list of bands used to create a subset of the study area. Atmospheric correction is filtering the effects of the atmosphere on the reflectance values of images acquired by satellite or airborne sensors (Pacifici et al., 2014; University of Maryland Institute for Advanced Computer Studies, 2008). It involves omitting the effect of scattering and absorption of the atmospheric molecule and

aerosol on object reflectance (Jinguo and Zheng, 2008). Atmospheric effects in optical remote sensing are significant and complex, dramatically altering the spectral nature of the radiation reaching the remote sensor (Schowengerdt, 2007).

The Landsat-8 OLI image bands were converted to calibrated radiance and then converted to surface reflectance in Fast Line-in-sight Atmospheric Analysis Spectral Hypercube (FLAASH) to remove the influence of the atmosphere. Initially, the input image for FLAASH must be a radiance image in band-interleaved-by-line (BIL) or band-interleaved-by-pixel (BIP) format. FLAASH is a first-principles atmospheric correction tool that corrects wavelengths in the visible through near-infrared and shortwave infrared regions, up to 3 µm. These corrections were processed at-sensor radiance, at-sensor reflectance, and at-surface reflectance. Radiometric correction is one of the essential steps in mineral exploration and lithological discrimination using remote sensing techniques (Rajendran and Nasir, 2014). Radiometric calibration calibrates image data to radiance, reflectance, or brightness temperatures and reduces errors in images' digital numbers (Traore et al., 2020).

4.4 Image Processing

The filtered satellite images were subjected to the following processing techniques, and the results are discussed in the following subsections.

4.4.1 Colour Composite Images

A colour composite is a technique of displaying remote sensing images of different bands in three primary colours (red, green, and blue) to produce a Colour Composite Image. A composite of natural colours made of red, green, and blue (in RGB mode) images can distinguish features related to geology, including textural characteristics of igneous and sedimentary rocks, structural features, and vegetation at a regional scale (Sabins, 1999). Band 432 was used to generate a true colour composite; FCC was produced using band 257 in RGB.

4.4.2 Band Ratio

The spectral band ratio is one of the most powerful techniques for mapping the minerals of clay, alunite, and iron minerals (Sabins, 1999). This remote sensing technique is applied mainly in geological studies (Amer et al., 2010; Ali and Pour 2014; Si Mhamdi et al., 2017; Yousif et al., 2018). Band ratios are simple arithmetic combinations of different bands that enable the distribution and intensity of specific absorption or emission features to be investigated semi-quantitatively (Sabins, 1997). The technique is performed by first dividing the digital number value of one band by the digital number value of another band (Mars and Rowan, 2006; Pour and Hashim, 2012). The ratio of the bands is selected based on the reflectance and absorption features of a given target (Amer et al., 2010). The band ratio composite is then performed by combining three-band ratio images in RGB (Red, Green,

Blue) after producing the individual band ratio of all seven bands in the Envi 5.3 version of the software. Several band ratio composites were tested by combining the following ratio in RGB.

A

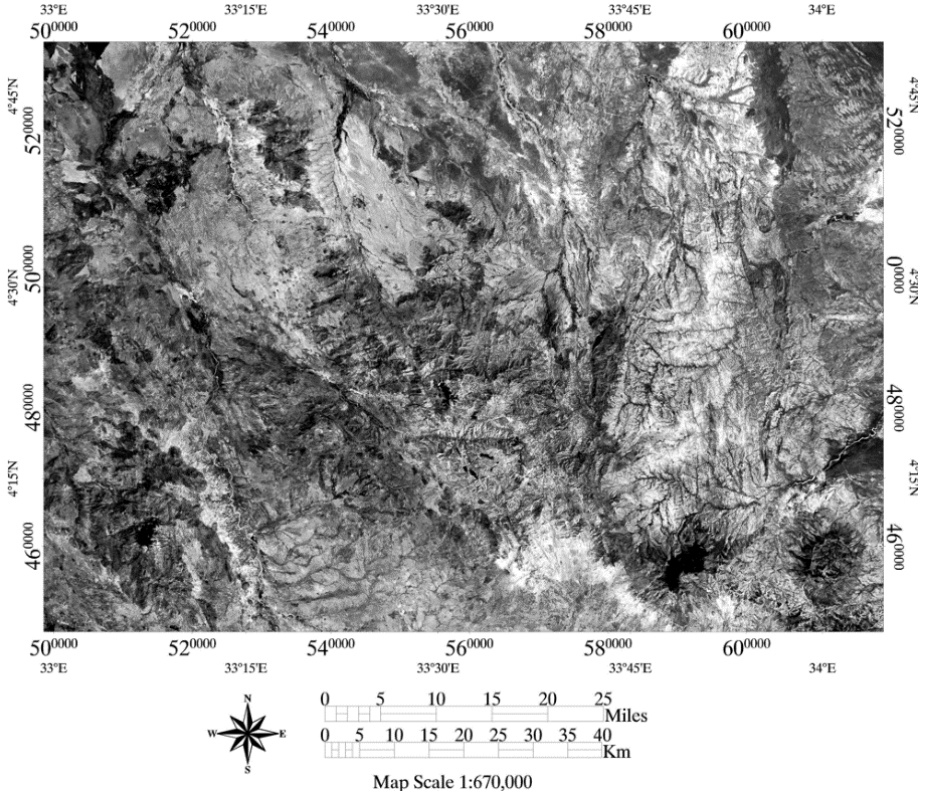

Map Scale 1:670,000

B

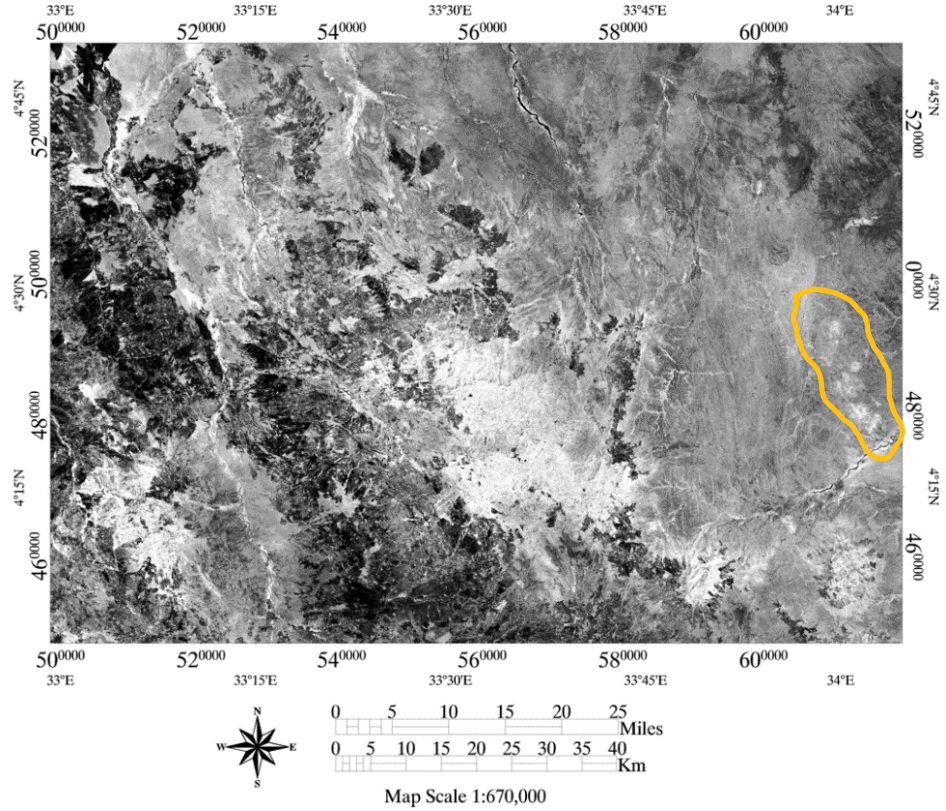

Map Scale 1:670,000

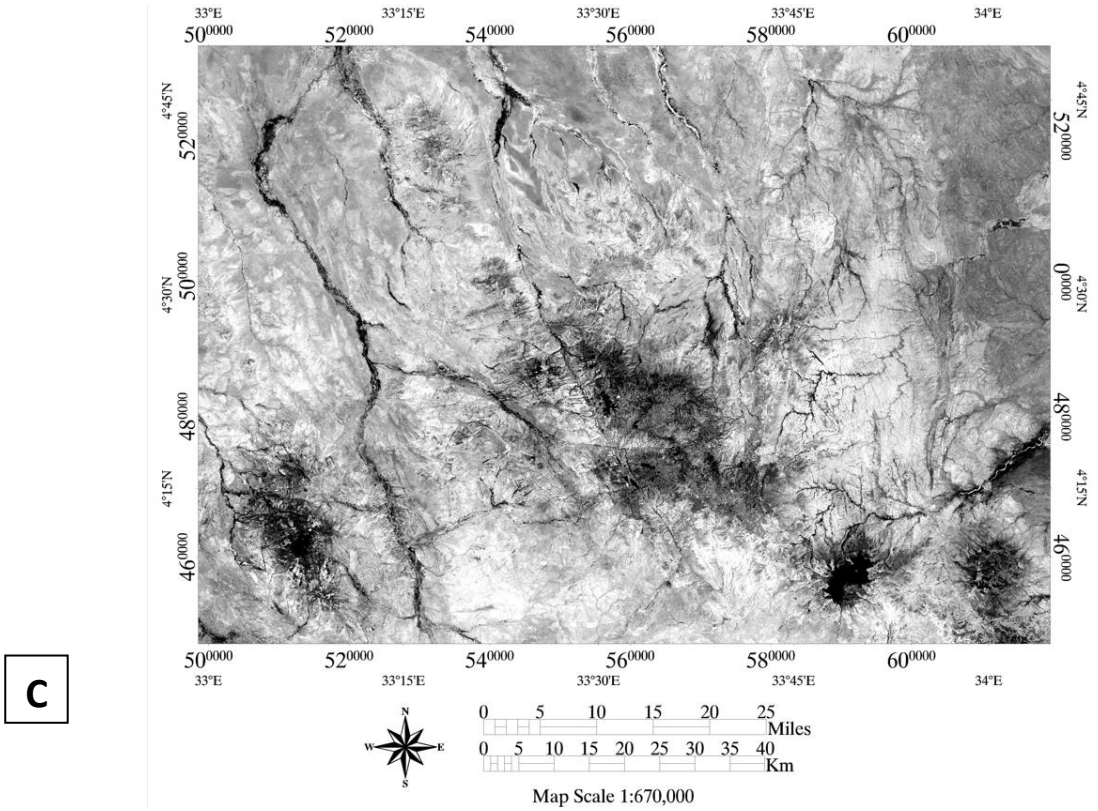

Figure 4.2: Landsat 7 ETM band ratio result (A) Band ratio 4/2, (B) band ratio 6/7, (C) band ratio 6/5.

The ratio 4/2 was used for mapping iron oxides because it has an absorption in the blue region, with high reflectance in the red region. The band ratio of 6/5 was useful to map ferrous minerals due to the high reflectance of these minerals in this ratio (Gupta, 2003). The band ratio 6/7 is always employed to effectively outline kaolinite, montmorillonite, and clay minerals and areas covered by vegetation. These minerals have high reflectance in the band (6) and low reflectance in band 7 of the Landsat 8 image. See the yellow mark in : B. The rest of the bright reflections in the image could be but are not limited to vegetation.

4.4.3 Principal Component Analysis (PCA)

Principal components analysis (PCA) reduces the number of variables and attenuates information redundancy (Wold et al., 1987; Pour et al., 2016; Mathew and Ariffin, 2018b). The bands of PCA data are non-correlated and independent and are often more interpretable than the source data (Jensen 1986). This technique can efficiently discriminate lithological units and geological structures (Amer et al., 2010; Pour et al., 2016; Gasmi et al., 2016). Previous studies have suggested that the first three bands of PCA contain over 90% of the spectral information (Amer et al., 2010, 2012; Richards, 2013; Adiri et al., 2016). Figure 4.3 shows a colour composite of principle component analysis of Landsat 7

ETM PCA2, PCA5, and PCA4 in RGB mode. The combination successfully categorised and distinguished the main lithological units in the area.

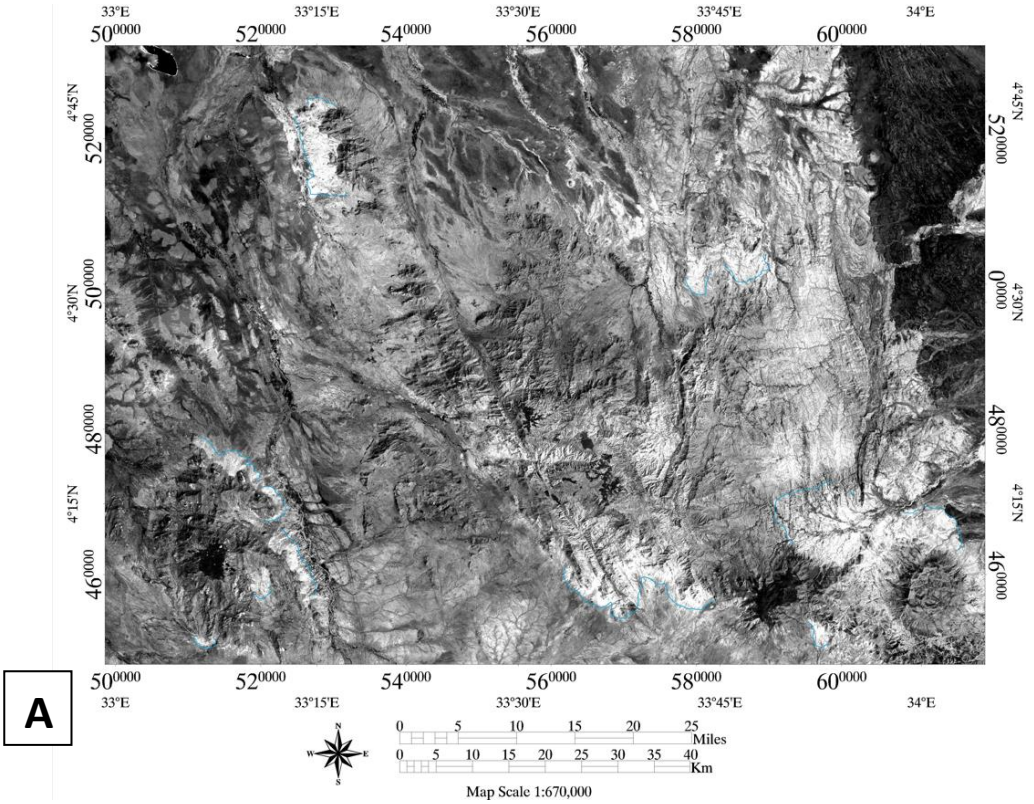

A

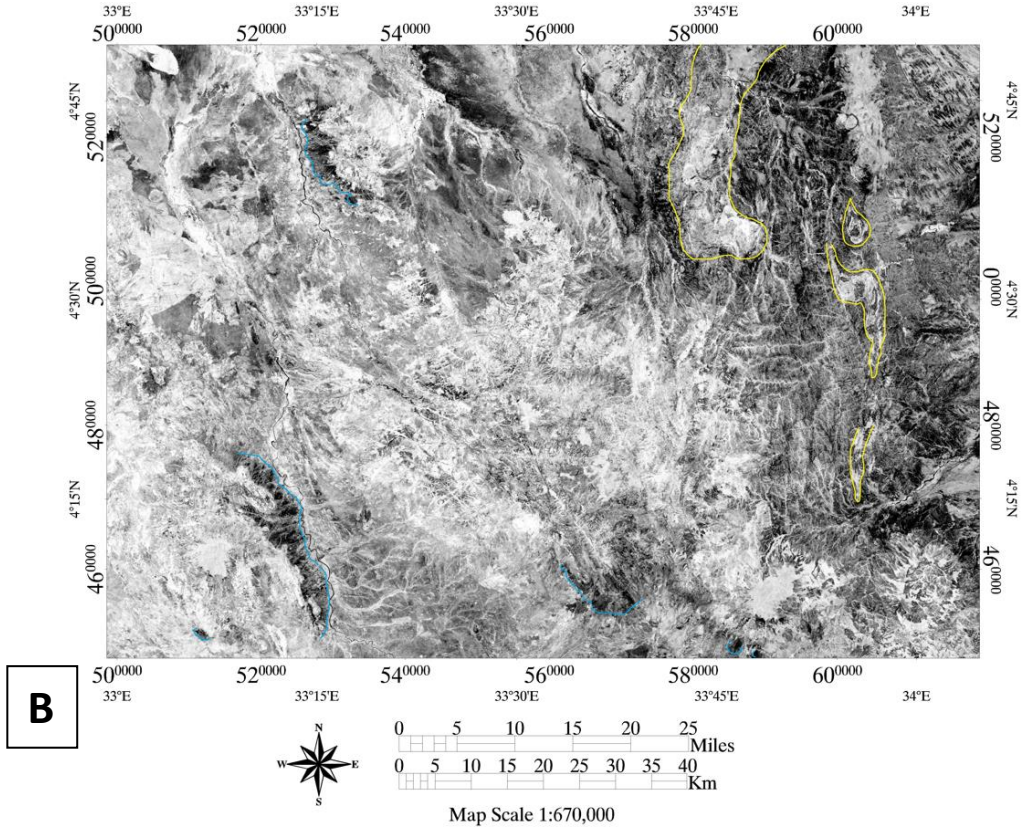

B

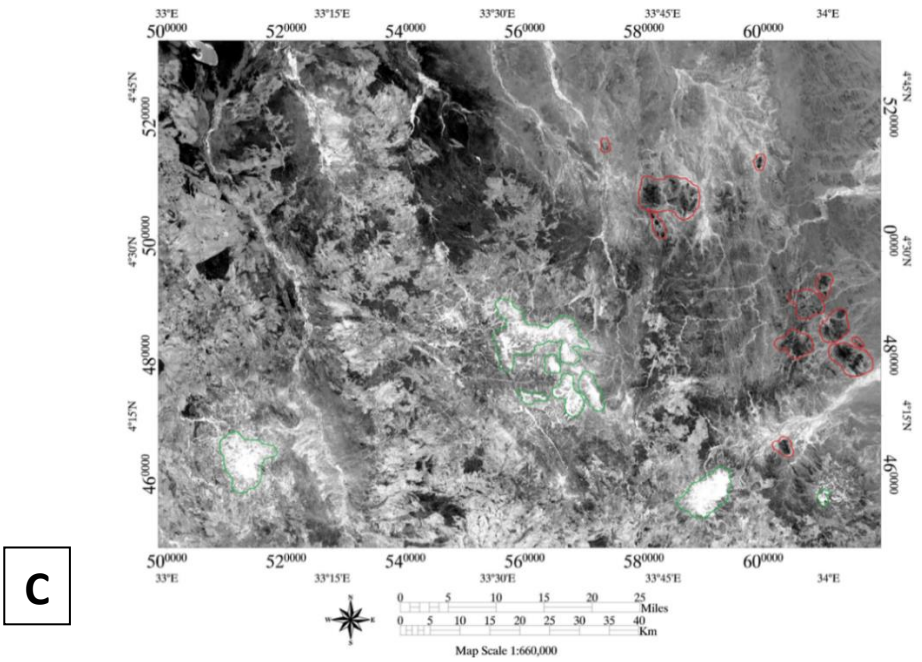

*Figure 4.3: PCA pan-sharpened single bands **(A)** PCA-2 bright reflections are alluvial fans around the mountains, and unconsolidated sediment, dark colour reflection to the north-east are the extrusive igneous bodies **(B)** PCA-4, yellow demarcation is ultrabasic-basic rocks and marbles, blue is an alluvial fan, and unconsolidated sediments **(C)** PCA-5 highlighted in red are ultramafic, gabbro and rhyolite, green highlights are vegetation.*

4.4.4 Minimum Noise Fraction (MNF)

The minimum noise fraction (MNF) transformation technique is used to determine the underlying dimensionality of image data, segregate noise in the data, and reduce the computational requirements for subsequent processing (Green et al., 1988; Boardman and Kruse, 1994; Chen, 2000; Bertels et al., 2005). This technique was employed in conjunction with PCA to validate and enhance the extraction of lithological categorization.

4.4.5 Supervised Classification

Supervised classification is always used for quantitatively analysing remote sensing image data (Richards, 2022). The technique is based on the notion that a user can select sample pixels in an image representative of specific classes and then direct the image processing software to use these training sites as references for the classification of all other pixels in the image. Training sites are sampled based on the prior knowledge of the user. The user also sets the bounds for how similar other pixels must be used to group them. These bounds are often set based on the spectral characteristics of the training area, plus or minus a certain increment. The user also determines the number of classes into which the image is classified.

4.4.6 SRTM-DEM

Hill shading was generated from the Shuttle Radar Topographic Mapping (SRTM), a directional filter technique involving the Kernel convolution method in ENVI version 5.3. This technique was

instrumental in understanding the structural trends of major lineaments and geomorphology. A four-directional illumination of 45°, 90°, 315° and 360°, with a sun angle hanging at 35°, was applied to correspond to NE-SW, E-W, NW-SE, and N-S directions. Based on these multi-direction illuminations, three major structural trends were realised.

4.4.7 Lineament Extraction

Lineament analysis is an essential step in geological and geophysical studies, providing valuable information about the structural features of an area. In lineament analysis, various image processing and interpretation techniques are employed. However, field validation becomes crucial to ensure the accuracy and reliability of the obtained results.

A lineament is a linear feature on the Earth's surface representing an expression of an underlying geological structure such as a fault, dyke, fissure, etc. For mapping the lineaments in the area, two methods were applied to two different images: SRTM and Landsat 8 images. Visual extraction of the lineaments from both images was carried out manually. The SRTM image was first processed by producing a hillshade from four different directions (360°, 45°, 90°, 270°) with the sun angle at 45°.

The Landsat 8 image was subjected to the PCA technique to acquire an image with maximum data. Subsequently, the selected PCA band was subjected to enhancement to produce a better resolution. Figure 4.4 illustrates the workflow for the lineament extraction and the software involved in the process for each stage. As described above, visual observation was employed on both SRTM, and Landsat 8 enhanced image Rose diagram of lineaments mapped four orientations, N-S, NNW-SSE, NW-SW, and NE-SW (Figure 4.5).

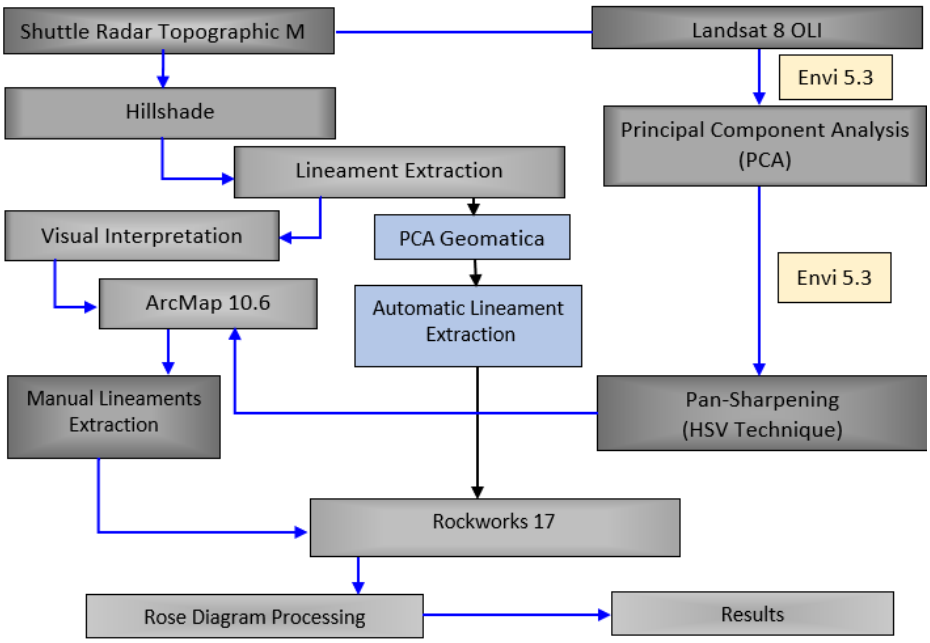

Figure 4.4: Flow chart showing the workflow for lineament extraction.

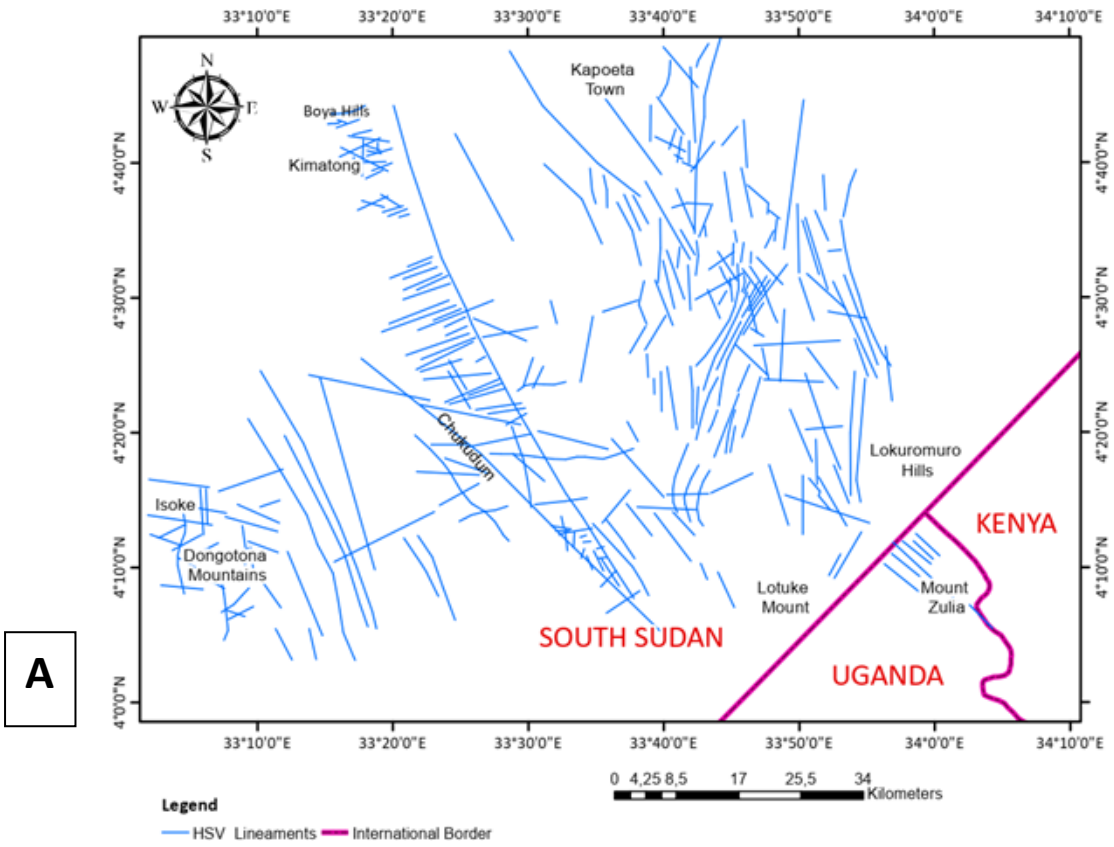

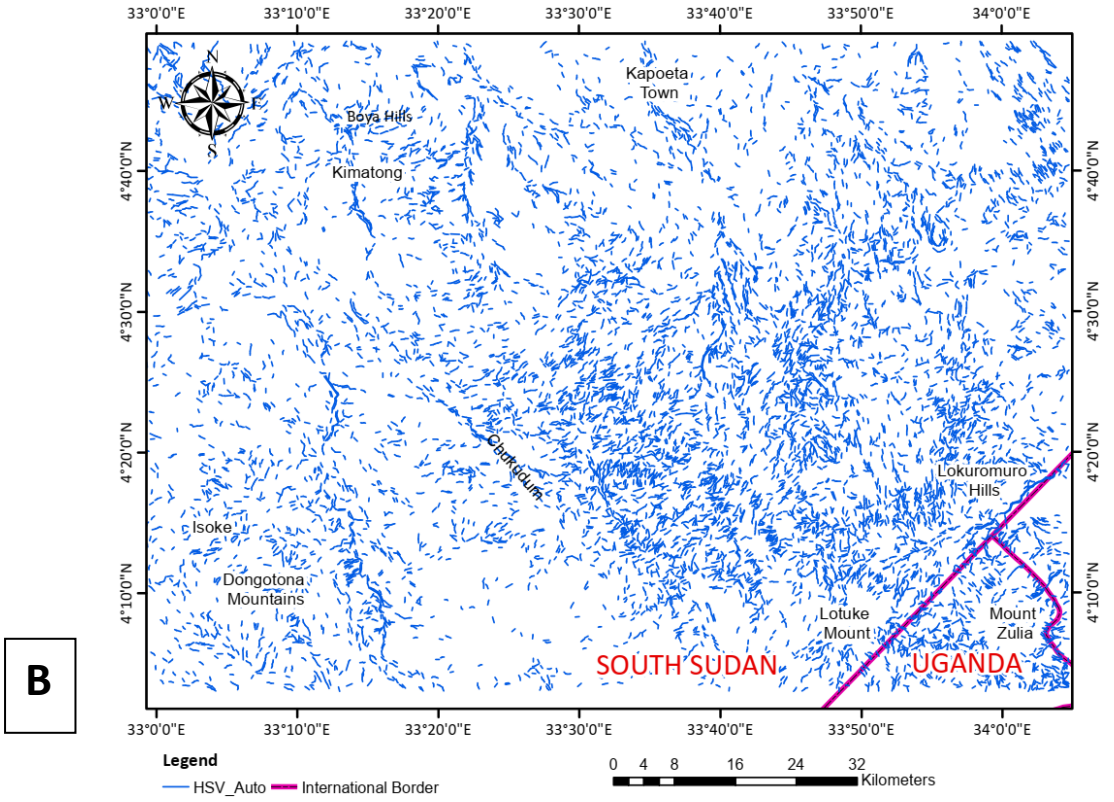

Figure 4.5: Landsat 8 OLI pan sharpened PCA 1 showing ***(A)*** *visual interpretation lineaments extraction and* ***(B)*** *Automatic lineaments extraction.*

4.5 Field Work and Sampling

Prior to the fieldwork, office work was first conducted to review available geological maps. This was followed by the processing of satellite imageries-based maps for fieldwork. Landsat 8 OLI images of various band combinations were used to produce the base maps with the scale of 1:500,000 and 1:200,000 for regional reconnaissance and detail mapping. The field data were collected in February 2021. The approach undertaken in collecting samples during fieldwork is composed of geo-traverses, preferably across strike from E-W and vice versa. More than thirty rock samples were collected from several outcrops for petrographic and geochemical analysis. Out of the total rock samples collected, only fourteen were considered for geochemical analysis, mainly composed of metavolcano-sedimentary lithologies. The samples vary in weight with the larger ones about 5 kg. Systematic measurements of the structural elements, such as planar and linear fabrics, were collected to build field relationships between different lithological units in the area and their regional implication. Artisanal mining activity sites were documented as additional data without collecting gold grain samples and residual panning deposits.

4.6 Geochemistry

The chemical analysis of fourteen (14) samples of metavolcano-sedimentary lithologies collected from the rock exposures, preferably along shear affected zone, was determined. X-Ray Fluorescence (XRF) technique was applied to determine the major elements oxides. Trace elements concentration was analysed using Inductively Coupled Plasma-Mass Spectrometry (ICP-MS) at the Geosciences Earth Lab of the School of Geosciences house in the school of Geography, Archaeology, and Environmental studies, University of the Witwatersrand, Johannesburg, South Africa. A LOI (loss on ignition) technique was applied to eliminate the effect of volatiles. The results of the analysis are presented in chapter six below.

4.7 Reinterpretation of Data

The tools used in data processing before the interpretation varies with data types in question. Observations of outcrops and correlation of various lithological units and structural features were documented during the fieldwork. The remote sensing images were processed using ArcGIS, ENVI 5.3 and RockWorks 17 software. The interpretation is based on the spectral responses corresponding to specific features or minerals on the ground. Visual interpretation based on tonal variation, patterns, shapes, and textures is common. The geochemical data was interpreted using Geochemical Data Toolkit (GCDkit). The method provided a flexible and comprehensive platform for efficient data processing, visualisation, and statistical analysis (Ihaka & Gentleman, 1996; Grunsky, 2002; R Development Core Team, 2005).

Chapter 5 Results

5.1 Remote Sensing and Interpretation

In this study, remotely sensed datasets were employed in two phases during the investigation: (I) pre-fieldwork image processing and interpretation of the geology and structure features in the study area, including plotting of previous sites of artisanal mining activities, which permits prediction for possible mineralisation. This exercise allowed the identification of geological features related to the potential targets and the creation of a base map taken to the field for validation, and (II) the assertion and generation of various lithological and structural datasets in the area using field data capture techniques and field traverses.

5.1.1 Colour Composite Images

Using the colour composite images technique, four images were produced by configuring different bands in RGB and the following band combination were found effective in the identification of geological features in the area: 4-3-2, 2-5-7, 7-4-1 and xxx (Figure 5.1).

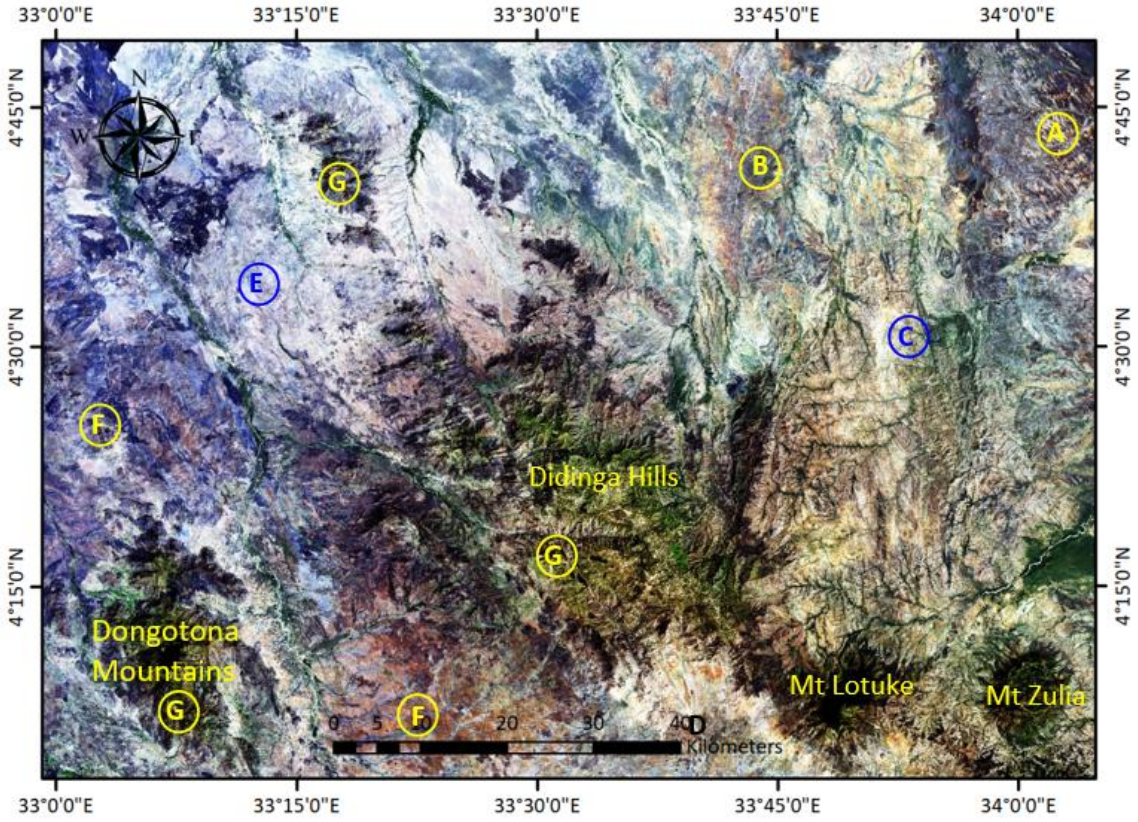

Figure 5.1: Landsat 8 OLI image Band combination 432 in RGB natural colour composite; Green indicates vegetation cover; ***(A)*** *brown to dark brown to the northeastern corner of the map indicates the extrusive rocks;* ***(B)*** *the ultramafics and metavolcanic bodies have the same tone;* ***(C)*** *the bright yellow colour represents undifferentiated gneisses and schists covered by sediments;* ***(D)*** *alluvial fans shown as bright at the foot of the outcrops;* ***(E)*** *Umm Rwaba Formation is shown in light or bright colours to the NW of Didinga Hills;* ***(F)*** *Undifferentiated basement complex:* ***(G)*** *Older Basement.*

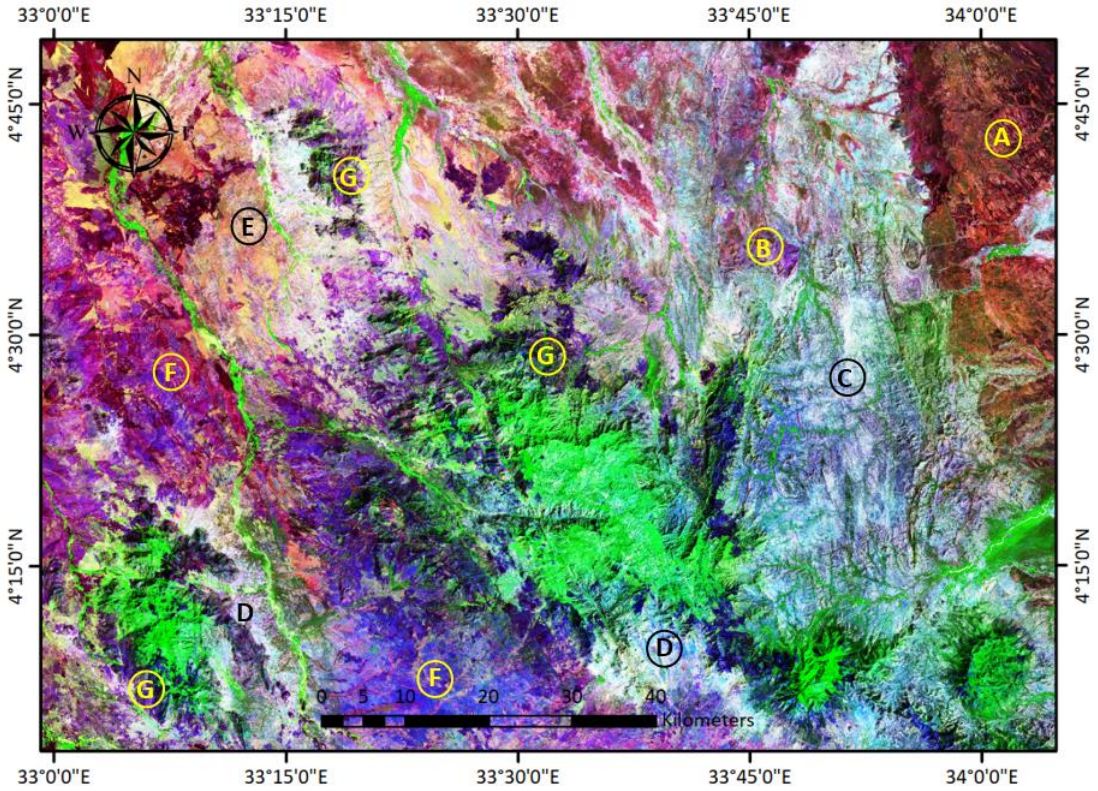

*Figure 5.2: Landsat 8 OLI image Band combination 257 FCC in RGB; **(A)** brownish colour highlights extrusive bodies; **(B)** basic-ultrabasic bodies; **(C)** undifferentiated gneisses and schists; **(D)** White = alluvial sediments; **(E)** Yellowish to orange = Umm Rwaba Formation; **(F)** Blue and purple indicates undifferentiated Basement Complex rocks; **(G)** Older basement; **(H)** Green represents vegetation cover.*

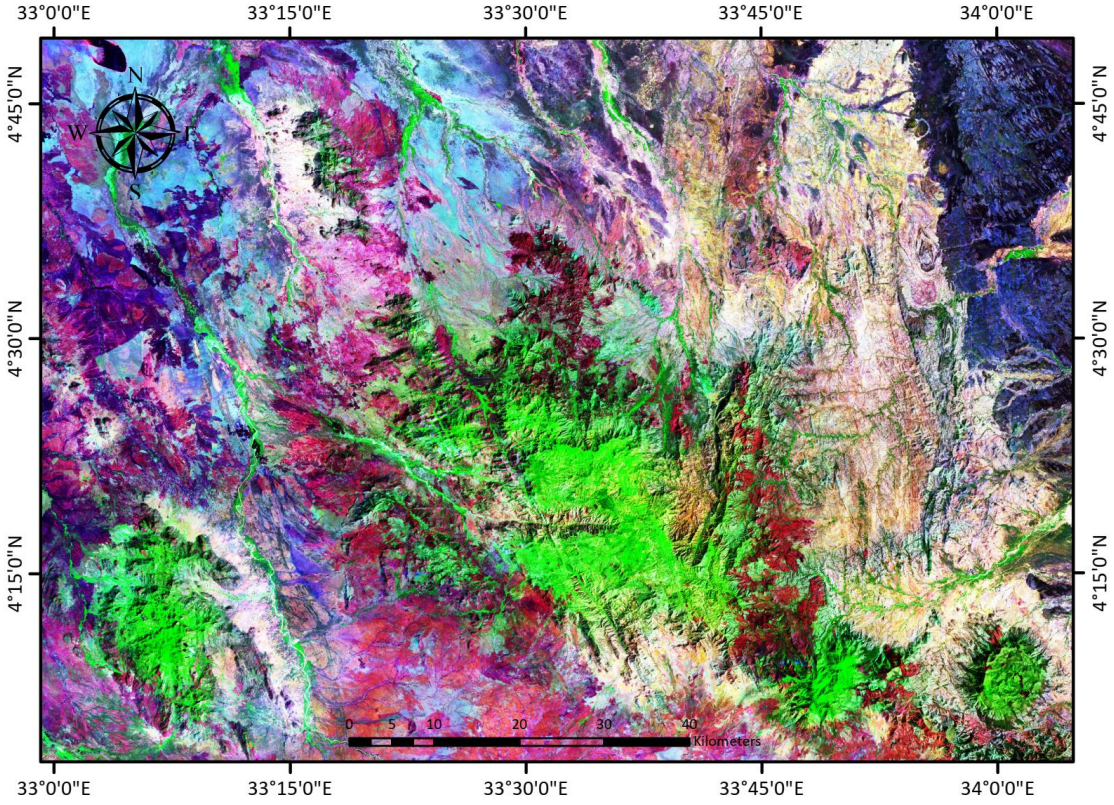

Figure 5.3: Landsat 7 ETM image band combination 741 in RGB

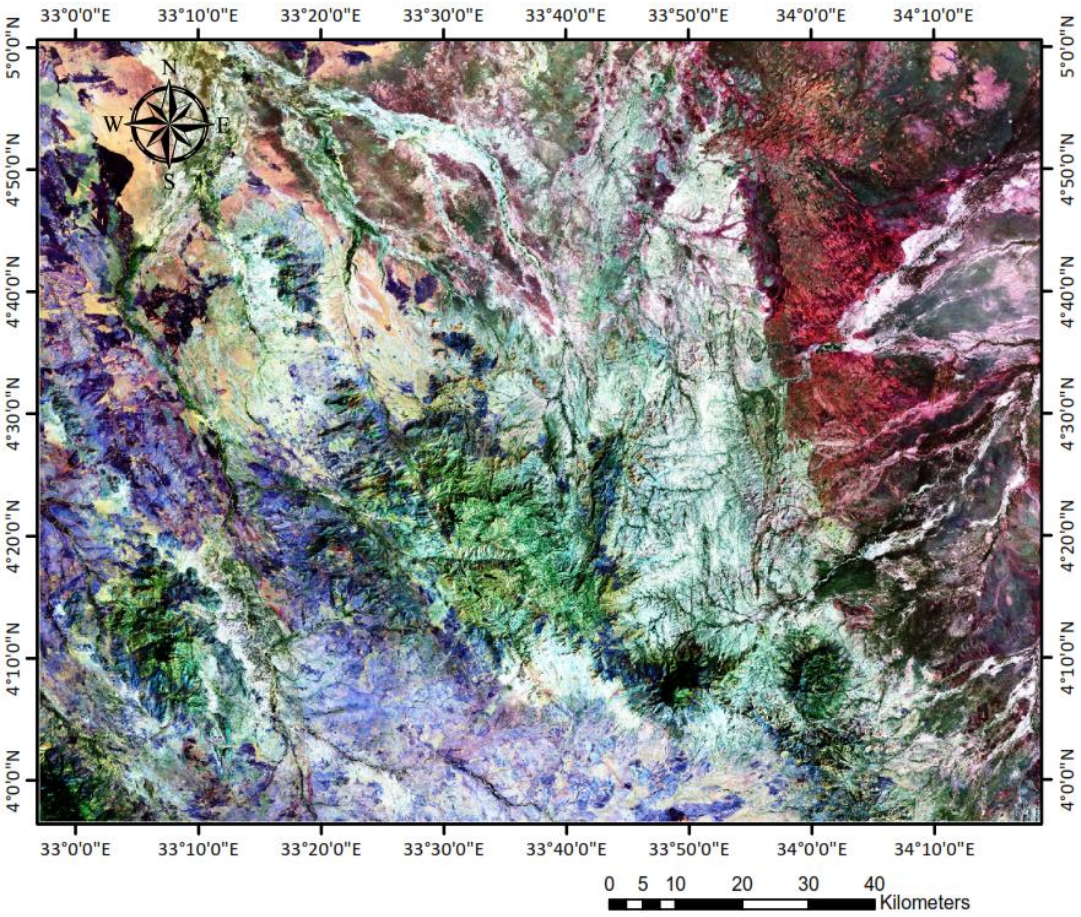

Figure 5.4: Landsat 7 ETM image band combination 257 in RGB

5.1.2 Band Ratio

The band rationing technique was used to enhance the Landsat image for better identification of geological, structural features and zone with high concentrations of certain minerals alterations in the study area. Several band ratio images were produced, including band ratio 4/2, which is used to map iron oxides because it has an absorption in the blue region, with high reflectance in the red region. The band ratio 6/7 is employed to effectively outline kaolinite, montmorillonite, clay minerals and areas covered by vegetation (Figure 4.). These minerals have high reflectance in band (6) and low reflectance in band 7 of the Landsat 8 image. Band ratio composite is then performed by combining three-band ratio images to enhance lithological identification in RGB (Red, Green, Blue). Several band ratio composites were tested by combining several band ratios in RGB, and band 7/5: 6/4: 4/2 band ratio composite in RGB appears to be the best combination (Figure 5.5).

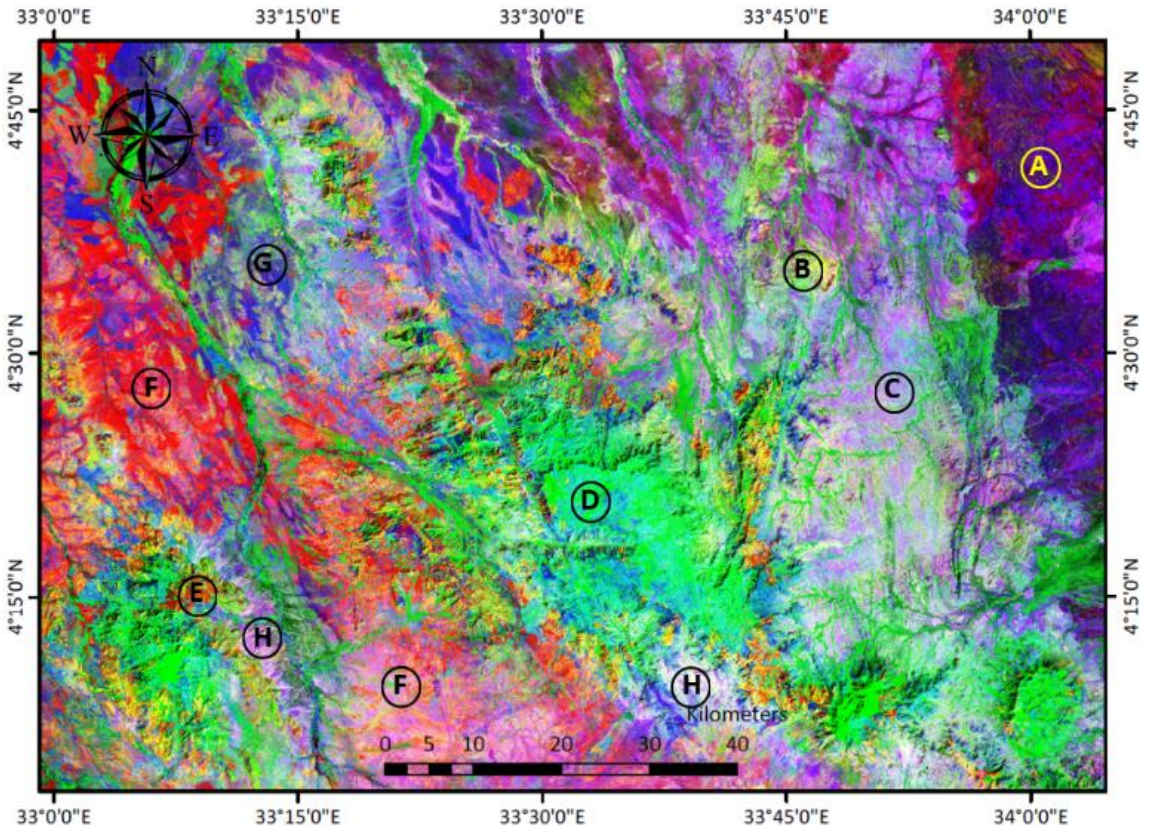

Figure 5.5: Landsat 8 image 7/5: 6/4: 4/2 band ratio composite in RGB; ***(A)*** *Dark blue with the hue of red defines the extrusive bodies;* ***(C)*** *Basic body* ***(D)*** *Green vegetation; light purple Karasuk Supergroup assemblages;* ***(E)*** *orange corresponds to Old Basement Complex* ***(F)*** *pinkish to orange corresponds to undifferentiated gneisses* ***(G)*** *Umm Rwaba Formation* ***(H)*** *alluvial sediments.*

5.1.3 Principal Component Analysis (PCA)

The result of the pan sharpened PCA for the three selected images is presented above in Figure 5.6 with each band showing unique characteristics from the other bands. Figure 5.6 shows a colour composite of the principal component analysis of Landsat 7 ETM PCA2, PCA5, and PCA4 in RGB mode. The minimum noise fraction (MNF) transformation technique was employed in conjunction with PCA to validate and enhance the extraction of lithological categorization, as shown in Figure 5.7.

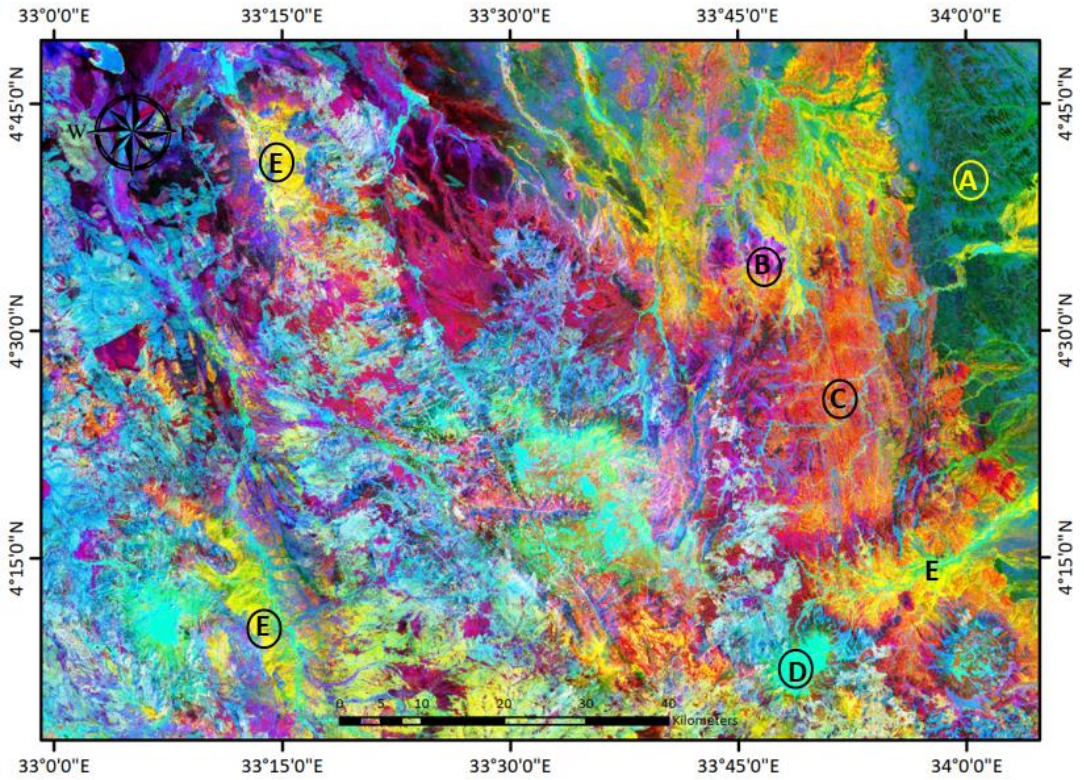

Figure 5.6: Landsat 7 ETM Principal Component Analysis PC2, PC5, PC4 in RGB; ***(A)*** *Green = Extrusive bodies;* ***(B)*** *purple defines basic and ultrabasic rocks;* ***(C)*** *reddish to reddish-orange defines metasedimentary rocks;* ***(D)*** *vegetation cover appears aqua or turquoise;* ***(E)*** *Yellow = alluvial sediments.*

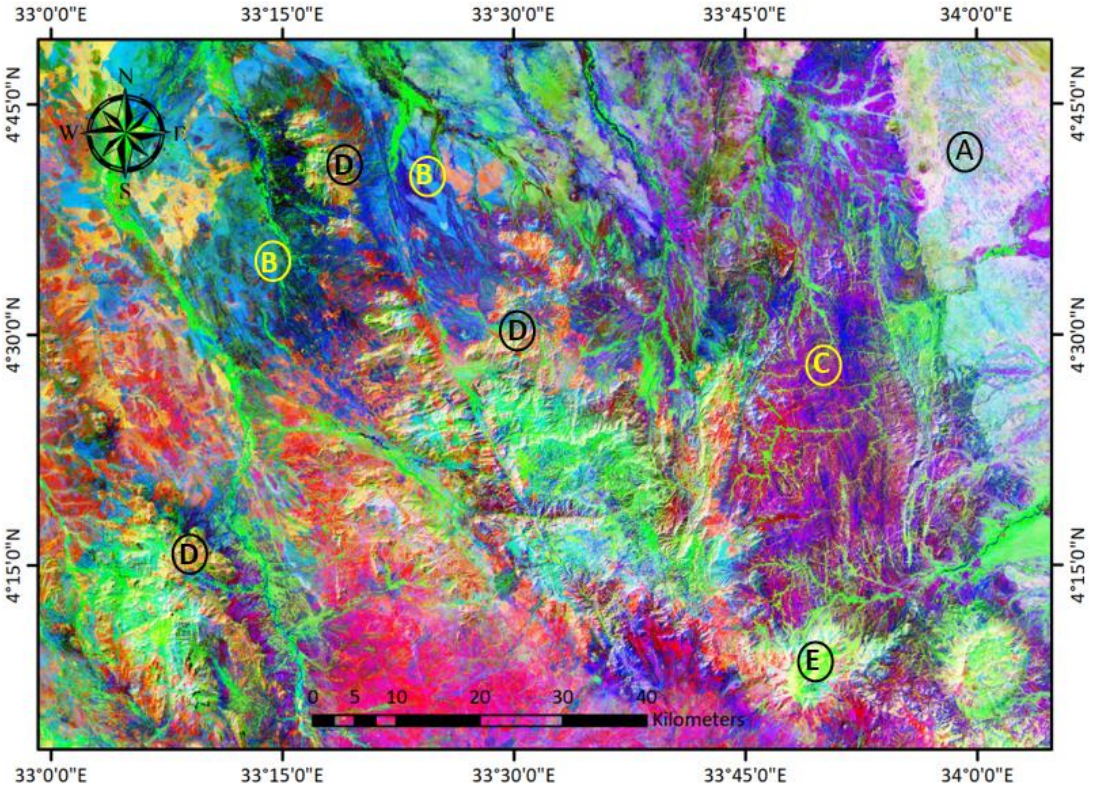

Figure 5.7: Landsat 8 MNF combination in RGB 234; ***(A)*** *Extrusive bodies are displayed in bright colour pink* ***(B)*** *light blue=Umm Rwaba* ***(C)*** *Navy blue mixed with maroon=undifferentiated gneisses* ***(D)*** *Old basement complex;* ***(E)*** *shades of green=vegetation cover.*

5.1.4 Supervised Classification

The results of the spectral signature sampled for the lithological features from the Landsat 8 OLI band composite imagery (Figure 5.1 and Figure 5.2) are shown below (Figure 5.8). This result was referenced to the ground observations during the fieldwork to direct the system to compute and analyse the image using a maximum likelihood technique.

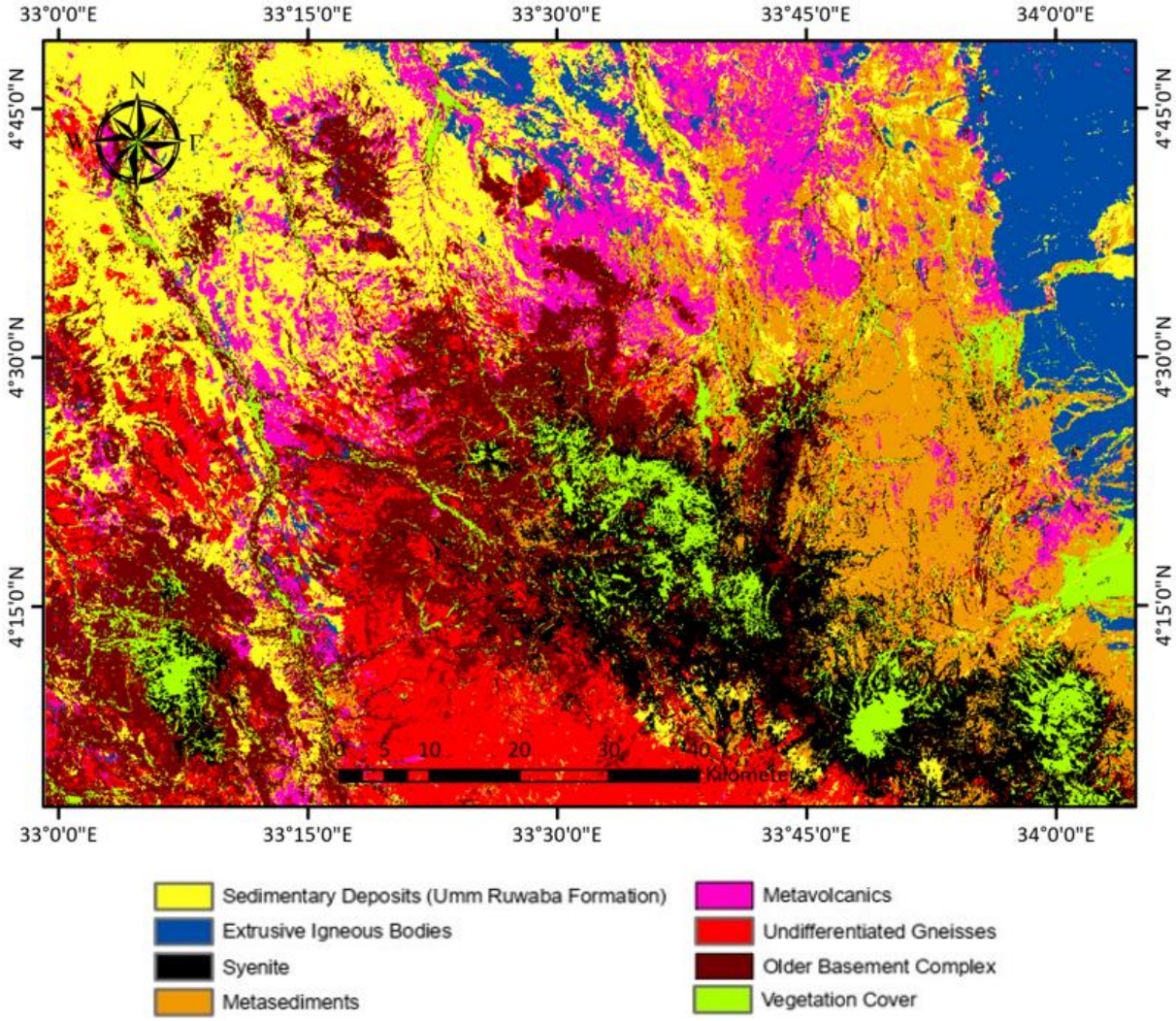

Figure 5.8: Supervised classification of Landsat 8 showing seven classes of geological features and vegetation in green.

5.2 Geological Mapping

The use of legacy data, together with remote sensing techniques combined and field validation, enabled the creation of a geological map for the Kapoeta area (Figure 5.9). The map shows the distribution of major lithologies and outlines the main structural trends in the study area. The application of remote sensing techniques before and after the fieldwork effectively mapped lithological and structural elements and their extent for a wide area. These facts led to the importance of remote sensing in shortening the period of fieldwork which indirectly had an impact on the finances.

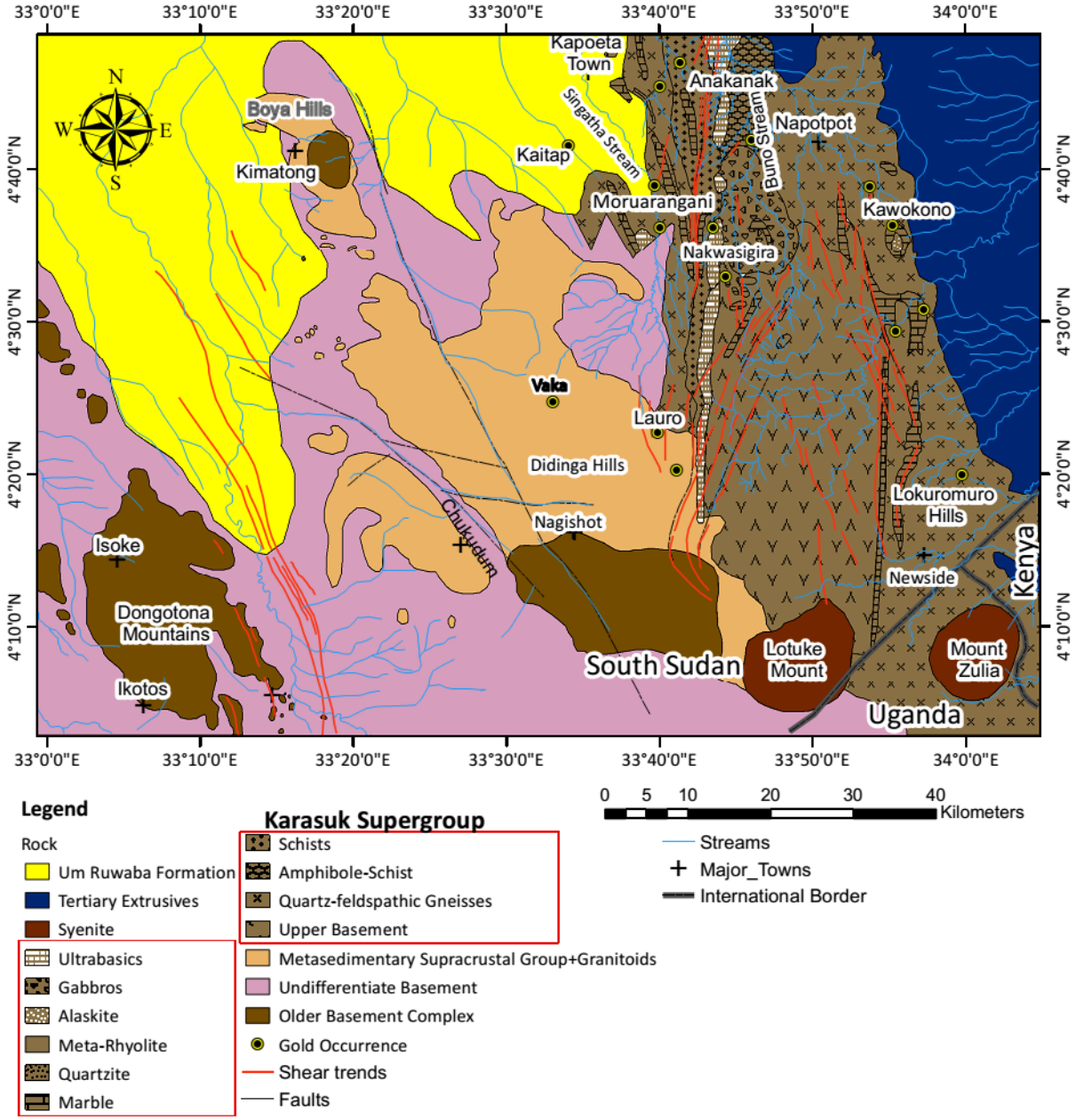

Figure 5.9: Geological map of the study area showing main lithological units of the Karasuk Supergroup (KSG). The boundaries are hypothetical due to the sedimentary cover. Map created using Landsat 8 OLI image of the study area, field data (modified after Belgian Mineral Exploration Project (1983).

5.2.1 Undifferentiated Basement Complex

The undifferentiated Basement Complex of the Archaean age received little attention during this study due to insecurity and poor road access. The account below is based on observation of reconnaissance surveys of selected accessible sites and interpretation from satellite imageries. The group encompasses the Dongotona assemblages and the Didinga and Boya Hills. These units are the oldest lithological group found in the area, which constitute the rocks of the southeastern part of the Sahara Metacraton assemblages and the western Mozambique Belt. During the field investigation, several lithologies were observed between the Dongotona Mountains and the Didinga Hills based on the

lithological and textural variations. The Didinga and Dongotona range share similar characteristics, such as rounded dome-like hills devoid of vegetation. Due to their relative resistance to weathering, the undifferentiated rocks of Dongotona, Didinga and Boya form areas of positive relief (Figure 5.10).



Figure 5.10: Field photographs showing typical outcrops in the Didinga Hills ***(A)*** *Massive rounded dome-shape cliffs of the Didinga Ranges* ***(B)*** *diorite southeast of the Didinga ranges along the road to Lotuke* ***(C)*** *Charnockite fragment with very coarse-grained texture behind the school in Isoke* ***(D)*** *Massive dome-shape outcrop of either Charnockite or the associated rocks in the area around Isoke.*

The common characteristic among these units is that the rocks are coarse-grained and massive. The metamorphosed units are foliated to varying degrees, defined by the alignment of the dark-coloured minerals (biotite and hornblende) relative to the light minerals (feldspar and quartz). The work of the Belgian Mineral Exploration Mission (1982-83) found charnockitic-gneiss with mesoperthitic feldspar and pyroxenes and leucocratic gneisses with biotite and amphiboles oriented parallel to the prevailing structure. On a regional scale, the NW–SE-trending massif hills may correlate with the isolated hilly massifs in northeastern Uganda mapped by Westerhof et al. (2014) between the Karasuk thrust front and the Aswa Shear Zone. The absence of geochronological data from this part of South Sudan makes it challenging to correlate them to the other units in the region. They are probably attributed to Watian or Aruan units around the Torit area.

According to Hunting (1983), these units are attributed to the Watian and Aruan tectono-thermal events, subsequently affected by the Chuan event. This terrane is strongly affected by the NW-SE trending tectonics. Several rock types were observed in Isoke around the Dongotona Hills at the Catholic church mission house and surrounding. These include granites, gabbro, charnockites, gneisses and migmatites. They are all characterised by a coarse-grained texture. The gabbros are melanocratic, while the granites, gneisses and migmatites appear leucocratic. The granites and the gabbros show a foliation.

5.2.1 Gneisses

The gneisses in the area surveyed comprise (I) grey gneiss and (II) quartzo-feldspathic gneiss. The former is poorly exposed around Moruarangani, west of the Singatha River, where several artisanal miners are panning for gold. The latter is found around Khor Jeep, extending eastward up to Kawokono. This tectono-stratigraphic subdivision underlies a major part of the eastern part of the study area and can be traced southward near Mount Lotuke and Zulia. On the Landsat image, the concentration of the shear-induced N-S and NNW-SSE lineament trends are visible, reflecting foliation orientation. The quartzo-feldspathic gneiss at Loyoro stream is invaded by thin pegmatitic veins that vary in lateral dimensions (Figure 5.11B & C). Field measurements of the foliation trend show NE-SW trends with a near-vertical dip.

The quartz-feldspathic gneiss is medium-grained and displays no compositional banding (Figure 5.11B). Alkali feldspar and quartz constitute the major mineral composition with minor biotite. Foliation in the gneiss varies based on the intensity of shearing, from poor to well-developed. The highly weathered biotite gneiss (grey gneiss) is composed of an equal proportion of alkali feldspar and plagioclase relative to the dark-coloured mineral, mainly biotite and possibly hornblende. The rock texture is medium- to coarse-grained and foliated with a general trend parallel to the foliation of the surrounding schists.



Figure 5.11: Field photos of some of the variety of gneisses observed in Kapoeta ***(A)*** *Quartz-feldspathic gneiss with amphibolite band along the Kapoeta-Narus road in Kawokono* ***(B)*** *and* ***(C)*** *Quartz-feldspathic gneiss in Khor Jeep with some elements of migmatisation* ***(D)*** *Biotite gneiss south of Singatha river around Namurunyang.*

5.2.2 Amphibolites

Amphibolites in the Kapoeta area are widely distributed and generally form low-lying exposures. The amphibolite bodies generally trend N-S and NNW-SSE. Three types are recognised based on texture and association.

(i) Those forming thin bodies associated with either the feldspathic gneiss and marbles (Figure 5.11A) or those found together with chlorite schists, quartz-feldspathic schist, e.g., around Buno and Anak Anak area (Figure 5.12),

(ii) the type found south of the study area around Nakwasigira. The Nakwasigira types show areas affected by hydrothermal alteration indicating pyrite enrichment (sample B-10). This amphibolite can be regarded as a potential mineralisation source because it exhibits a hydrothermal alteration factor associated with pyrite enrichment. A thin-section analysis of the sample (B-10) is recommended to evaluate whether the pyrite carries any gold.

(iii) The amphibolite found in Nakwasigira is suggested to belong to the older basement. The amphibolite here is capped unconformably by marble (Figure 5.13).

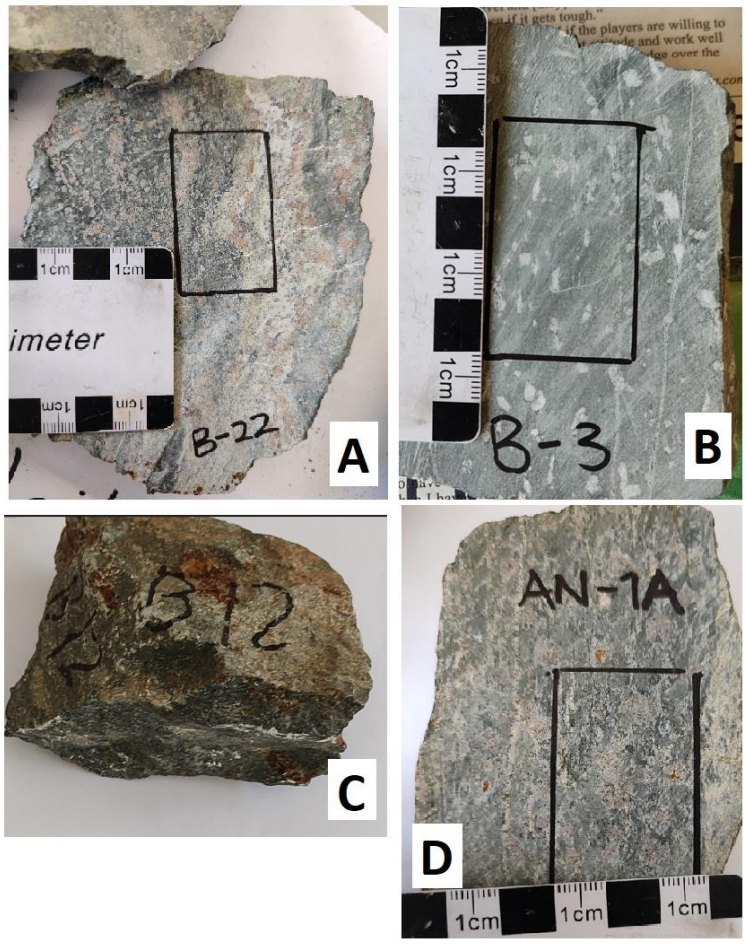

*Figure 5.12: Samples of amphibolites derived from an igneous protolith **(A)**. Amphibolite contains almandine garnet **(B)** Meta-andesite **(C)** meta-basalt with boudinage structure south of Buno stream **(D)** amphibolite with garnet.*

According to the Belgian Mineral Exploration Mission (1983), the amphibolites are challenging to differentiate in the field, whether they belong to the Karasuk Supergroup assemblages or the older basement rocks in terms of the metamorphic regime. However, field relations can help draw the line between the igneous (ortho-amphibolite) and sedimentary (para-amphibolite) protolith types. The igneous protolith-related amphibolite is generally associated with schist, e.g., the type exposed along Kapoeta Narus road in Buno stream. The amphibolite of sedimentary protolith origin occurs as scattered small bodies associated with marble and gneisses.

The amphibolites generally appear dark to dark blue in hand specimens with medium- to fine-grained textures. The mineral composition is mainly amphiboles and plagioclases, with occasional minor quartz, garnet, mica, quartz, and epidote (Figure 5.11).



*Figure 5.13: Field images of the variety of amphibolite **(A)** and **(B)** Amphibolite capped unconformably by marble at Nakwasigira **(C)** Thin bed of amphibolite approximately 5 m wide associated with banded marble east of Moruarangani Hill.*

5.2.3 Schists

The schists are regarded as one of the major components of the metavolcano-sedimentary sequence in most study areas. It probably contains the source for the alluvial gold deposit in the region. Different types are observed during field traverses, including quartzo-feldspathic gneiss, chlorite schist,

muscovite/sericite schist, hornblende schist, and talc schist. These units are masked in many parts, occurring beneath unconsolidated sediments of varying thicknesses. However, in some areas they crop out as low-lying exposures. The chlorite, quartzo-feldspathic and talc schist-associated amphibolites are well exposed along the main Kapoeta Narus road at Buno stream, forming part of the basement greenstone rocks Figure 5.14). The overlying unconsolidated sediments made it challenging to delineate the boundaries of the schists. Well-exposed outcrops are visible in the stream beds. It implies that stream beds should be accorded special consideration when mapping this region.

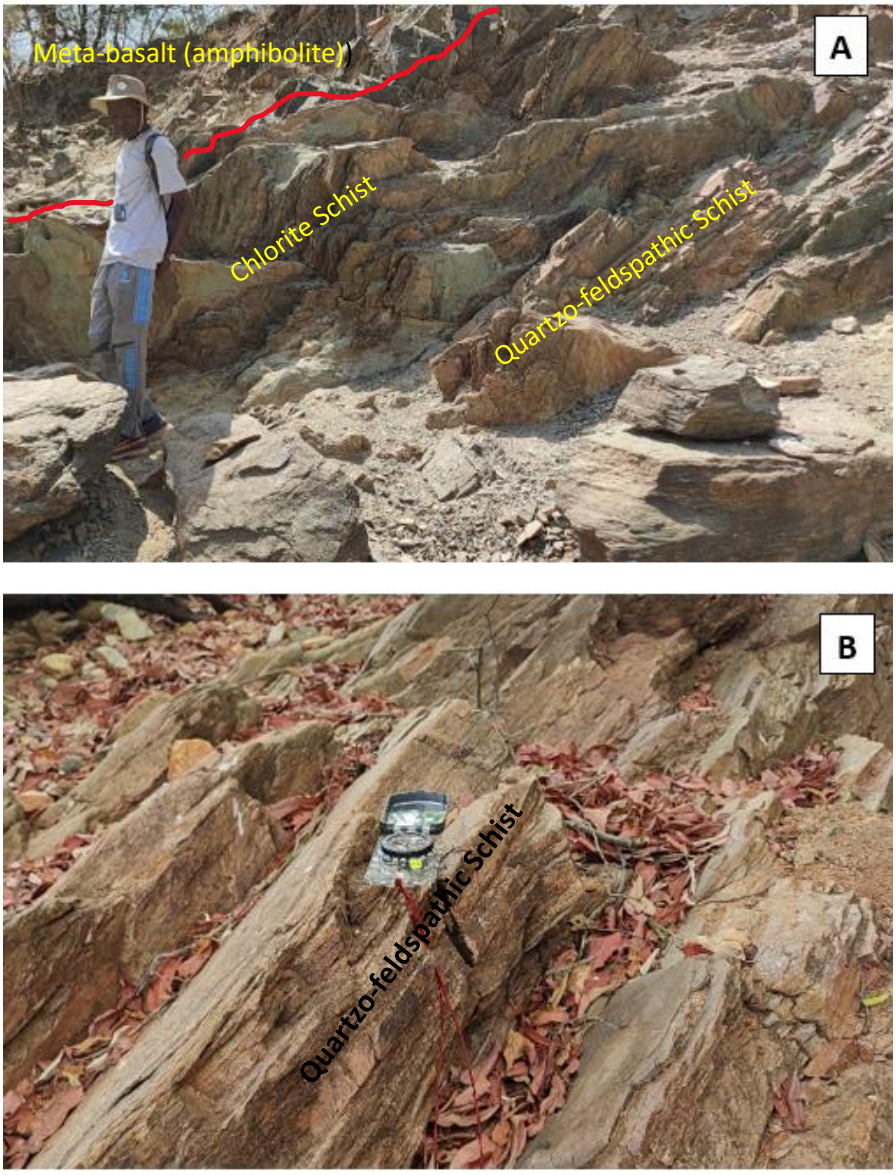

*Figure 5.14: Field photos showing **(A)** Chlorite schist around Buno streams along the Kapoeta-Narus highway and **(B)** Quartzo-feldspathic schist around Anakanak streams east of Kapoeta town.*

5.2.4 Meta-Rhyolite

Meta-rhyolite bodies were encountered a few kilometres to the east and southeast of Kapoeta town, about 2.5 km from the Kapoeta Narus road south of Buno stream, Moruarangani Hill in Namurunyang,

Napotpot. These units outcrop tens of metres above the general ground level. The meta-rhyolite here is characterised by fine-grained and intense shearing. Weathered surfaces are dark, reddish-brown to dark-brown, whereas the fresh surface is pinkish due to the dominance of alkali feldspars. The Moruarangani Hill meta-rhyolite contains shearing-induced quartz veins ranging from about 10 cm or more long and ~ 1 cm or less. The quartz veins trend in the N-S direction parallel to the shearing direction, affecting the host meta-rhyolite. Figure 5.15 shows sheared boulders of meta-rhyolite about 300 m east of Moruarangani hill.



Figure 5.15: Field photo showing meta-rhyolite fragment about 150 m east of Moruarangani Hill, Namurunyang area.

5.2.5 Marbles

Marbles are the most common metasedimentary rock in the study area, showing orientations between N-S and NNW-SSE. Two types are observed showing distinct characteristics, which implies that they are of different origins: (i) the banded variety and (ii) the white marble. The marbles are generally of a medium to coarse-grained texture. The banded marbles are poorly exposed. In most parts, they are covered with sediments of varying thicknesses. The Belgian Mineral Exploration Mission (1982) defines them as part of the older basement lithologies. They exhibit Tofani (Swiss cheese) like weathering and a buff colour (Figure 5.16). Around Buno police station, this variety of marble is intruded by a stockwork of NNW-SSE trending quartz veins but shows no signs of mineralisation. The white marble, on the other hand, exists as outcrops forming a ridge-like hill about 100 metres above the general ground and as low-lying exposures.

The marbles in general are dominant compared to the associated quartzites but less that schists. The thin amphibolites are occasionally found hosted in the marbles are probably dolomite.

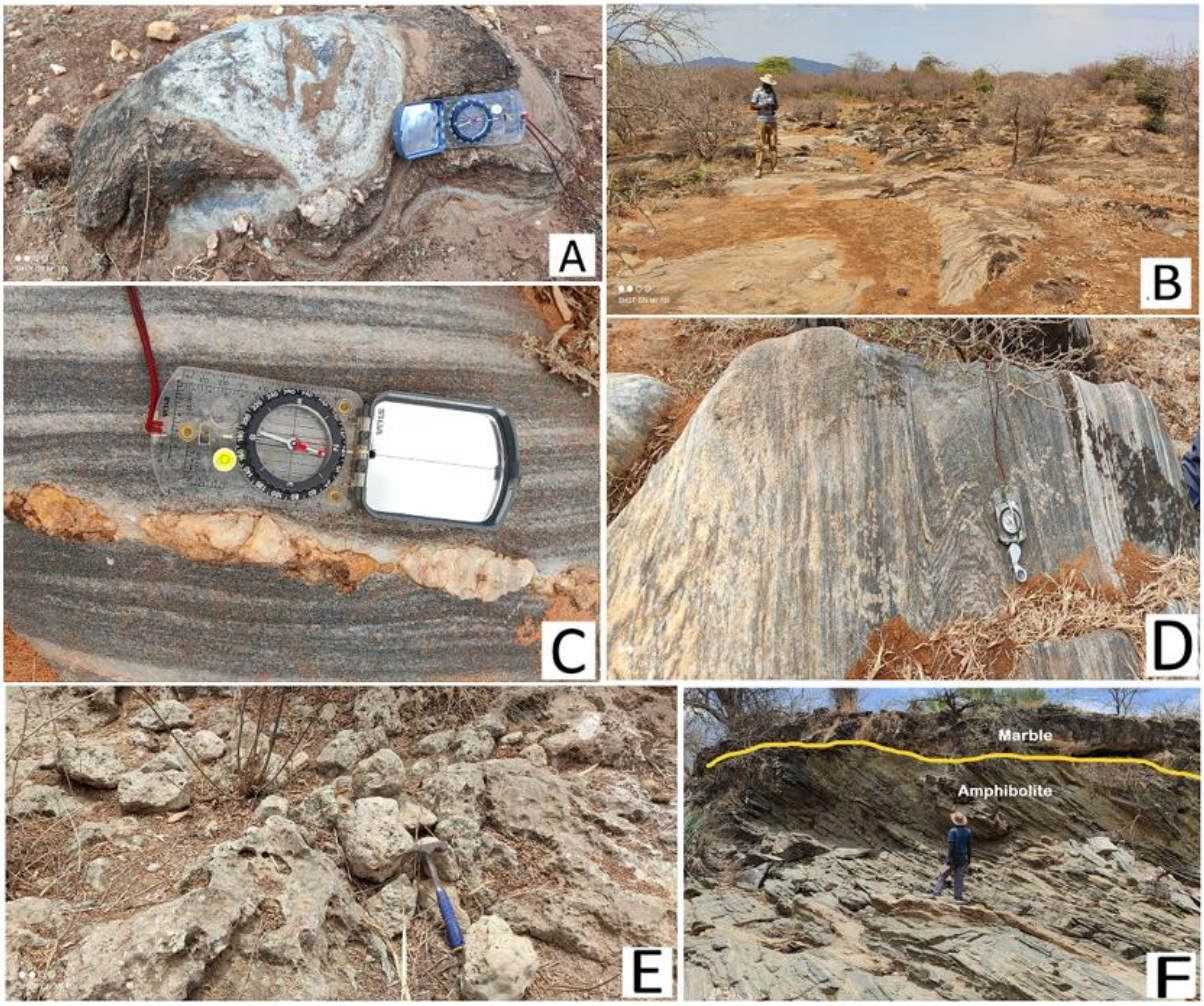

Figure 5.16: Field photos showing banded marble of Kapoeta; ***(A)*** *Marble with thin layers of amphibolite* ***(B)*** *Banded marble around Namurunyang;* ***(C)*** *Marble with a boudin of quartz* ***(D)*** *Evidence of shear effect in marble* ***(E)*** *Tofani (Swiss cheese-like weathering) east of Moruarangani Hill;* ***(F)*** *Marble lying unconformably on amphibolite near Nakwasigira.*

5.2.6 Quartzite

Quartzite bodies are widely distributed in the area. In areas where the quartzites occur, they are particularly associated with the marbles, such as those forming ridge-like bodies at Anakanak, a highly brecciated type around Kangatung and the sheared type at Lokwamur village. The quartzite bodies generally trend between 330° and 340° NNW-SSE. Generally, the quartzites can be divided into two types based on the mineral composition; (i) the first variety includes crystals of iron-rich amphibole mineral that may reach 3 cm in length or more with varied lateral dimensions, (ii) the second type is composed mainly of quartz with no inclusion of other minerals. According to the Belgian Mineral Exploration Mission (1983), some of the area's quartzites are manganese garnet and graphitic bearing. The manganese garnet-bearing variety is characterised by a fine-grained texture and is composed of quartz and about half of the idiomorphic spessartine grains, and a thin film of black dust coats the whole rock. The latter's graphite forms folded flakes that do not follow the preferential orientation.

5.2.7 Quartz Veins

The quartz veins are found in different parts of the study area associated with the metavolcano-sedimentary rocks. Three sets are observed based on orientation, the N-S, NNW-SSE, and NE-SW trending veins. These veins vary in size and length. The different orientation trends of these veins suggest that the veins resulted from multiple episodes of hydrothermal fluid activity in the area at different times. Among the veins, the N-S and NNW-SSE are the most interesting group. The N-S trending lineaments are found in a zone of sheared contact between the marbles and schists. These are covered by metasedimentary rocks not limited to schists and marble. The most intriguing characteristic of these quartz veins compared to the other veins in the area is the occurrence of pyrite, which can be considered the first visual typical pathfinder mineral for Au (Figure 5.17). However, the rest of the vein shows no alteration fingerprints to suggest their potentiality for hosting gold deposit. Generally, all the veins observed indicate that the host rock attitude dictates the orientation of all the quartz veins.

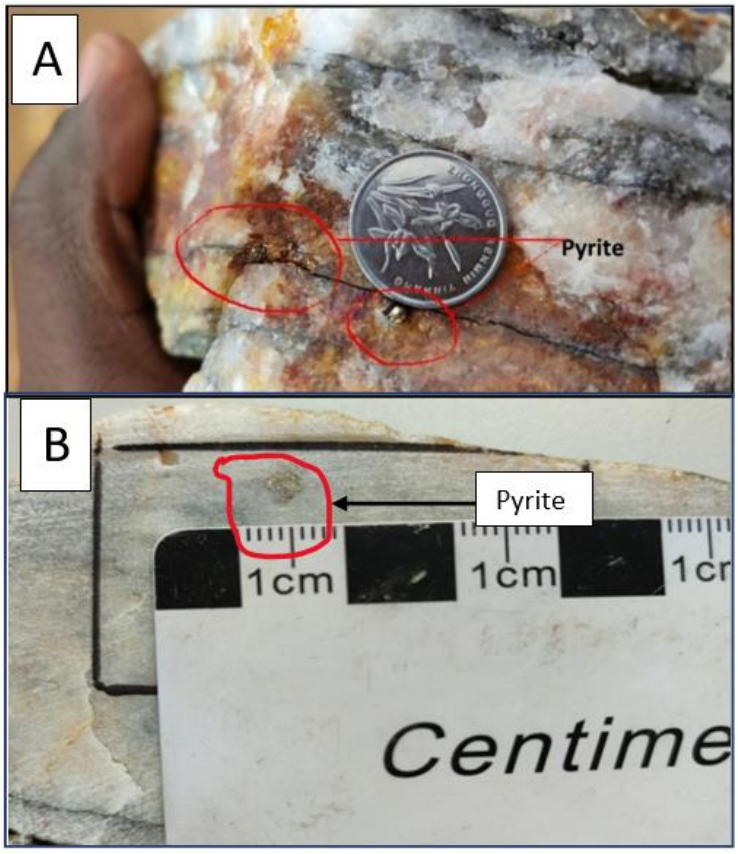

*Figure 5.17: Field photos of vein quartz **(A)** Quartz vein showing pyrite and oxidation from Moruarangani area a few kilometres south of Kapoeta town **(B)** quartz vein with pyrite after slicing the sample for thin section.*

5.2.8 Gabbro

Boulders of a gabbro body are located south of Buno stream on the Landsat 8 image; it appears to be well exposed, forming an area of positive relief. They are interpreted as a later stage of the Karasuk

assemblages. South of the Buno stream, the main gabbro body is capped by vast masses of Karasuk marbles (Belgian Mineral Exploration Project, 1980). Several boulders were encountered during a field excursion along the strike of the Buno stream. The rock exhibits a melanocratic appearance on the weathered surface and has a coarse-grained texture (Figure 5.18). The rock shows no effect of foliation or shearing. This massive gabbro is among the youngest intrusive bodies that invaded the Karasuk Supergroup metavolcano-sedimentary assemblages. Several bodies mapped by the Belgian Mineral Exploration mission west of Monoropus are associated with NS and NNW faults. However, it is too early to correlate them to the ultramafic bodies, or the gold reported in the Mirian-aged rocks south of Juba (Kinyeti metasedimentary rocks?).



Figure 5.18: Field photo showing boulders of massive gabbro 2 km south along Buno stream bed.

5.2.9 Acidic Intrusions

Two intrusions were encountered during the field investigations: a granite body and alaskites. The granite body is located a few kilometres northeast of Kapoeta town. The granite body is massive and occurs in the form of boulders. The rock appears to be older than the alkaline intrusions (Lotuke and Zulia) described above but could be older or younger than the syntectonic granite described by the Belgium Mineral Exploration Mission (1982) west of Lobur. The granite body exhibits a medium-grained texture and is composed mainly of alkali feldspar (microcline and orthoclase), plagioclases, quartz, and dark-coloured minerals, which might be biotite or hornblende or both. The alaskites around Kawokono area intrude into the marbles and quartz-feldspathic gneisses. Texturally, the rock composed of large crystals mainly of alkali feldspars, probably microcline or orthoclase and quartz.

5.2.10 Basalts and Rhyolite Bodies

The basalts with some rhyolite bodies dominate the northeastern part of the study area. They form sharp contact with quartzo-feldspathic gneisses and the marbles. These rocks are well exposed in the form of hills and low-lying bodies. In most areas, the basalts are highly jointed, exhibit a fine-grained texture, are dark to dark grey, and occasionally show a greenish colour on the weathered surface. The rhyolite appears brownish to dark brown and pinkish on the fresh surface. These extensive extrusive igneous bodies have a distinct appearance in satellite images. Examination of the satellite images for the Narus area shows several dyke-like structures (Figure 5.19). At Loyoro River, the basalt is conformably underlain by the rhyolites. Late silica-rich fluid flow was common; this activity resulted in the development of radiating quartz and the widespread occurrence of white agate.

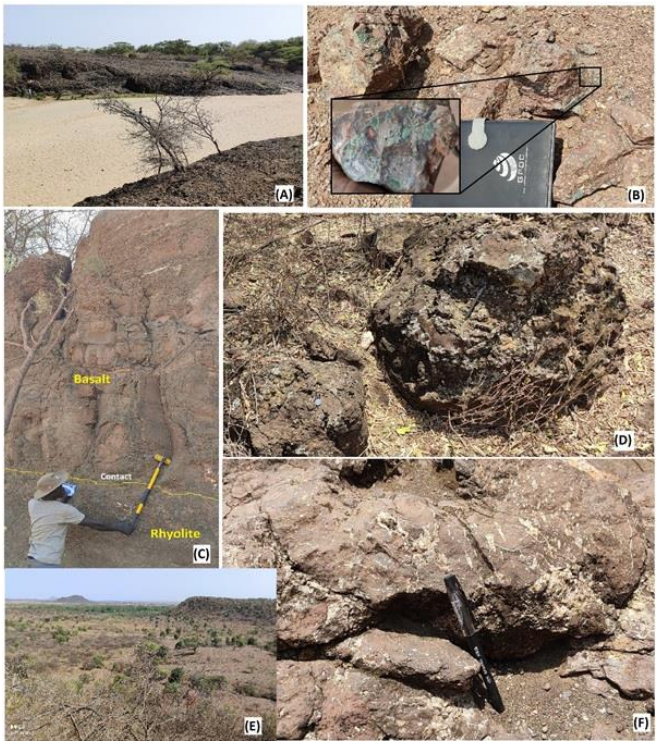

Figure 5.19: Field photos of volcanic rocks ***(A)*** *Basaltic lava flow at Loyoro stream* ***(B)*** *Rhyolitic lava with a green mineral forming a phenocryst or amygdale* ***(C)*** *a contact between basalt overlying rhyolite at Loyoro stream* ***(D)*** *Rhyolitic boulder with vesicles at Napeikeng Hill about two kilometres behind the county headquarters* ***(E)*** *outcrops of basalt west of Narus around Lapachol* ***(F)*** *Rhyolite boulder with quartz.*

5.3 Structural Interpretation

The structural interpretation is based on field observation, documentation, and image interpretation of structural elements in the area. It encompasses recording of the structural trends and deformation products. The results are then compared with the regional structures and their tectonic origin.

5.3.1 Lineament Extraction

Lineament analysis is an essential step in geological and geophysical studies, providing valuable information about the structural features of an area. In lineament analysis, various image processing

and interpretation techniques are employed. However, field validation becomes crucial to ensure the accuracy and reliability of the obtained results.

The extracted lineaments for both automatic and visual methods were examined, and the data were compared against the significant structural elements such as shear trends, faults, and major joints on the geological map. The automatically extracted data were subject to RockWorks 17 edition platform to generate a rose diagram to analyse the lineament's frequency distribution to the orientation. In the rose diagram, an individual line becomes an element regardless of length. The rose diagram of lineaments mapped four orientations, N-S, NNW-SSE, NW-SW, and NE-SW (Figure 5.23). The structural analysis discussed here is based on satellite image analysis combined with limited field data. The structural trends interpreted can be related to the work of Hunting (1976), as shown in Table 5.1.

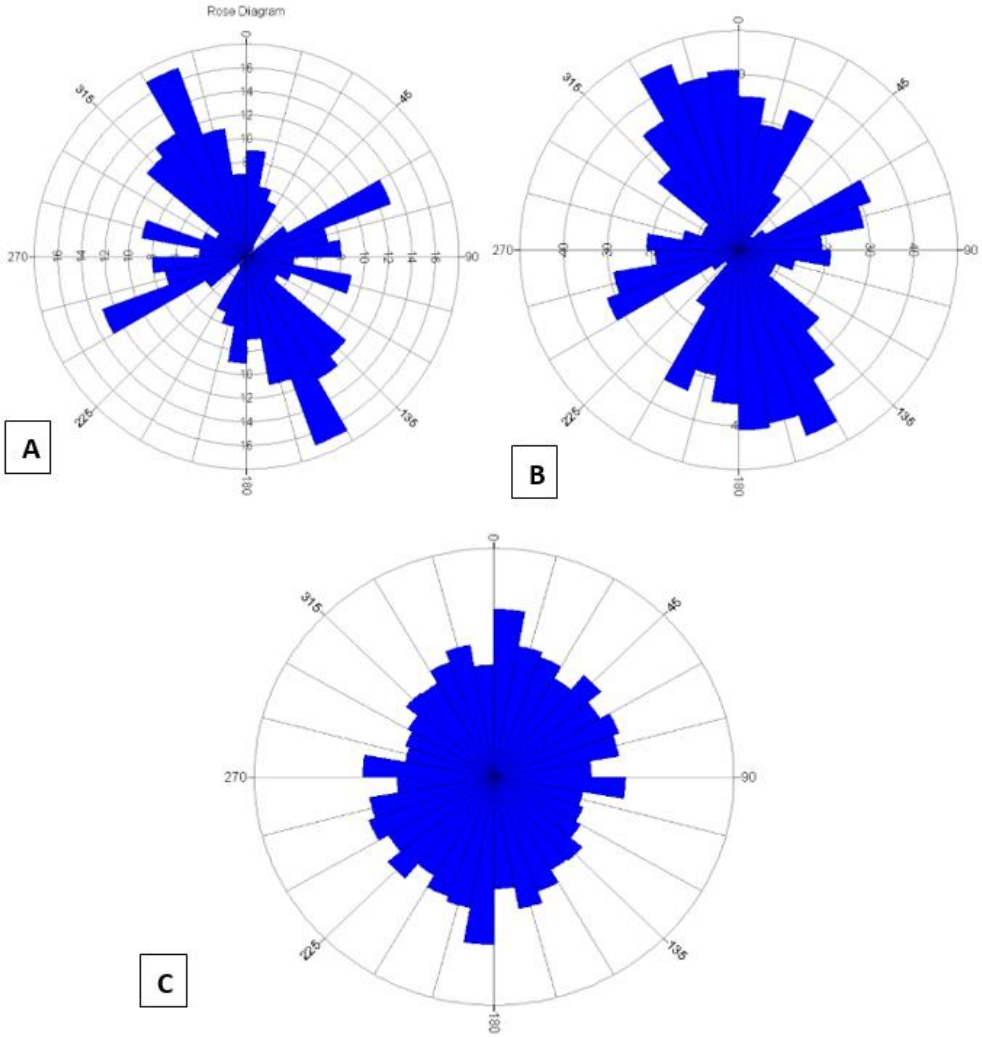

*Figure 5.20:Rose diagram showing the main structural trends mapped using **(A)** Visual interpretation extraction method from SRTM hillshade image **(B)** Visual interpretation from PCA 1 HVS enhance Landsat 8 Image **(C)** PCA 1 HVS sharpened automatic extraction.*

In the second approach, lineament analysis was performed using the QGIS 3.20.1 software. The latter software was used on Shuttle Radar Topography Mission - Digital Elevation Model (SRTM-DEM) of the

study to produce hill-shade images from four illumination directions, NE-SW, E-W, NW-SE, and N-S, with the sun elevation set at 45° to achieve optimal visualisation. The result shows that the area is affected by three major deformation regimes: NW-SE, NNW-SSE to N-S and NE-SW trending structures. The structural pattern is generally analogous to that established by Hepworth & Macdonald (1966); Almond (1969); Vail (1976); Berhe (1988); Fritz et al. (2013); Westerhof et al. (2014) for the East Africa region.

By employing the hill-shade technique, the QGIS software simulated the effects of light and shadow on the terrain, enhancing the visibility of lineaments. This visualisation technique is particularly useful as it allows for better identification and interpretation of structural features.

Table 5.1: Main tectono-thermal events registered in South Sudan (Hunting 1976)

Age (Ga)	Tectono-thermal event	Structural trend
2.88	Watian	East-West, (Leggo, 1974)
~ 2.55	Aruan	N, NNE, (Hepworth and Macdonald, 1966; Leggo, 1974)
~1.0	Mirian	E-ENE (Leggo, 1974, Lavreau)
0.65-0.4	Chuan (Aswa)	NW, NNW (Dominant trend in Kapoeta)

5.3.2 Folds, Faults and Joints

On a megascopic scale, the fold structure can be deduced from the satellite and SRTM image for the Kapoeta and Didinga Hills area as an anticline represented by the Kawokono Bull eye structure (Figure 5.1 & Figure 5.21A). This might be associated with the evolution of the alaskite, which occupies the central position on a hill west of Didinga Hill and a tight fold south of the Kawokono anticline. On a mesoscopic scale, several fold structures are registered in the field in the metasedimentary rocks. Strike and dip readings recorded from the schists and associated amphibolites suggest a tight fold. Observation of the marbles and quartzite around the Namurunyang area suggests that the fold structures become gentler from east to west (Figure 5.21). All the fold axes measured from the field and those deduced from the satellite images show a general trend between N-S, NNW-SSE and NW-SE.

Several trends can be deduced from the Landsat images, and their origin is intimately related to the regional tectonic regimes. Faults observed on the satellite images and the ground are mostly attributed to the shear kinematics and geometry in the area. The prominent fault structures are seen on the satellite image west of the Didinga Hills, trending NW-SE, WNW-ESE and E-W. Joints are common, forming several sets; the prominent set that dominates outcrops NW of the Didinga Hills, has created the ridges described above. Megascopic joint sets are seen in the satellite images.



Figure 5.21: Field photos showing fold structures in banded marble around Moruarangani, approximately 10 km south of Kapoeta town.

5.3.3 NNW-SSE and N-S Structures

In the field, points where rock attitudes were recorded (metavolcano-sedimentary assemblages) show that the N-S and NNW-SSE oriented sets are mainly confined to the Karasuk Supergroup rocks. The metavolcano-sedimentary lithologies recorded a steep dip angle between 60°and 70° with three dip directions, W, SW, and NE. On the SRTM-DEM hill-shaded image, the N-S and NNW-SSE trends predate the NE-SW structures (Figure 5.23). These trends correspond to the regional tectonic E-W compressional events in the Arabian Nubian Shield and Mozambique Belt event, depicting crustal shortening described in Mosely (1993). According to Mosely (1993), after the first event, which involved transforming an essentially sedimentary sequence to paragneisses, subsequent phases of deformation followed. The subsequent phases record progressive shortening across the orogenic belt during the collision between two major continental fragments (East and West Gondwana). It involves extensive structural reorganisation and isotopic resetting (Mosely 1993). During the progressive 630-580 Ma event, regional N-S to NNW-SSE trending ductile shear zones (generally sinistral) were produced (Mosely 1993). The main structural features of the Karasuk Group in Uganda were developed during the second tectonic phase of intense shear folding, in which a northerly striking foliation was produced (Clark 1967).

According to Westerhof et al. (2014), the Karasuk Group and the evolution of the West Karamoja group are related to the Karamoja belt development. The formation of the Karamoja Belt and tectonic emplacement of rocks belonging to the Karasuk Supergroup and West Karamoja Group are related to the first E–W compressional event, magmatic emplacement of some of the Neoproterozoic in-situ granitoids is supposedly related to the second N–S compressional event. It stems from E–W compression resulting from the collision and amalgamation of East and West Gondwana. The amalgamated East and West Gondwana collided with the Sahara Metacraton in an N-S compressional event (Westerhof et al., 2014).

Elsewhere in Ethiopia and Kenya, the development of the Karamoja belt-related domain commenced with the closure of a rift and small ocean basin system, during which thrust slices of the dismembered basement and oceanic crust, including ophiolitic ultramafics, was emplaced (Kazmin et al. 1978, Pohl and Horkel 1980). According to Abdelsalam and Stern (1996), the Arabian Nubian Shield's deformation belts include sutures encompassing arc-arc and arc-continent type and post-accretion structures. These include the north-trending shortening zone, northwest-trending strike-slip faults, and minor northeast-trending and dextral strike-slip faults. The N-S shear can be related to the Mozambique orogeny. According to Hepworth (1967), it is related to the Mozambiquian orogeny with north-westerly trending lineaments. Furthermore, Aruan rocks (Table 5.1) cut structural belts of tightly folded and foliated rocks with thick mylonites in the middle of the southern West Nile.

5.3.4 NW-SE Trends

The NW-SE structural trends dominate the Landsat 8 (Figure 5.6) and the SRTM DEM images (Figure 5.23). Its effect is evident in the reworked Archaean Basement Complex of the Sahara Metacraton west of the study area. The NW-SE structures are explained by Berhe and Rothery (1986) and Berhe (1987) due to shearing along north-westerly trending faults. Moreover, these structures are interpreted as resulting from the tectonic escape of the NW corner of the proto-Congo Craton. The NW-SE structural trends mark the period of refoliation zones 'Straightening Zones', a term Hepworth (1967) coined to denote the Watian (Table 5.1). Vail (1983) suggested that this late tectonic event is now characterised by long, narrow NW-SE trending fold shears. The north-westerly faults have long histories dating from the Palaeozoic through the Jurassic to the Tertiary (Berhe, 1988). Hunting (1979), using photogeology, defined four tectono-thermal events in South Sudan (Table 5.1) that correlate with those found in Uganda (Hepworth, 1967). The dominant NW-SE structures represent a series of refoliation zones like the photogeological expression interpreted by Hepworth (1967) in northern Uganda.

Kujjo et al. (2019) used a horizontal gradient filter on the gravity field data in the northeast-southwest direction to outline the expression of any of the major linear geologic structural patterns of the

Precambrian basement and lithologic boundaries in South Sudan that are mostly trending northwest-southeast. The result shows the effect of the NW-SE set to dominate much of South Sudan (Figure 5.22).

The evolution of NW-SE structural lineaments in Kapoeta is related to the development of the Aswa and Nyangere Shear Zones. These shear zones are among the NW shear-zone patterns within the Arabian Nubian Shield, which have different orientations relative to the ophiolite-decorated sutures compared to the rest of the shears (Fritz et al., 2013). The shear zones are emplaced approximately parallel to the NNW-elongated belt-aligned arc–arc suture (Fritz et al., 2013). Three shear structures (Aswa Shear Zone, Nyangea shear and Mutito shear zone) converge at the southern end of the Arabian Nubian Shield (Fritz et al., 2013), which suggests a common evolutional genetic origin. Kinematic studies reveal that the early phases of deformation were characterised by low vorticity sinistral shear (accompanied by a significant pure shear component) and subsequent localised dextral shearing (Bauernhofer et al., 2008b). The shear zones are high-temperature sinistral shear zones (Shackleton, 1996; Bauernhofer et al., 2008a) with a strong component of coaxiality. The NW-SE trending deformation is pronounced in the reworked Archaean rocks to the west. To the east of the Didinga Hills, the lineament swings to the NNE-SSW (Figure 5.23), obliterating the north-south footprints of the Karasuk Supergroup dominated by NNW-SSE lineaments. On the SRTM-DEM image, the Karasuk Supergroup of South Sudan in the Kapoeta area appeared to be affected by NNW-SSE, with a vertical dip. In the field, the Karasuk Supergroup rocks exhibit an N-S trending orientation.

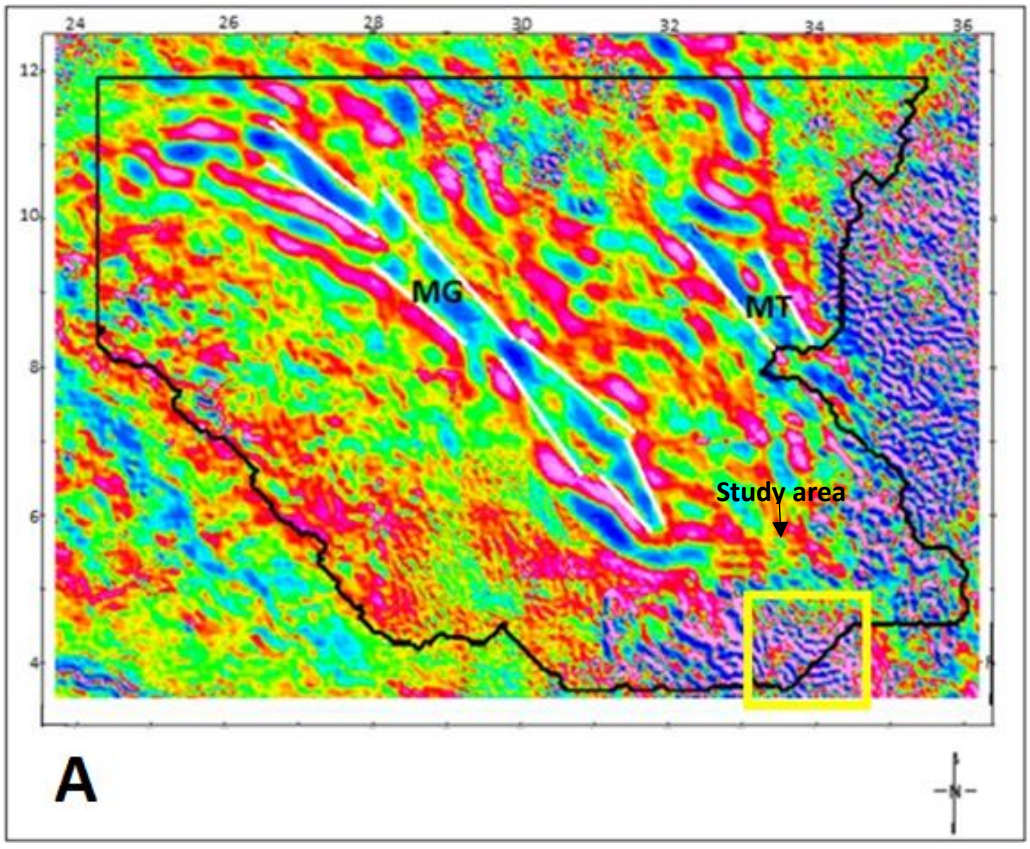

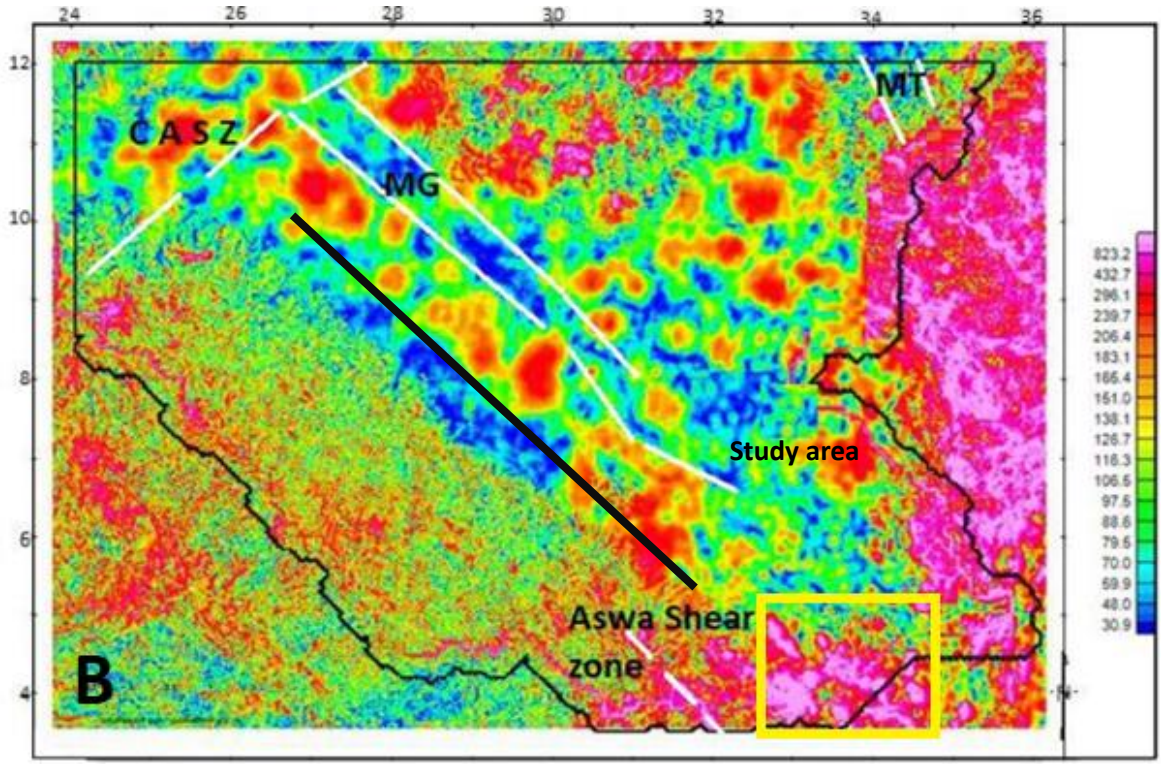

Figure 5.22: Geophysical data of South Sudan showing the study area ***(A)*** *Bouguer anomaly acquired from a horizontal gradient in the northeast-southwest direction indicating northwest-oriented geological structures;* ***(B)*** *Basement topography determined from employing an analytic signal to gravity data. Locations of the Central African Shear Zone (CASZ) and the Aswa Shear Zone are shown as study areas in the yellow box; MG: Muglad Basin; Melut Basin (After Kujjo et al., 2019). Near-surface basement areas are highlighted in red, and deeper segments are defined by blue.*

5.3.5 NE-SW Structures

The NE-SW trending shear structure to the east of Didinga Hills Figure 5.23 shows similar characteristics to the Aswa shear zone in southwestern Juba in South Sudan. This pattern has been studied by Katumwehe et al. (2015) using an SRTM-DEM image, airborne geophysical data, and magnetic image which shows that the Aswa shear zone bifurcates into several NW-trending splays. The work of Westerhof et al. (2014) in northernmost Uganda segments suggested that this bifurcation phenomenon is associated with subduction and head-on collision involving the Sahara Metacraton and the proto-Congo Craton. The N–S compression gave rise to E–W extension and opening of the northern portion of the NW–SE striking ASZ, which, in turn, allowed the emplacement of magmas of a granodioritic nature at around 0.66 Ga.

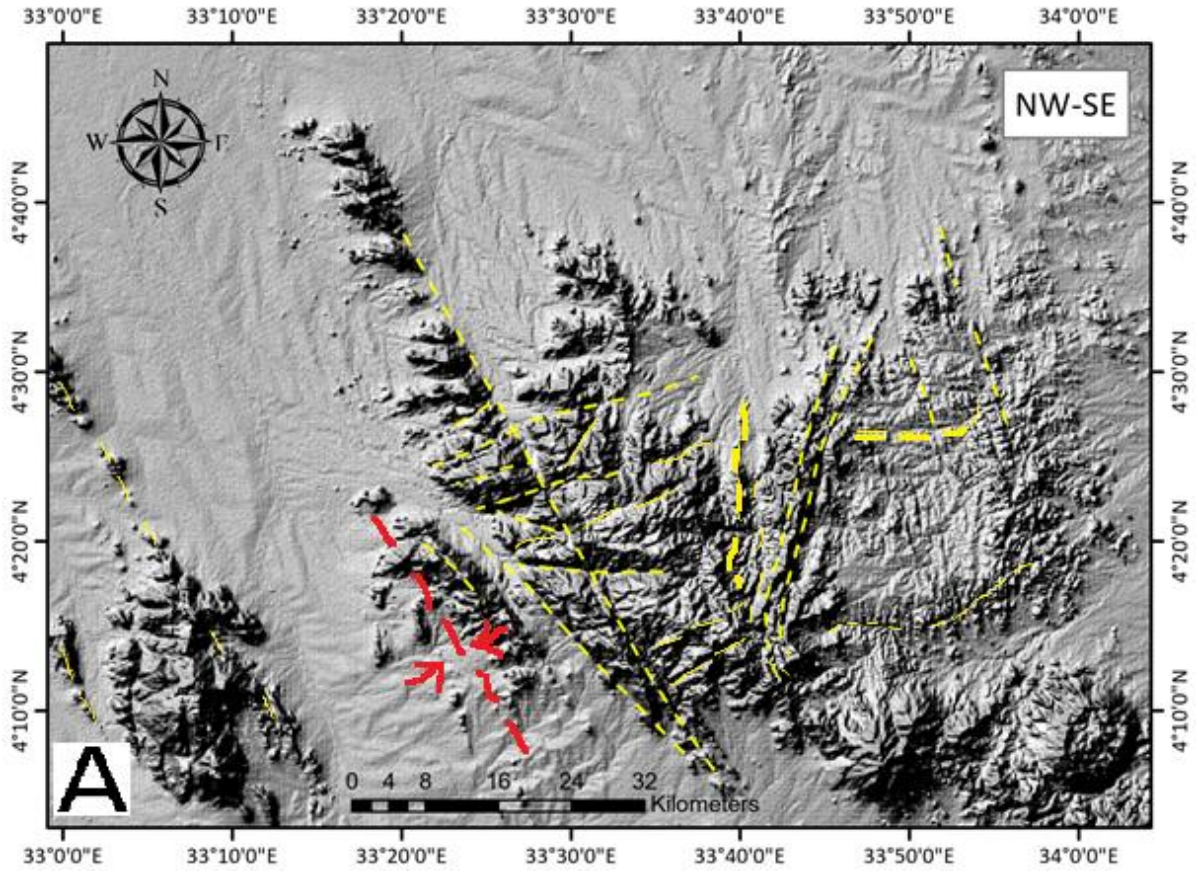
33°0'0"E
33°10'0"E
33°20'0"E
33°30'0"E
33°40'0"E
33°50'0"E
34°0'0"E
4°40'0"N
4°30'0"N
4°20'0"N
4°10'0"N
N
W
E
S
NW-SE
A
0 4 8 16 24 32
Kilometers

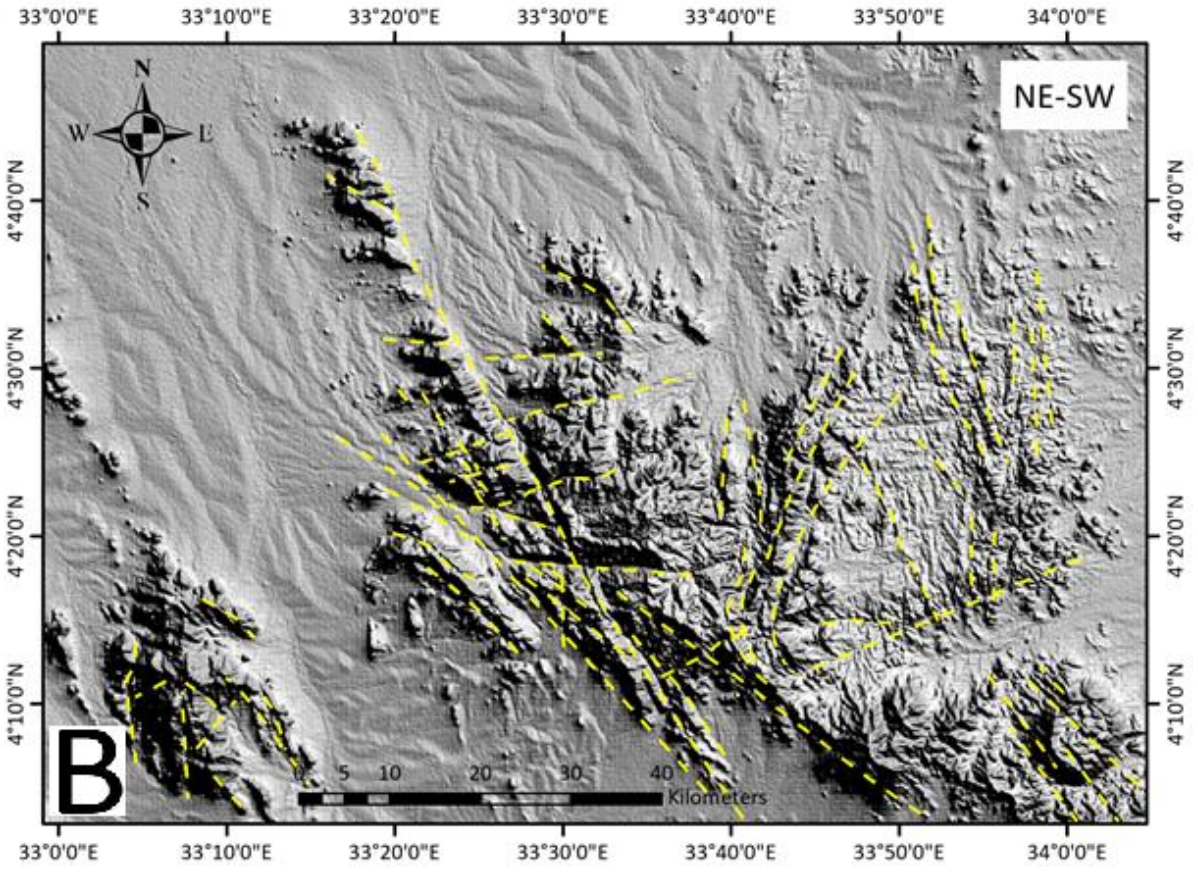
33°0'0"E
33°10'0"E
33°20'0"E
33°30'0"E
33°40'0"E
33°50'0"E
34°0'0"E
4°40'0"N
4°30'0"N
4°20'0"N
4°10'0"N
N
W
E
S
NE-SW
B
0 5 10 20 30 40
Kilometers

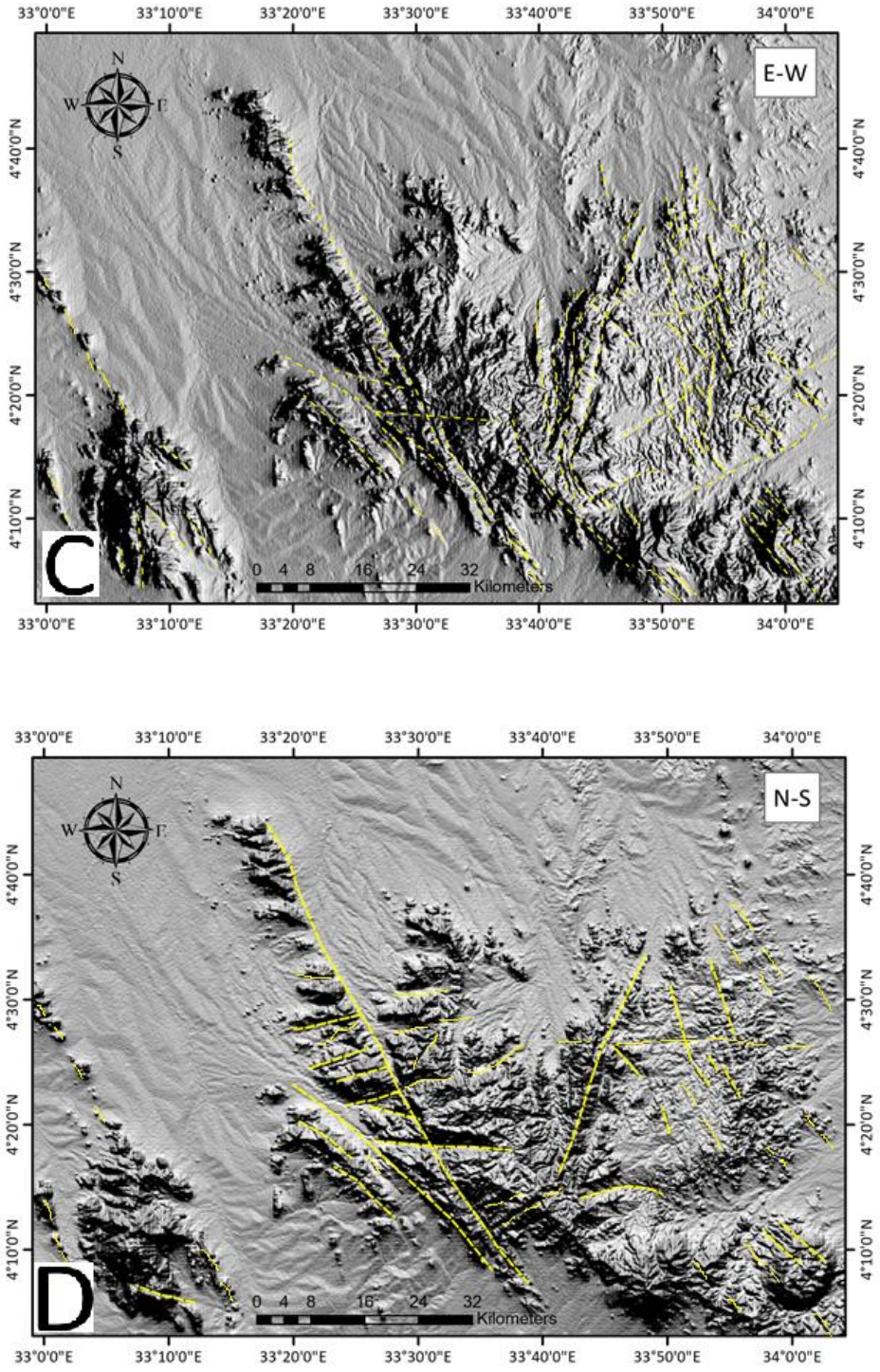

*Figure 5.23: SRTM-DEM map showing major structures and trends in the Greater Kapoeta area with the sun elevation angle at 35°; **(A)** Hill-shade from illumination from 315° (NW-SE); **(B)** illumination direction 45° (NE-SW); **(C)** illumination trend 90°(E-W); **(D)** illumination direction 360° (N-S).*

5.4 Mineralisation

The discovery and exploitation of alluvial and eluvial gold deposits by artisanal miners in the Kapoeta area started before the independence of the then-united Sudan (Adde, 1984), around the 1940s or earlier (Belgium Mineral Exploration Mission, 1983). It is believed that the Belgian project exploration

benefited from the artisanal miners' early work in conducting their exploration campaign. There are no documented reports of how much gold is produced annually and how long it has been produced. Based on this fact, it is impossible to quantify the local diggers' volume of gold production from this region over the years. However, the Belgian Geological Survey Mineral Exploration (1980) estimates that artisanal miners' gold produced from this region from the placer deposit between 1979 to 1983 amounts to approximately 100-200 kg per annum.

The gold deposits in Kapoeta can be divided into primary and secondary. The primary deposits, which are believed to be based on limited field evidence, suggest that the deposits are associated with metavolcano-sedimentary sequences. The secondary gold deposits are of placer type, and these are widely distributed in the area (Figure 5.25). It is commonly accepted among the natives that all the seasonal rivers in Kapoeta contain gold deposits.

5.4.1 Placer Gold

Placer gold deposits are widely distributed in the Kapoeta area (Figure 5.25). Based on the current field investigation, the placer gold can be divided into three main groups; (I) gold panned in the stream beds suggests transportation from some upstream locations. (II) gold panned from the overlying sediments, which suggests that the gold was deposited simultaneously with the overburden overlying the metavolcano-sedimentary units of the Karasuk Supergroup. They can be of an eluvial nature, as reported by the Belgians. However, where panning is taking place currently, there is no mention of deposits recovered from the country rock. (III) gold recovered from ancient streams buried under the overburden; an example is at Kaitap. Here the artisanal miners dig vertical pits approximately 10 m deep and then go horizontal following the trend of the stream. The idea is to collect sand and gravel, bring them to the surface and pan for gold. This case explains the use of excavators by some small-scale companies working between Kapoeta and Lauro. In Kawokono, local diggers concentrate their activities on recovering alluvial sediments deposited between fractures of the marble boulders and panning the sediments using the wind technique. The work of the Belgians in this part of Kapoeta encountered a primary deposit associated with the marble.

Figure 5.24 shows sites where artisanal mining activity is currently happening. The areas include Kawokono, Buno River, Anakanak, Kaitap, Namurunyang and Nakwasigira. In Namurunyang, the natives are panning from two sites in the stream bed of Singatha River, which drains near the foot of Didinga Hills and along the stream's banks. The drainage network forming the Buno River suggests that the alluvial gold deposit in the riverbed is associated with the basic and the ultrabasic bodies from where it appears to originate.



Figure 5.24: Field photographs showing workings /activity of the artisanal mining of alluvial gold deposits ***(A)*** *Artisanal mining pit at Kaitap* ***(B)*** *site where overburden has been removed for panning* ***(C)*** *Two Toposa girls panning gold at Buno stream bed* ***(D)*** *shows gold nuggets in the red square recovered from alluvial sediment from Buno stream* ***(E)*** *overburden and basement rocks* ***(F)*** *Open pit where the overburden is recovered using an excavator pan with the Didinga Hills on the horizon* ***(G)*** *Three Toposa girls in Kawokono recovering sediments deposited between marble boulders to be panned for gold.*

5.4.2 Primary Gold

The technique employed for the whole-rock geochemical analysis does not cover the detection of Au in the samples examined. However, based on the field evidence, geochemistry of the trace elements, Landsat 8 image interpretation, and legacy data from the Belgian Geological Survey mission of the 1980s have made it possible to decipher the source of the gold in the area. The extensive geochemical survey analysis by the Belgian Mineral Exploration Project (1983), identified several anomalies of Cr, Zn, Cu, Ni and Co in several locations (Figure 5.25). The origin of the alluvial gold deposit based on geochemical analysis of the trace elements and their correlation with Belgians anomalies and usual association with gold suggests that Cu, Zn, Co, Cr, Ni and As are the potential pathfinders.

Based on the geochemical anomaly map of the Belgium Geological Survey and the current interpretation of the satellite image suggest that the primary gold host lithologies are N-S and NNW-SSE trending pyrite-rich quartz veins and metavolcano-sedimentary sequence, most preferably at the contacts of the major sequences.

The unpublished report of the Belgian Mineral Exploration Project (1983) mapped areas of occurrence and anomalous concentrations of Cu, Co, Cr, Ni, and Zn, together with the geochemical data, and suggested that these elements are the potential pathfinders for the gold deposit in the area. The map indicates a close association between Cu and Zn anomalies (Figure 5.24). Due to the map's poor quality, it was impossible to plot the rest of the points on the map. However, plotted points portray an idea to understand the relation between these elements and gold occurrence. It is worth mentioning here that the gold occurrence indicated in the map comprises current findings and supplementary data from the Belgian Geological Survey work of the 1980s.

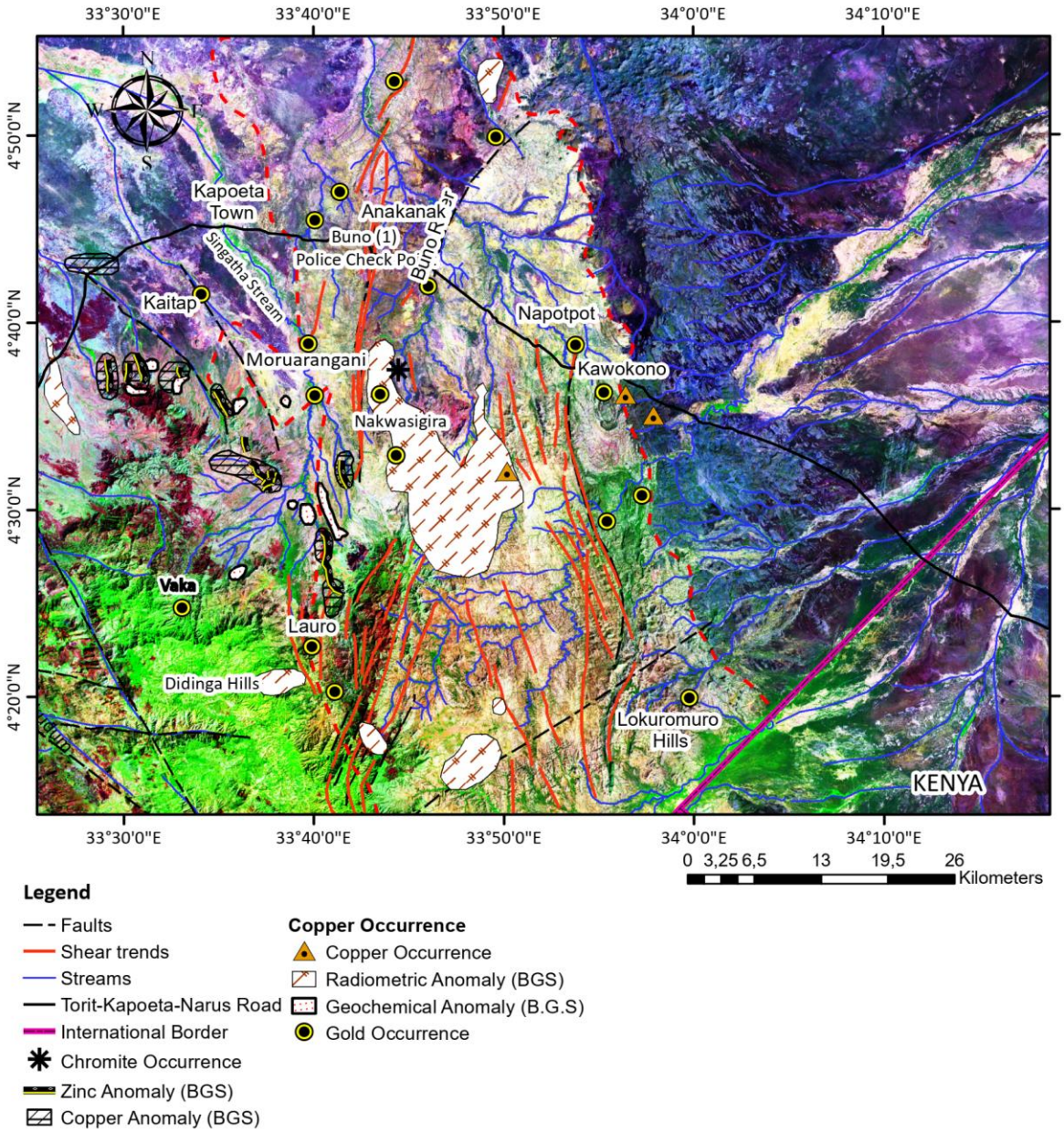

Figure 5.25: Landsat colour composite image of Kapoeta showing the occurrence and anomalies of Cu, Zn, and Cr elements.

Previous studies found 12 localities of gold occurrences associated with different lithologies in the Kapoeta area. The most important gold deposit was the Kawokono, about 45 km east of Kapoeta town and 3 km south of the Lobur police post. The gold occurs in both eluvial and alluvial concentrations. The primary source is hosted in graphitic gneisses that have been invaded by an NW-SE trending alaskite body (Adde, 2002). A follow-up investigation in a small portion of this area yielded an average of 6.5g Au/m^3. Adde (1984) investigated the minerals, structures and rock types associated with Kapoeta gold, while Kwaku (1986) outlined that the acid/basic rocks are chemically associated with the Kapoeta. The Belgium Geological Survey, mineral exploration mission, conducted an exploration campaign between 1979-1985; extensive geochemical sampling and analysis of stream sediments were conducted. Several alluvial and eluvial gold occurrences were found. An effort to continue with the project was frustrated by the civil war of 1983 to 2005.

The unpublished reports of the Belgian Mineral Exploration Project (1983, 1985) in parts of Kapoeta found that gold is hosted in eluvium and alluvium with a concentration of 2.5 g/m^3 and 1 to 2 g/m^3 associated with talc schists (Belgium Mineral Exploration Project, 1985). In Nyangea, in an area located 25 km ENE of Kapoeta town, the eluvial gold deposit occurs in quartz veins hosted in talc and chlorite schist. Adde (1984) suggested that the concentrates of the panned gold found that the occurrence of tremolite-actinolite may be used as a pathfinder for the gold in the area. The tremolite-actinolite minerals suggest a provenance from schists and greenstone host rocks. Figure 5.24D shows heavy metals; probably magnetite and other ferromagnesian minerals and gold, after panning. This suggests that the mineralisation is lithologically linked to mafic minerals that might have originated from the basic and ultrabasic rocks south of the Buno stream. The Kawokono gold deposit is hosted in marbles and NW-SE trending graphitic gneiss intruded by alaskite (Belgium Mineral Exploration Project, 1985). One sample showed specks of gold up to 1 mm in size. It has been estimated that the deposit may host some 10,000 gr Au/tonne. They suggested further exploration around the tip of the anticline (Belgium Mineral Exploration Project, 1985). The Kawokono anticline deposit was probably introduced into the marble and the graphitic gneiss during the intrusion of the alaskite. A study focus was placed on the activity of natives.

Field data, in conjunction with satellite image interpretation of all the gold occurrence localities from the current study together with the legacy data from the Belgium Geological Survey Mission (Figure 5.24), suggests that the source of the alluvial gold deposit in Kapoeta suggests structural and lithological control associated with (i) structural features dominated by the N-S and NNW-SSE shears and folds (ii) lithological units associated with the (a) pyrite rich quartz veins, amphibolites, (b) other lithologies such as meta mafic/ultramafic assemblages, and metasedimentary rocks. The Kawokono

anticline deposits can be considered as dual mineralisation involving intrusion granitic composition lithologies (alaskite) into marble, including the marble and quartzo-feldspathic gneiss.

5.5 Geochemistry

The chemical analyses of major oxides and trace elements as representative samples for the metavolcano-sedimentary lithologies of Kapoeta performed by X-ray fluorescence spectrometry, and ICP-mass spectrometry at the Earth Lab, School of geosciences, University of the Witwatersrand (Wits) are presented below.

5.5.1 Whole-rock Geochemistry

The major oxide, rare earth, and trace element concentrations of the fourteen representative samples from the Kapoeta East and South are presented in Table 5.2 and Table 5.3. Both have been used to determine the nature, provenance, and environment of the rocks of the study area. The data was processed by using GCDkit 6.0 run in R 3.6.0 software to determine their protolith and tectonic setting. It is important to note that, although most of the major elements and other mobile elements are influenced by secondary processes, the conclusions based on mobile and immobile elements are in fair agreement.

5.5.1.1 Amphibolites

Several amphibolites were encountered in the field and are generally fine to medium grained. They comprise mainly amphibole, pyroxene, and plagioclase. The amphibolites are characterised by a moderate concentration and relatively low variation in SiO_2 (40.38–58.53 wt. % and are rich in Fe_2O_3 and CaO with Al_2O_3 (11.92-15.93 wt.%), Fe_2O_3 (7.73-13.63 wt.%), and CaO (7.95-17.96 wt.%). The MgO varies from 2.43-6.03 wt.% and total alkalis (Na_2O + K_2O) range from 1.06 to 4.51 wt.%. The TiO_2 content ranges from 0.57 to 1.75 wt.%. The trace element concentration ranges between 26.6–110.4 ppm for Ni, 15.7–49.1 ppm Co, and 38.2–471.3 ppm Cr, 51.2–99.3 ppm Zn and 2.084–151.62 ppm Cu. The Cr and V contents are between 143–360 ppm. The chondrite normalised REE patterns show enrichment in LREE for four samples relative to HREE. On Figure 5.28B there is a flat line with slight variation between LREE and HREE. Sample B-10 indicates a minor increment of HREE compared to LREE. The REE patterns of all meta-gabbros are similar, and all show a prominent positive Eu anomaly.

5.5.1.2 Metagabbro

The metagabbro is dark coarse-grained and composed of pyroxene and calcium-rich plagioclase. The major oxide content of the gabbro (sample B-14) is 47.97 wt.% SiO_2, 16.5 wt.% Al_2O_3, 11.7 wt.% Fe_2O_3, 11.82 wt.% CaO, and 5.97 wt.% MgO, 2.75 Na_2O wt.% and 0,24 K_2O wt. % (Table 5.1). The content of trace elements for the selected elements is 41.75 ppm Ni, 37.7 ppm Co, 129.7 ppm Cr, 89.7ppm Zn

and 187.6 ppm Cu. The chondrite normalised REE patterns are consistent with the rest of the samples (Figure 5.28).

5.5.1.3 Meta-Rhyolite

Meta-rhyolites are found in three areas, Napotpot, Namurunyang and south of Buno stream, occurring as outcrops. They are characterised by a dark brown to reddish brown or sometimes a buff appearance. The rock is a fine-grained texture and exhibits pronounced effects of shearing. In the hand specimen, the meta-rhyolites are composed of predominantly alkali feldspars (orthoclase and microcline), quartz and mafic minerals, which are probably biotite or amphibole minerals. The rocks show relatively high SiO_2 (83.44 – 85.25 wt.%), Fe_2O_3 (2.70–4.16 wt.%), CaO (0.07–0.24 wt.%) and variable Al_2O_3 (7.01–7.97 wt.%) with low TiO_2 (0.30-0.36). The total alkalis are very low (K_2O + Na_2O) at <1 wt.%. Trace element contents include low Ni (7.914–8.362 ppm) and low concentration of Cr (8.455–9.692 ppm). Fe_2O_3 shows an increase against MgO, while Ni, and Cr show no significant differences. An increase in SiO_2 corresponds to a decrease in Ni and Cr contents.

5.5.1.4 Schists

Schists of various types crop out in many parts of the study area, are characterised by pronounced schistosity and exhibit fine to medium-grained texture (Figure 5.14). Mineralogically, the schists are variable. The chlorite schist is green and fine- to medium-grained. It is predominantly composed of chlorite, but muscovite and quartz are also minor constituents. The quartzo-feldspathic schists are pinkish to buff, fine-grained, and have a pronounced schistosity. The schist comprises mainly quartz, alkali feldspars and muscovite. The oxide content of the schists ranges from 48.12-55.67 wt.% SiO_2, 1.83-18.85 wt.% Al_2O_3, 7.77-12.58 wt.% Fe_2O_3, 13.5- 17.39wt.% MgO, and 0.03-0.73wt.% K_2O. The trace element content is very low, 14.14 –147.2 ppm Ni, 23.4–55.7 ppm Co, 5.49–766.5 ppm Cr, and 0.078-0.264 ppm As. Sample (BUNO) is exceptional because of its higher Cr content relative to the rest of the samples suggesting an ultramafic origin. The high chromite concentration corresponds to high nickel (Ni) and cobalt (Co) content for the same sample compared to the concentrations of the other rock samples. Copper yields a lower concentration relative to Ni, Co, and Cr for sample BUNO than the rest. The chondrite normalised REE patterns are variable, and one sample shows enrichment in LREE. BUNO (green schist) displays a relatively flat normalised plot with slight enrichment in LREE, while sample BUN (chlorite schist) shows negative Ce and Eu concentrations relative to chondrite values (Figure 5.28).

Table 5.2: List of major oxides and Trace elements concentration result of the selected samples of metavolcano plutonic rocks from the Kapoeta area. South Sudan

	Samples													
Rock Types	M-Rhy	Amp	Amp	Amp	Amp	Amp	Gab	Alt-Zone	Schist	Amp	C-Schist	Amp	Amp	Calc-Sili
Elements	**AN-1**	**AN-1A**	**B-3**	**B-5**	**B-10**	**B-12**	**B-14**	**B-15**	**B-17**	**B-22**	**BUN**	**BUNO**	**BUN-2**	**NA-2**
SiO_2	85.25	52.13	53.67	58.53	40.38	47.46	47.97	83.44	48.12	44.43	54.17	55.67	49.27	50.48
Al_2O_3	7.01	15.01	15.48	15.93	11.92	14.25	16.50	7.97	18.85	13.72	1.83	4.09	13.81	19.28
Fe_2O_3	2.70	14.78	10.19	7.73	9.62	12.72	11.78	4.16	7.77	8.59	12.58	9.44	13.63	9.70
MnO	0.05	0.26	0.12	0.10	0.07	0.19	0.19	0.02	0.07	0.19	0.19	0.19	0.18	0.16
MgO	0.19	3.22	4.45	2.43	4.95	5.54	5.97	0.07	13.35	3.86	17.39	16.73	6.03	0.31
CAO	0.24	7.28	9.93	7.95	17.97	12.40	11.82	0.07	1.44	17.96	11.89	11.95	10.86	17.43
NA_2O	-0.01	2.69	3.66	3.81	1.17	1.76	2.75	0.01	2.10	1.06	0.28	0.58	2.63	0.07
K_2O	0.32	0.14	0.43	0.03	0.27	0.12	0.24	0.09	0.73	0.08	0.19	0.03	0.42	0.06
TiO_2	0.36	3.10	1.22	1.15	1.69	1.11	1.24	0.30	1.66	0.57	0.11	0.12	1.75	1.15
P_2O_5	0.07	0.54	0.23	0.41	0.26	0.09	0.18	0.06	0.28	0.05	0.07	0.02	0.22	0.20
Cr_2O_3	0.01	0.01	0.02	0.04	0.02	0.04	0.03	0.00	0.02	0.08	0.01	0.12	0.02	0.02
NiO	0.00	0.00	0.00	0.01	0.00	0.02	0.01	0.00	0.00	0.02	0.00	0.02	0.01	0.00
LOI	3.47	1.26	0.67	2.32	8.73	4.41	1.35	3.96	6.51	9.68	1.84	1.61	1.82	1.76
CIA	92	59	52	57	38	49	52	97	81	41	12	24	49	52
Total	**99.65**	**100.42**	**100.07**	**100.43**	**97.06**	**100.12**	**100.03**	**100.14**	**100.90**	**100.28**	**100.54**	**100.56**	**100.64**	**100.61**
	List of Trace Elements													
Li	20.366	11.979	9.04	11.044	39.429	16.448	12.013	18.378	26.952	23.954	1.115	5.489	4.83	2.704
P	189.251	2169.23	929.689	1570.431	1032.889	307.844	699.489	149.128	1124.132	178.594	239.351	22.412	905.224	794.184
Sc	7.051	26.959	28.82	17.681	26.985	43.714	46.888	8.253	21.476	33.284	11.296	72.121	37.092	19.368
Ti	1524.939	16289.885	6673.866	6015.675	9223.977	5709.649	6432.262	1223.792	2857.514	2481.765	592.316	643.135	9342.795	6467.148
V	70.191	235.565	232.159	148.453	286.006	299.538	347.056	89.39	186.486	292.856	58.21	149.552	297.58	286.362
Cr	9.692	2.241	88.654	184.255	38.23	238.11	129.781	8.455	37.819	471.382	5.494	766.164	79.185	27.264
Co	4.814	38.622	27.361	15.758	30.253	49.141	37.718	3.034	23.457	40.288	36.071	55.712	39.223	4.119
Ni	8.362	20.096	40.427	55.608	20.426	110.498	41.753	7.914	28.773	99.683	14.147	147.28	26.635	2.672
Cu	23.615	44.913	2.084	54.505	151.627	81.086	187.652	37.676	1.41	70.622	0.54	0.845	45.346	2.519
Zn	26.581	133.689	51.66	91.63	99.328	98.568	89.738	27.36	43.907	51.265	67.241	46.197	59.672	15.327

Ga	7.429	23.315	16.401	17.194	16.287	14.439	17.17	9.355	20.626	14.084	2.756	2.94	17.418	26.259
As	4.16	0.584	0.319	1.095	0.333	0.223	0.734	6.015	0.264	0.162	0.088	0.078	0.269	0.62
Rb	5.405	0.616	1.889	0.264	3.039	0.782	2.384	1.317	8.539	0.598	7.535	0.171	1.979	0.929
Sr	63.543	342.608	287.875	365.737	467.194	118.533	405.871	23.849	114.938	160.296	9.777	15.962	241.154	784.571
Y	32.706	42.095	23.525	27.757	18.235	18.175	21.596	20.542	16.655	13.11	16.939	3.282	31.976	17.176
Zr	12.112	4.833	28.024	24.138	1.75	3.207	3.542	56.205	2.114	2.858	7.972	2.985	13.442	19.157
Nb	8.542	9.649	4.736	6.668	2.814	1.515	0.603	15.761	1.785	0.173	0.377	0.203	3.551	3.43
Sn	2.349	4.094	2.01	2.8	1.6	0.66	0.599	9.478	1.144	1.248	0.864	0.157	1.747	1.429
Sb	1.828	0.381	0.409	1.068	0.187	0.151	0.583	4.686	0.65	0.515	0.077	0.697	0.509	1
Cs	0.274	0.026	0.039	0.021	0.143	0.021	0.067	0.102	0.11	0.035	0.328	0.01	0.041	0.028
Ba	122.528	38.069	52.174	36.199	75.84	59.485	108.921	23.091	215.458	250.684	17.299	31.319	268.033	33.829
Hf	0.213	0.167	0.817	0.577	0.126	0.175	0.31	1.35	0.079	0.207	0.248	0.159	0.452	0.52
Ta	0.158	0.59	0.295	0.461	0.169	0.113	0.044	0.116	0.135	0.018	0.037	0.019	0.21	0.201
W	0.949	0.342	0.356	0.283	0.762	0.273	0.221	0.522	0.647	0.152	0.138	0.176	0.414	0.686
Tl	0.38	0.007	0.02	0.003	0.079	0.011	0.05	0.114	0.104	0.006	0.042	-0.001	0.019	0.004
Pb	3.424	4.707	1.099	6.539	1.129	0.918	1.496	5.576	1.757	1.526	0.285	0.725	0.548	4.798
Bi	0.099	0.052	0.048	0.053	0.059	0.018	0.008	0.055	0.005	0.02	0.015	0.006	0.087	0.065
Th	6.079	4.231	2.1	3.243	0.913	0.146	0.093	32.588	1.769	0.146	0.328	0.064	0.627	0.883
U	2.307	0.797	0.835	2.061	0.58	0.062	0.045	7.31	0.224	0.385	0.164	0.025	0.256	0.309

Note: Zircons may be only partially digested by the acid dissolution method used, leading to low Zr concentrations
NDS: No Standard Data

Table 5.3: Rare Earth Elements (REE) of fourteen (14) samples from Kapoeta Area

		Samples													
Rock Types		M-Rhy	Amp	Amp	Amp	Amp	Amp	Gab	Alt-Zone	Schist	Amp	C-Schist	Amp	Amp	Calc-Sili
Elements		**AN-1**	**AN-1A**	**B-3**	**B-5**	**B-10**	**B-12**	**B-14**	**B-15**	**B-17**	**B-22**	**BUN**	**BUNO**	**BUN-2**	**NA-2**
	La	10.883	18.92	6.601	18.213	11.621	2.483	3.568	5.528	8.814	1.181	2.02	0.883	6.535	8.966
	Ce	23.731	57.419	19.876	37.903	28.656	6.336	9.855	12.73	23.962	2.907	1.714	1.476	17.153	21.012
	Pr	3.63	6.394	2.081	5.167	3.983	1.042	1.632	2.074	3.162	0.449	0.623	0.243	2.552	2.89
LREE	Nd	18.125	29.896	10.2	22.971	18.815	5.918	9.299	10.625	15.495	2.59	3.619	1.32	13.503	13.697
	Sm	4.651	7.511	3.138	5.284	4.759	2.027	3.036	3.128	4.362	1.078	1.527	0.458	4.148	3.261
	Eu	1.212	2.26	1.146	1.588	1.438	0.801	1.208	0.8	1.236	0.477	0.282	0.136	1.432	1.101
	Gd	5.216	8.174	3.865	5.493	4.96	2.729	3.74	3.563	4.909	1.633	2.293	0.634	5.17	3.445
	Tb	0.857	1.297	0.629	0.82	0.725	0.472	0.598	0.576	0.72	0.311	0.419	0.1	0.869	0.517
	Dy	5.826	8.323	4.156	5.234	4.221	3.244	4.026	3.8	4.051	2.292	2.981	0.652	5.82	3.209
HREE	Ho	1.259	1.696	0.899	1.076	0.772	0.714	0.839	0.83	0.738	0.515	0.629	0.138	1.241	0.656
	Er	3.505	4.541	2.531	2.973	1.936	1.952	2.24	2.46	1.801	1.52	1.748	0.364	3.433	1.753
	Tm	0.52	0.637	0.374	0.427	0.268	0.284	0.324	0.395	0.232	0.229	0.258	0.051	0.498	0.25
	Yb	3.227	3.743	2.452	2.667	1.696	1.864	2.007	2.726	1.336	1.519	1.602	0.326	3.122	1.572
	Lu	0.463	0.529	0.362	0.361	0.269	0.285	0.307	0.389	0.173	0.236	0.233	0.051	0.468	0.223
ΣREE		83.105	151.34	58.31	110.177	84.119	30.151	42.679	49.624	70.991	16.937	19.948	6.832	65.944	62.552
La/Nb		1.274	1.961	1.394	2.731	4.130	1.639	5.917	0.351	4.938	6.827	5.358	4.350	1.840	2.614
Ce/Pb		6.931	12.199	18.086	5.796	25.382	6.902	6.588	2.283	13.638	1.905	6.014	2.036	31.301	4.379
Nb/Lu		3.703	12.107	5.672	3.235	4.852	24.435	13.400	2.156	7.969	0.449	2.299	8.120	13.871	11.100
La/Sm		2.340	2.519	2.104	3.447	2.442	1.225	1.175	1.767	2.021	1.096	1.323	1.928	1.575	2.749
Sm/Nd		0.257	0.251	0.308	0.230	0.253	0.343	0.326	0.294	0.282	0.416	0.422	0.347	0.307	0.238
La/Yb		3.372	3.372	5.055	2.692	6.829	6.852	1.332	1.778	2.028	6.597	0.777	1.261	2.709	2.093
Gd/Yb		1.616	1.616	2.184	1.576	2.060	2.925	1.464	1.863	1.307	3.674	1.075	1.431	1.945	1.656
Ce_N/Ce^*		3.775	5.220	5.362	3.907	4.212	3.939	4.083	3.759	4.538	3.992	1.527	3.186	4.200	4.127
Eu_N/Eu^*		0.246	0.288	0.329	0.294	0.295	0.340	0.358	0.239	0.267	0.359	0.150	0.252	0.309	0.328

5.5.2 Trace Element Variations

The trace element contents show a consistent distribution with minor variations among all the samples. Ti concentration is very high in the amphibolites and moderate in the schist samples. It is probably due to Ti's strong fractionation into Fe-Ti oxides (Green 1980; Winter, 2001). Sr concentrations are relatively high in most of the samples. During magmatic processes, Sr is partitioned into mid-stage fractionates and, thus, tends to be enriched in intermediate rocks (ca. 500 ppm) relative to evolved granite (<300 ppm) or mafic igneous rocks (<450 ppm) (Salminen et al., 2005). Mielke (1979) cites levels of Sr in ultramafic, basaltic and granitic rocks as 1, 465 and 100–440 ppm, respectively. Co, Y, Sc, and C concentrations are moderate, while Zr, Nb, Cs, Sn, Ta, W, U, and Hf generally show a low content in all the samples (Table 5.2). The primitive mantle-normalised trace element plots (normalisation values after Sun and McDonough, 1989) show the amphibolites and gabbro are defined by a slightly positive slope produced by enrichment in the incompatible elements and low high field strength elements (HFSE) (Figure 5.26). The amphibolite samples display pronounced negative Zr relative to the rest of the trace elements. As is evident between the amphibolites and the meta-rhyolite samples, V, Co, and Cr decrease with increasing SiO2. These elements are highly compatible with olivine, spinel and clinopyroxene. Thus their high concentration might indicate a mantle source (Green 1980; Winter, 2001).

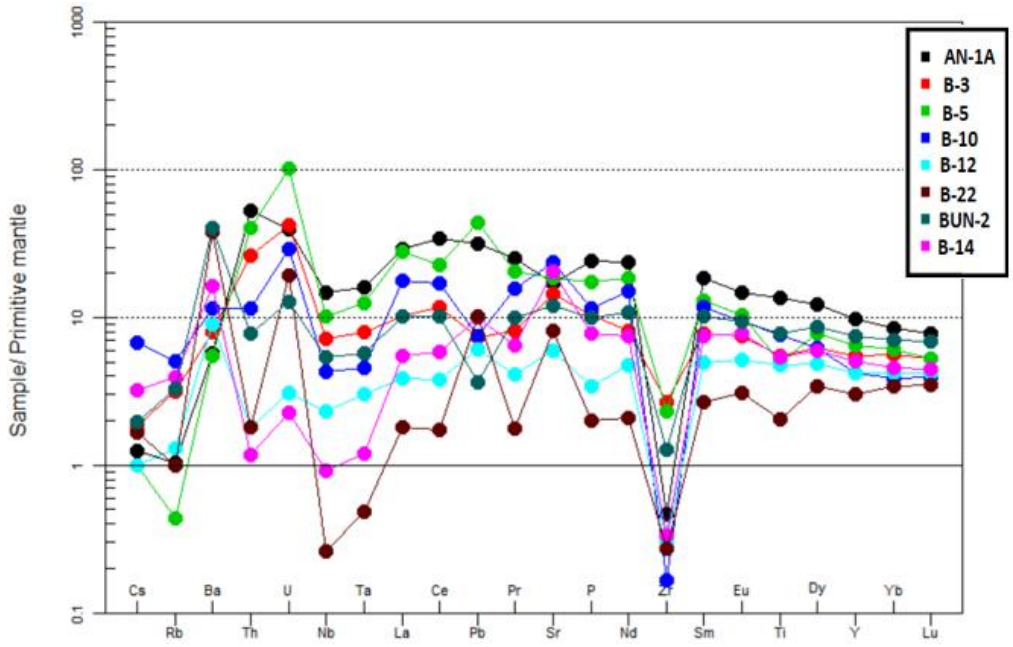

Figure 5.26: Primitive mantle-normalised trace element plots of amphibolites of Kapoeta (normalisation values after Sun and McDonough, 1989).

In the normalised primitive mantle immobile using normalising factors from McDonough and Sun (1995) multi-element plots, Rb and Nb show a low concentration in most of the samples whilst there is a distinct negative Zr pattern for all samples and tightly similar HREE values for all rock types.

The chromium, cobalt, nickel, copper, and zinc concentration of the samples examined have shown a normal pattern with respect to the individual sample. These elements are regarded as the minor elements of the crust, and the principal factors regulating the distribution of the four elements are their coordination numbers. The oxygen coordination of Cr^{3+}, Co^{2+} and Ni^{2+}, which illustrate the common valences in nature is 6-fold, whereas the coordination of Zn^{2+} may be either 4-fold or 6-fold (Lundegardh 1947). This means that the partition coefficients are low. Thus, they are concentrated in biotite, amphibole, pyroxene, and olivine where present. Normalised primitive mantle multi-element plots and normalised immobile plots display consistent negative Zr anomalies and Hf as well. The primitive mantle normalised REE is consistent with chondritic normalised REE. According to Henderson (1984), there is convincing evidence that the bulk of Earth has a relative REE distribution like that of chondritic meteorites. Thus, the primordial mantle is expected to have the same relative REE abundance as a chondritic meteorite.

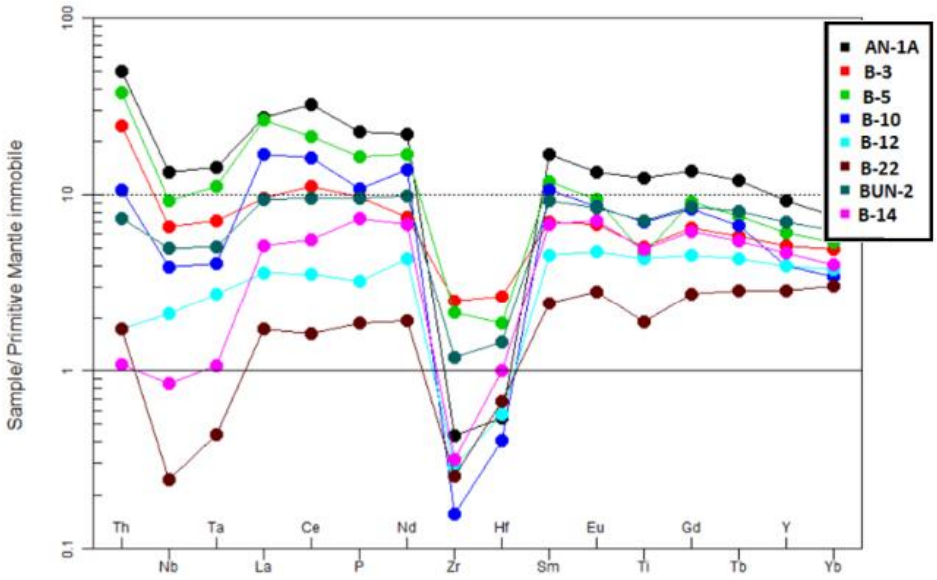

Figure 5.27: Multi-element plot of trace elements relative to primitive mantle normalised data based on McDonough and Sun 1995. AN-1A=amphibolite; B-3= amphibolite; B-5= amphibolite; B-10= amphibolite; B-12= amphibolite; B-22= amphibolite; BUN-2= amphibolite; B-14= Gabbro.

Ce behaviour is somewhat anomalous during chemical weathering as it behaves differently from other REEs (Bao and Zhao, 2008; Henderson, 1984). Cerium in an oxidising environment occurs as Ce^{4+}, resulting in highly insoluble CeO_2, whereas the other REEs maintain their 3+ ionic states and are leached by circulating water (Marsh, 1991).

Rare earth element data for amphibolites, schists and meta-rhyolites were normalised to chondrite using values from Nakamura (1974), and REE multi-element plots are presented in (Figure 5.27). The concentration of REE in the amphibolites, schists and meta-rhyolites samples is shown in Table 5.3. Chondrite normalised REE patterns of the three rock groups show smooth patterns with enrichment

in the LREE relative to the HREE in most of the samples. Sample B-22 shows relative enrichment of HREE compared to the LREE. Sample B-12, B-24 and BUNO indicate a relatively flat plot (Figure 5.27A and B).

On normalised chondrite plots, the REE patterns show LREE enrichment relative to the HREE pattern with relative negative Ce and Eu anomalies (Figure 5.28). Negative Ce anomalies are observed in chondrite-normalised rare earth element patterns from various volcanic arc suites (Bellot et al., 2018). The negative Ce anomalies are ascribed to the addition of a sedimentary component to the arc magma source (Dixon and Batiza, 1979; Elliott et al., 1997; Hole et al., 1984; Woodhead, 1989). Fe-Mn crusts and MnO clays preferentially scavenge Ce^{4+} relative to other REE^{3+} and thus have positive Ce anomalies (Amakawa, 1991; Bau et al., 2014). The Ce anomaly reflects that the wall rocks of this deposit were formed in the sedimentary environment of passive continental margin facies (Zhao, 1993). In general, Eu is a significantly multivalent element. Under the relatively oxidising condition, Eu^{3+} can exist in the solution for a long time, and under the relatively reducing environment, Eu^{3+} is reduced to Eu^{2+} and will be precipitated, whereas Ce displays an opposite condition. Therefore, the Eu-anomalies and Ce-anomalies are considered the tracers of an oxidising-reducing environment (Tang Wenchun and Zhu Huipai, 2008; Zheng Jie et al., 2011).

I. Most samples show LREE enrichment on the chondrite normalised REE patterns relative to the HREE. The enrichment of LREE compared to the HREE from La – Lu indicates the concentration of minerals in the rocks, such as plagioclases, orthopyroxene and clinopyroxenes, that are compatible with LREE.
II. Sample BUN shows a negative Ce and Eu* anomaly. The apparent negative anomaly shown by Eu* in normalised chondrite REE is when Eu is in its 2+ state, leading to Eu substituting for Ca^{2+} in plagioclase feldspar. The depleted content of Eu may indicate less fractionation of plagioclase feldspars in the melt since the feldspars favour the incorporation of Eu in their crystal structure. Because Eu^{2+} is compatible with plagioclase and potassium feldspar, europium anomalies are chiefly dependent on feldspar mineral content (Rollinson, 1993). The negative Eu anomaly is ascribed to the fractionation of feldspars (plagioclases) relative to mafic minerals.

The possibility that REE chondrite-normalised patterns might be affected by sea-floor alteration and low-grade metamorphism has been discussed by Pearce and Cann (1973), Pearce (1975), Frey (1983), Frey and Green (1974) and Frey et al. (1978). Because the rare earths are highly insoluble and immobile, rare-earth patterns often remain unchanged during metamorphism. Hence rare-earth patterns can provide information on the pre-metamorphic history of rocks (White, 2005). Plotting the

REE abundances against Zr is one of the most reliable tests to detect possible alteration and effects of metamorphism on the REE geochemistry (Yibas et al., 2003).

The chondrite normalised REE plot in Figure 5.28A generally depicts variable curves, a plot that favours the OIB and the plot that shows MORB characteristics. The anomalous redox characteristic of Eu reflects its content in Ca-rich minerals, most notably plagioclase and epidote (Anenburg et al., 2015; Bédard, 2006; Bieseler et al., 2018; Frei et al., 2004; Rudnick, 1992; Schoneveld and O'Neill, 2019). A negative Eu anomaly is typical of many continental rocks, as well as most sediments and seawater (White, 2005). Among the metamorphic minerals, garnet is very efficient in concentrating the HREE (Henderson, 1984).

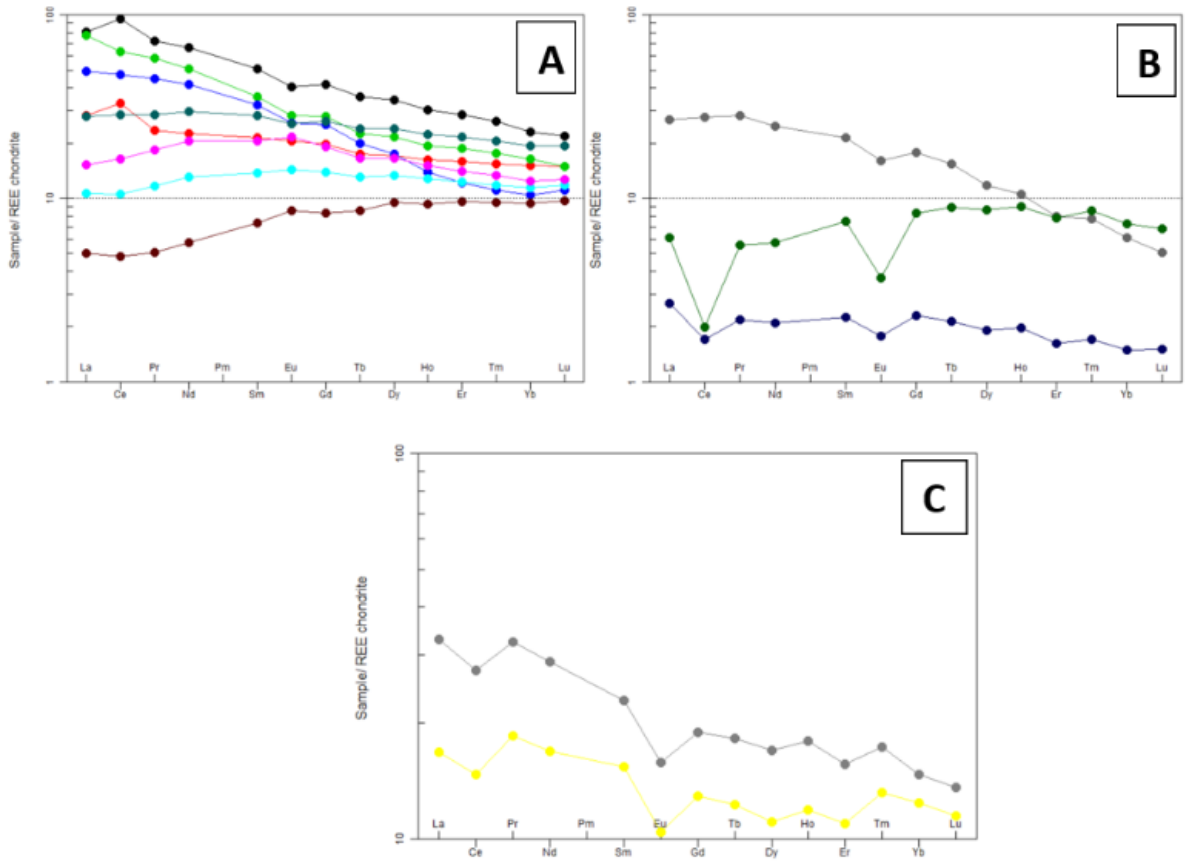

Figure 5.28: Chondrite normalised REE plots for the various rock types ***(A)*** *Chondrite normalised REE for the amphibolites* ***(B)*** *Chondrite normalised diagram for the schists.* ***(C)*** *Chondrite normalised REE metavolcanics (normalised factors after Nakamura, 1974).*

White et al. (1972) analyses of garnet and pyroxene separated from eclogite show that HREE favours garnet while pyroxene shows LREE enrichment. It has also been proven that the presence of garnet can cause a similar effect. The development of hornblende can account for the extreme enrichment of LREE compared to the HREE. It has been observed that all samples have negative Eu anomaly (0.150 – 0.359) and positive Ce anomaly (5.362 – 1.527). A positive Ce anomaly might be related to hydrogenous (seawater sourced) Fe oxyhydroxides, as Ce^{3+}, and Ce^{4+} are preferentially incorporated

into the zircon structure due to their identical charge and similar size of Zr (Zhong et al., 2019). Thus, the degree of the Ce anomaly is controlled by the oxidation state of the magma. However, the water content of the melt, temperature and melt composition also have an influence (Smythe and Brenan 2015). High oxygen fugacity will oxidise Ce^{3+} to Ce^{4+} and permits more Ce to be incorporated into the zircon crystal structure, thus resulting in greater Ce anomalies in chondrite-normalised patterns (Zhong et al., 2019).

5.5.3 Magmatic Series Determination

The geochemical data were subjected to several discrimination diagrams to define the protolith of the rocks of Greater Kapoeta. In the AFM discrimination diagram proposed by Irvin and Baragar (1971), (where A = Na_2O+K_2O, F = FeOT, M = MgO, and A + F + M = 1), the majority of the samples lie within the tholeiite series field, while two samples plot adjacent to the separation line with the calc-alkaline series field which implies possible fractionation of tholeiitic magma giving rise to the calc-alkaline affinity (Figure 5.29A).

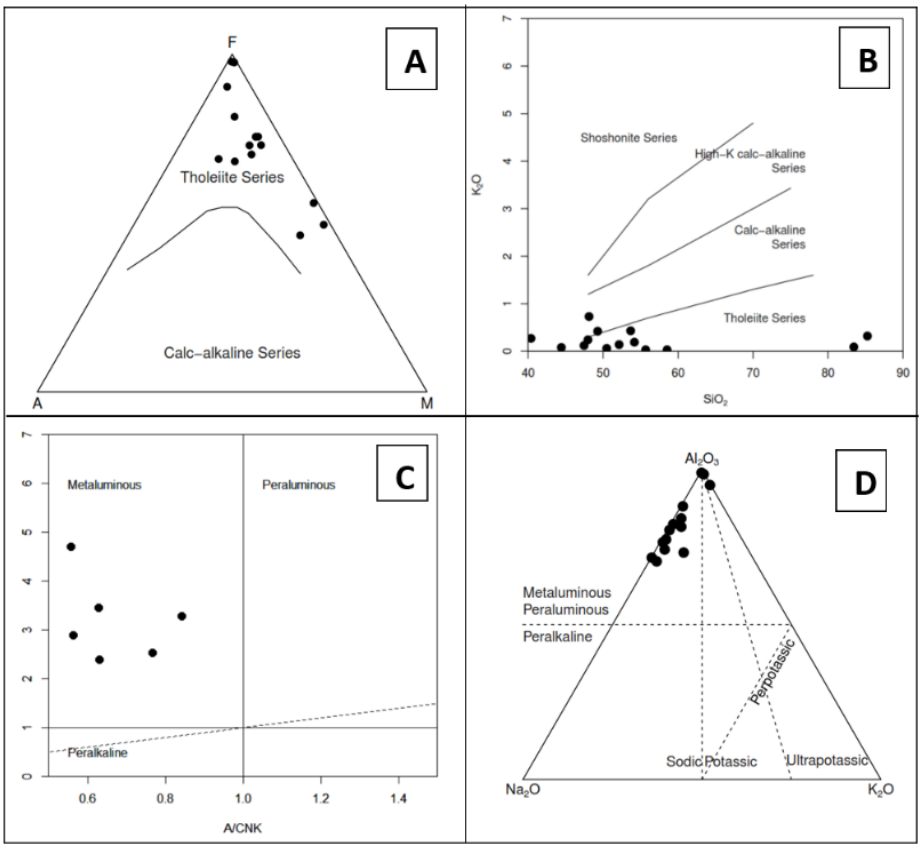

Figure 5.29: Discrimination diagrams showing the affinities of the analysed samples ***(A)*** *AFM diagram of Irvine & Baragar, 1971;* ***(B)*** *SiO_2-K_2O diagram of Peccerillo and Taylor 1979;* ***(C)*** *The A/NK versus A/CNK diagram (Shand, 1943)* ***(D)*** *Molar $Na_2O – Al_2O_3 – K_2O$ ternary diagram.*

The K_2O versus SiO_2 diagram after Peccerillo and Taylor (1976) shows similar results to the AFM diagram (Figure 5.29B), with amphibolite sample B-5 behaviour variation. On the aluminium

saturation index plot based on the molecular proportions of AI, Ca, Na and K, expressed in the form A/CNK > 1, A/CNK-1, A/CNK < 1, all the amphibolite samples are located within the metaluminous affinity field (Figure 5.29D) (after Shand 1946). On the molar Na_2O-Al_2O3-K_2O plot, all the samples fall in the metaluminus-peraluminous field. On the Ti-V geotectonic discrimination diagram (Shervais, 1982) the metavolcanics have Ti/V in the range of 20 - 50, thus, are characterised as ocean floor basalt affinities with little imprints from island arc basalts.

5.5.4 Tectonic Classification

The geochemical data (Table 5.2) of the Neoproterozoic metavolcano-sedimentary-ultramafic of the Kapoeta greenstone terrane were subjected to several discrimination diagrams to discriminate their tectonic setting. The TAS discrimination diagrams after Cox et al. (1979) (Figure 5.30A-B) indicate that the samples examined primarily have a sub-alkaline tholeiite series affinity. Similarly, the Le Bas et al. (1986) TAS classification diagram suggests a similar interpretation.

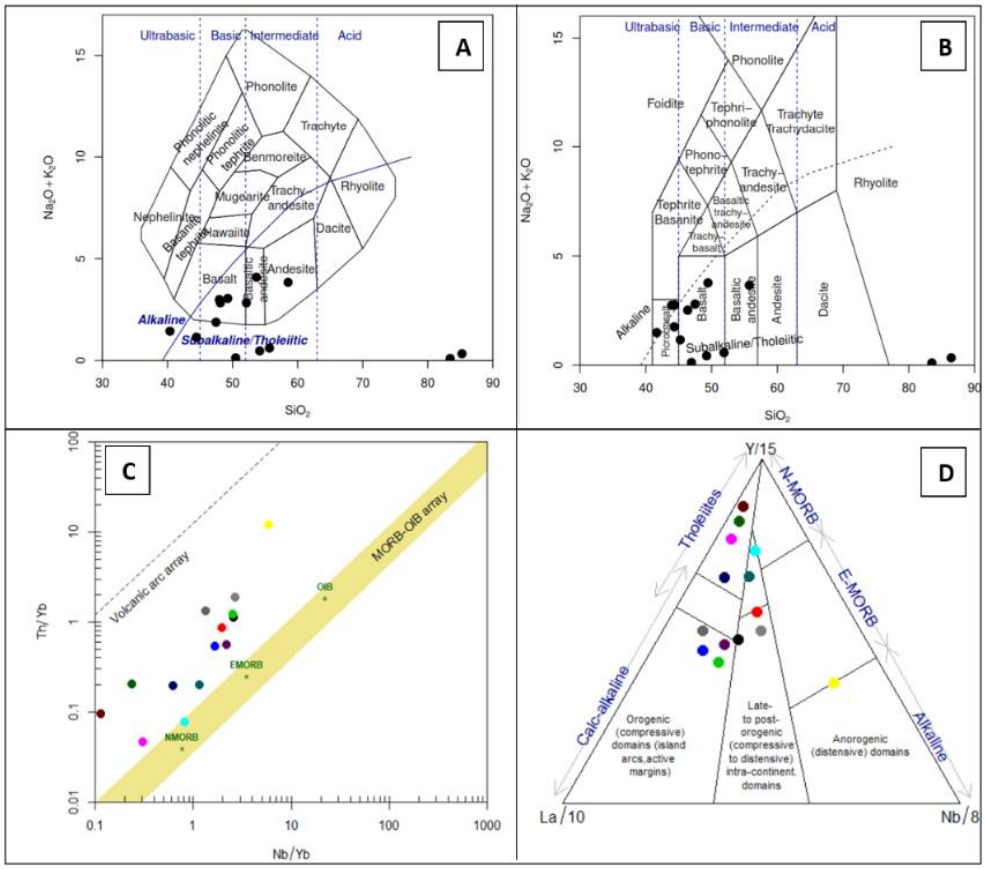

Figure 5.30: The chemical classification and nomenclature of plutonic rock using the total alkalis versus silica ***(A)*** *Total Alkali-Silica diagram (TAS) Cox et al. (1979)* ***(B)*** *Total Alkali-Silica (TAS) diagram (after Le Bas et al. 1986)* ***(C)*** *FeOt – MgO ternary plot that serves to discriminate between calc-alkaline and tholeiite series* ***(D)*** *La/10 Y/15 and Nb/8 discrimination ternary diagram (after Cabanis and Lecolle 1989).*

According to Wilson (1989), the calc-alkaline melt is typical magma in a subduction zone, while the tholeiitic series is typical of magma resulting from the first stage of island arc formation. The

discrimination diagram, Nb/Yb – Th/Yb of Pearce (2008), as shown in Figure 5.30C, indicates that the samples examined fall within a volcanic arc environment. The ternary diagram by Cabins and Lecolle (1989) suggests that the samples were formed in orogenic compressive domains, including island arc, active margins, and late to post-orogenic compressive to distance intra-continental domain (Figure 5.30D).

Chapter 6 Discussion and Conclusion

6.1 Introduction

The main purpose of this study is to demonstrate the viability of using an integrated approach involving remote sensing, in conjunction with field geological mapping and geochemical data in understanding the origin and potential sources of the alluvial gold deposit in Greater Kapoeta. Considering the data sets used during the study, it is possible to:

(i) Map areas of potential sources for gold mineralisation and their relation to the lithological units and structure in the area.

(ii) Using the geochemical data, it was possible to delineate areas of chemical variations as potential indicators for the mineralisation and their relationship to the various lithologies, discrimination of various lithological units, and understanding of the tectonic regime in the area.

6.2 Remote Sensing and Image Interpretation

Remote sensing is the science of acquiring, processing and interpreting images and related data from aircraft and satellites that record the interaction between matter and electromagnetic energy (Sabins, 1997). Remote sensing images are used for mineral exploration in two applications: (1) geological and structural mapping that localise ore deposits; (2) recognising hydrothermally altered rocks by their spectral signatures (Sabins, 1999). In the early phases of the discovery of remote-sensing technology in the 1970s, geological mapping and mineral exploration were the most typical applications (Rowan et al. 1974; Rowan et al. 1977; Goetz et al. 1983; Abrams et al. 1983). During this study, the application of satellite image datasets in mapping lithology and lineaments have proven instrumental in extracting valuable information that helped in understanding the occurrence of alluvial gold deposits and their relation to the lithology and structure in the area. The integration of Landsat (Landsat 7 ETM, Landsat 8 OLI) and Shuttle Radar Topography Mission (SRTM) digital elevation model (DEM) data successfully demonstrated the effectiveness of the method in mapping lithology and structural elements in the area.

6.2.1 Lithological Mapping

Lithological mapping using Landsat imagery and applying various techniques has been employed increasingly by several researchers (e.g., Abrams et al., 1983; Kaufmann, 1988; Abdelsalam and Stern, 1999; Sultan et al., 1986; Kusky and Ramadan, 2002; Gad, 2002; Frei and Jutz, 1989; Sabins, 1999; Bahiru and Woldai, 2016). Several techniques were utilised to perform lithological mapping using Landsat 7 ETM and 8 OLI images, as described in Chapter 4. Generally, the methods employed

produced good results related to lithology and documenting the structural elements. It has been observed that a single technique is not comprehensive in identifying all the possible lithological groups in the area. This is because of the spectral band's limitation and ability to capture electromagnetic signals from a specific spectrum range. Band 5 proved to be effective in outlining lineament features on the image. Traditionally, Band 5 is known to be excellent in discriminating vegetation cover in an area, which has been satisfactorily achieved. Several band composite images were processed for lithological discrimination.

The results from the colour composite of bands 432 in the RGB array produced a good result in mapping lithology, structure, and associated features. The combination highlights vegetation in shades of green to dark green. The dark green areas represent the dense vegetation cover seen on top of the Didinga Hills, Dongotona Mountains, and Mount Lotuke (Figure 5.2). The extrusive bodies stand out to the east and northeast corners of the composite image in a dark brown and bright colour. A band composite of natural colours made of red, green, and blue (in RGB mode) images can distinguish features related to geology, including textural characteristics of igneous and sedimentary rocks, structural features, and vegetation at a regional scale (Sabins, 1999).

Alternatively, band combinations 257 FCC in RGB were tested to discriminate lithological and major structural features (Figure 5.2). The image shows the metasedimentary supracrustal group of the Didinga Hills and Dongotona Mountains rocks in blue colour. Shades of purple represent the undifferentiated Basement Complex. The vegetation cover is green, and the extrusive bodies are presented in a brownish colour. The bright colour around the outcrops indicates alluvial fans. The fold structures are visible, e.g., the bull's eye structure in Kawokono and the folding feature south of it. A reverse of the same band, 752 FCC in RGB mode, also displays excellent results. The inclusion of Band 5 mainly exhibits a green colour, reflecting vegetation cover, corresponding to the natural colour composite result. Band 5 can also outline major structural trends and geometry. Due to sediments covering most of the area visited the satellite sensor detects few rock exposures. As such, mapping hydrothermal zones becomes challenging in the area.

The band ratios 6/7 and 6/5 effectively resolved clay zones; See the yellow mark in Figure 5.3B. However, these band ratios effectively mapped vegetation cover due to the extensive sediment cover. The rest of the bright reflections in the image could be but are not limited to vegetation. The band ratio of 6/5 is helpful to map ferrous minerals due to the high reflectance of these minerals in this ratio (Gupta, 2003). The combination of band ratios (7/5: 6/4: 4/2) in RGB mode displays the extrusive bodies' dark blue and kidney red to dark blue colour (Figure 5.5). The colour composites created from the band ratios show the best result for lithological mapping units in the area. This image appears to

discriminate better major structural trends and vegetation mapping in the area. The spectral band ratio is one of the most powerful techniques for mapping the minerals of clay, alunite, and iron minerals (Sabins, 1999). This remote sensing technique is applied mainly in geological studies (Amer et al., 2010; Ali and Pour, 2014; Si Mhamdi et al., 2017; Yousif et al., 2018).

The PCA technique results for a single band (PCA 2) shows very good results in highlighting the major structures in the area (A). PCA 4 Figure 5.6B) effectively highlights areas underlain by ultramafic, mafic bodies in bright pixels marked in yellow, while sand, alluvial fan and sediment show as dark pixels. The rest of the bright reflections are unidentifiable. The PCA colour composite PC2-PC5 and PC4 in RGB mode effectively mapped the extrusive bodies, basic-ultrabasic, alluvial, and unconsolidated sediments, and vegetation (details in Figure 5.6).

Figure 5.7 shows the MNF band combination in RGB of bands MN2, MN3, and MN4, highlighting major lithological units and structural trends of major fractures and shear orientations; see details in the caption. As Green et al. (1988) modified and implemented in ENVI, the MNF transform is essentially two cascaded Principal Components transformations. Compared to the PCA technique, the MNF technique identified the older basement bodies better. Unlike the PCA technique, the MNF technique did not outline the basic-ultrabasic bodies. Noise can be removed from multispectral data by transforming to the MNF space, smoothing or eliminating the noisiest components, and retransforming to the original space (Green et al., 1988). MNF transformation corresponds to principal components when the noise variance is similar in all bands, and it diminishes to a multiple linear regression when noise is in one band only (Shawky et al., 2019). In contrast, the MNF transform minimises their noise fraction or maximises their signal-to-noise (SNR) ratio (Berman et al., 2012).

The computation of Principal Component Analysis (PCA) band ratios together with MNF has made it possible to validate the results obtained by applying a simple band composite technique. The results were remarkably effective in mapping lithological units, as shown in Figure 5.6 to Figure 5.7; based on the above findings in conjunction with field investigations, the rocks of the study area can be divided into six lithological units.

(i) Tertiary or Quaternary volcanic flood basalt sequences related to the East African Rift system.
(ii) Metavolcano-sedimentary assemblages + gneisses (Karasuk Supergroup)
(iii) Basic and ultrabasic bodies
(iv) Undifferentiated gneisses
(v) Older basement (charnockites, granulites, gneisses, granitoids etc), and

(vi) The alkaline intrusion. Furthermore, the composite band technique was practical in defining the SW flow direction of the rift-related extrusive lithologies, which appear like ripple marks on the satellite image (Figure 5.1, and Appendix I).

The Principal Component Analysis technique can efficiently discriminate lithological units and geological structures (Amer et al., 2010; Pour et al., 2016; Gasmi et al., 2016). Previous studies have suggested that the first three bands of PCA contain over 90% of the spectral information (Amer et al., 2010, 2012; Richards, 2013; Adiri et al., 2016). The combination successfully categorised and distinguished the main lithological units in the area.

Using the supervised classification technique, eight possible classes were extracted using a composite band 752 (in RGB mode, see Figure 5.8). An exception is the black tone, which categorises the syenites with probably other intrusive lithologies of similar characteristics around the Didinga Hills and Dongotona Mountains. Later field observations indicate that the black tone may highlight an area of igneous intrusions. The Umm Ruwaba Formation and the alluvial sediments are well-defined, and the results are analogous to the outcome of the other applied techniques. However, some predictions, mainly the metavolcanic rocks, appear slightly off from the expected. This might be attributed to sampling inaccuracy.

Superimposition of the drainage pattern, plotting of the current location for artisanal miners' activities, copper occurrence, copper anomaly, zinc anomaly and chromite occurrence on the Landsat image has further enabled delineation of the potential source and lithology for the gold mineralisation in the area (Figure 5.25) and the associated pathfinders.

6.2.2 Lineament Mapping

Prospectors and mining geologists have long recognised the importance of regional and local fracture patterns as controls on ore deposits (Sabins, 1999). The notion of extraction of lineaments from digital satellite images has been performed with success by several researchers (Won et al., 1997; Kim et al., 1999; Madani, 2001; Sedrettea and Rebaïb, 2016; Si Mhamdi et al., 2017), for groundwater exploration (Bruning, 2008; Alonso-Contes, 2011) and exploration for minerals (Lee et al., 2010; Rowan et al., 1991; Mars and Rowan, 2006; Herbert et al., 2014; Bahiru & Woldai (2016); Mathew and Ariffin 2018; Farahbakhsh et al., 2018 and references therein). Using satellite images with field observations enables large-scale structure elements to be mapped over a wide area. Traditionally, there are three standard techniques used in lineament extraction; lineament density maps (Zakir et al., 1999), rose diagrams (Ali, 2000; Abdul Sattar et al., 2006), and intersection density of lineaments helps characterize the spatial patterns of lineaments (Kumar and Reddy, 1991). This study applied orientation analysis, combining various orientations in all directions into a single rose diagram with angles between zero, 0

and 180 degrees (Chopra, 2009). Manual lineament extraction involves visual examination, interpretation and digitising the lineament manually, and automatic lineament extraction depends on edge enhancement and filtering techniques using algorithms and computer software (Ramli et al., 2009; Hung et al., 2005; Mostafa and Bishata, 2005; Kocal et al., 2004; Argialas and Mavrantza 2004; Madani, 2001; Karnieli et al., 1996; Arlegui and Soriano 1988). The accuracy and quality of extracted lineaments, particularly the manual extraction, depends heavily on the spatial resolution of the imagery (Javhar et al., 2019) and the user's proficiency.

Figure 5.10B highlighted a large population of lineaments compared to Figure 5.10A. Four trends can be deduced from both images, N-S, NNW-SSE, NE-SW, and E-W. The NE-SW and E-W fracture systems are the predominant trends. The N-S system is weakly represented due probably to the overburden. However, in the field, they are dominant in the metavolcano-sedimentary sequence. The automatic method predicted the orientation but with higher density, which is unreliable for defining the area's structural trends. Based on the field observation and satellite image interpretation, two structural trends are of interest (i) the NW-SE trend, which is linked to the Nyangea shear zone (ii) the N-S and NNW-SSE structures, which dominate the metavolcano-sedimentary assemblages of the Karasuk Supergroup. Field evidence suggests that these structures are the potential structures controlling the area's mineralisation and tectonic development.

6.2.3 Hydrothermal Alteration Zone Identification

Hydrothermal alteration zones have been successfully mapped by many researchers using bands combination 5, 6, 7 in RGB (e.g., Kujjo, 2010; Frutuoso, 2015; Achieng et al., 2017; Omwenga, 2018; Githenya et al., 2019); however, application of this band combination produced image with similar characteristics, but it was difficult to identify potential hydrothermal alteration zones without prior knowledge of the geology of the area. A dark blue colour corresponds to the rock exposures, mainly the charnockite, granulites and granitoids. Light blue marked by boxes (Figure 6.1) are potential hydrothermal alteration zones, the red to orange are the vegetation cover in the area and green to yellow green represent basalts lava (Appendix I). Di Tommaso. (2007); Rockwell et al. (2008); Pour and Hashim. (2011) found that band ratio transformation is applicable in the qualitative detection of hydrothermal alteration minerals. As discussed above, certain band ratios, such as 4/2 and 6/7, are useful in depicting iron oxides for the former and map kaolinite, montmorillonite, and clay minerals, respectively. Ferrous mineral detection is possible using a band ratio 6/5 due to the high reflectance they have in this ratio (Gupta., 2003).

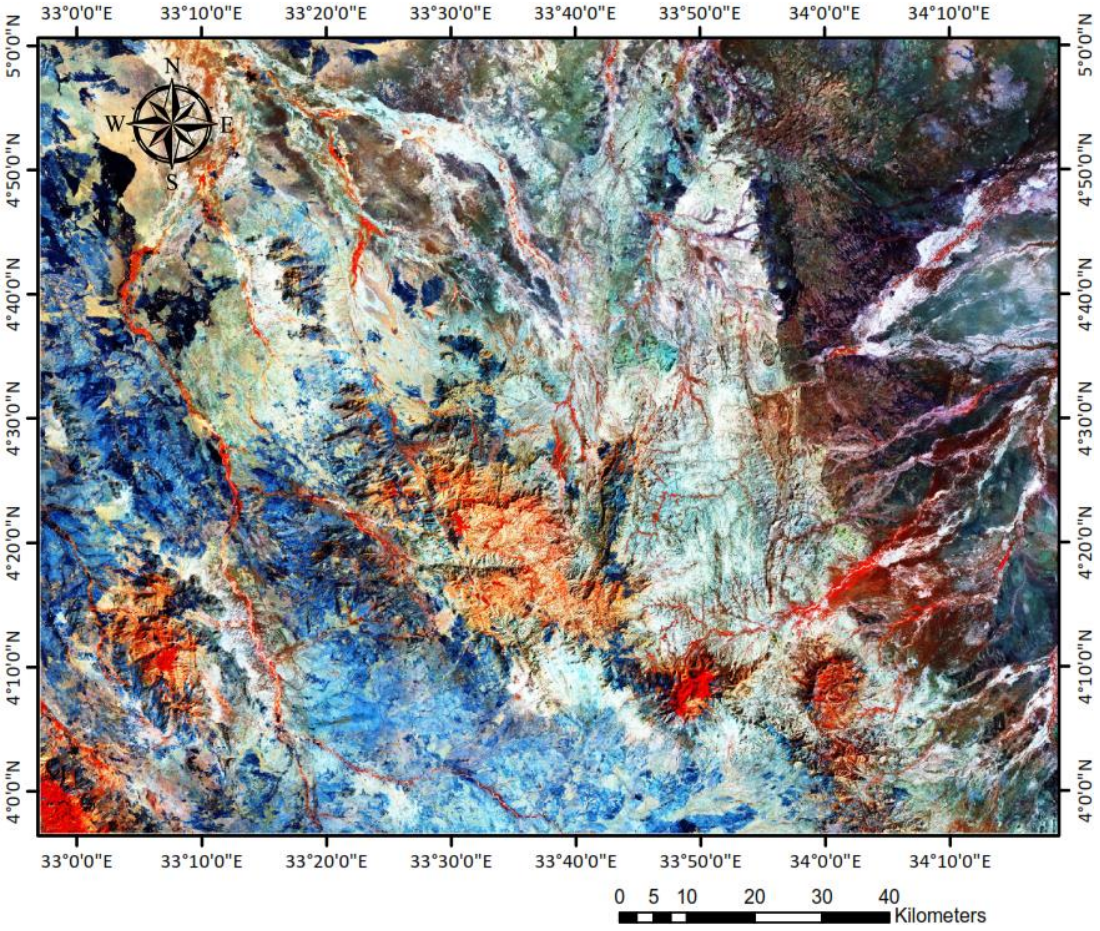

Figure 6.1: Landsat 8 OLI image band combination 457 in RGB for hydrothermal zone mapping

6.2.4 Regional Correlation and Tectonics

It has been established that the evolution of the N-S trending structure is related to E–W compression resulting from the collision and amalgamation of East and West Gondwana translated to N–S shearing due to the collision and amalgamation of the already united East and West Gondwana with the Sahara Metacraton (Westerhof et al., 2014). Compression gave rise to W- and SW-directed thrusting. Tectonic escape of the northwest corner of the proto-Congo Craton resulted in sinistral shear along the Aswa Shear Zone (Westerhof et al., 2014). Berhe (1988) established that it started with the E-W trend, which was refolded into N-S to NE-SW and later sheared and rotated into NW-SE trends. Data from different territories in the region shows that N-S to NE-SW trends are mainly found in Sudan, with the N-S and E-W trends in western Ethiopia. Furthermore, southwestern Ethiopia and north-western Kenya are generally NW-SE (Berhe, 1988), including southern South Sudan.

The NW-SE, N-S, and NNW-SSE which are identified as the dominant trends based on the field investigation and satellite imagery interpretation. The NW-SE structural orientation are pronounced in the area between the Didinga Hills and the Dongotona Mountains, a region that is dominated by the pre-Neoproterozoic lithologies (Figure 5.23). This finding agrees with the Bouguer anomaly, and the

basement topography map acquired from the gravity data (Figure 5.22). however, the NW-SE trending structures effect are not limited to the reworked basement but was observed in the field in the juvenile Neoproterozoic lithologies of Kapoeta, although the latter is mainly dominated by the N-S and NNW-SSE structural trends. These trends can be correlated to the regional trends documented in southern Ethiopia and northern Kenya. The NW-SE structural trends that are dominant in SE South Sudan, S Ethiopia, and NE Kenya have been explained because of shearing along NW trending faults (Berhe and Rothery, 1986). The NW-SE structure trends are believed to have evolved because of an oblique collision, which caused juxtaposition of the Pan-African-Mozambique terranes along a NW-SE trending strike-slip transpressive craton margin (Shackleton and Rise, 1984; Berhe, 1990) (Figure 6.3). This produced widespread NW-trending faults throughout the whole of the E and NE Africa including the Arabia region (Brown 1970; Davidson et al. 1976; Moore 1979; Vail 1983; Stern 1985; Berhe 1986; Katumwehe et al. 2015). Burke and Sengör (1986) and Berhe (1990) further postulated that the NW-trending shear zones together with minor NE-trending strike-slip shear zones represent conjugate sets of sinistral and dextral strike-slip fault systems, respectively. The N-S trend is ascribed to the Mozambique Belt event. Chronologically, the sequence of deformation based on cross-cutting relationship of folds established indicates E-W, followed by N-S (the result E-W compression) and then refolded by NW-SE trending structures (Berhe, 1990). Based on this interpretation it is logical to argue that this region had been subjected to at least three (3) phases of deformation whose fingerprints are is widely distributed throughout E and NE Africa.

Regarding the origin of the NW-SE trend structures in the study area, Katumwehe et al. (2015) in Uganda concluded that the NW-SE trending structures are potentially initiated by lateral escape due to the collision of the Arabian Nubian Shield and the Sahara Metacraton and contemporaneous final closure of the Mozambique Ocean due to docking of Azania with the Congo Craton. Attempts to correlate the Neoproterozoic NW-SE trending strike-slip shear zones of E and Northeast Africa reveal that these have occurred at different times. NW-SE trending lineaments in South Sudan are believed to overprint the older Watian and Aruan events. Berhe (1990) and Stern (1994) suggested that the development of the Aswa Shear Zone and other shear structures (e.g., Nyangere) can be linked to the collision between East and West Gondwana. Furthermore, Fritz et al. (2013) linked the evolution of the Arabian Nubian Shield to that of the Nyangere shear zone, which passes through the greater Kapoeta area, as it marks the western boundary of the Arabian Nubian Shield.

The results obtained using the above techniques in conjunction with field investigations have shown that the zones marked with shear trends are correlated with the gold occurrences which suggest potential mineralisation sites. These findings show the spatial correlation between lithology, structural lineaments, drainage pattern and the mineralisation distribution zone. Although there are some short

comings to the method such as thick vegetation cover and overburden which can limit the level of detection of the hydrothermal alteration zones by masking the outcrops which makes it difficult to detect the maximum signal, the approach employed in this study is excellent and reliable to explore mineral deposits with a high degree of efficiency.

6.3 Field Relationships and Regional Geology

The geology of study area is underlain by low to high-grade metamorphic terrane which correlate to the Karamoja Belt lithologies of NE Uganda and west Kenya. The rocks comprise Archaean metamorphosed high-grade units and associated intrusion which correlate to the basement complex of northern Uganda terrane found in the stretching from Didinga Hills westward to Dongotona mountains (Figure 5.9) and the juvenile Neoproterozoic lithologies assembled in the Arabian Nubian Shield-Mozambique Belt covering most part of the Greater Kapoeta area. They include metamorphosed rocks of igneous (intrusive and extrusive) and sedimentary protolith such as schists, amphibolites, gneisses (quartz-feldspathic, biotite), quartzites and marbles collectively classified as metavolcano-sedimentary assemblages and igneous intrusions overlain unconformably by the east Africa System basalts and associated extrusive. The metavolcano-sedimentary assemblages with the associated Precambrian intrusions combined, constitute part of the Karasuk Supergroup of Uganda-Kenya border.

6.3.1 Older Basement

The geological framework of the Didinga Hills to Dongotona mountains area to the west (Figure 5.9) is dominated by reworked pre-Neoproterozoic lithologies belonging to the west Mozambique Belt and Sahara Metacraton. This group is classified under the West Karamoja Group lithologies described in northern Uganda (Westerhof et al., 2014) which are metamorphosed to granulite facies. They are composed of granulites, charnockites, migmatites, gneisses, amphibolites and granitoids. The Didinga Hills ranges is defined as supracrustal assemblages (Vail 1988b; Petters 1991) and can be correlated to the Eastern Granulite Belt of western Mozambique Belt (see Katumwehe et al., 2015). Due to the absence of petrographic, geochemical, and chronological data, it is not possible to assign each group to the relevant units in the northern Uganda terrane.

6.3.2 Metavolcanic, Basic and Ultrabasic Rocks

In East and NE Africa metavolcanic, basic and ultrabasic rocks have been defined by several workers; to constitute the ophiolites in the eastern Egyptian desert (Bakor et al., 1976; Garson and Shalaby, 1976; Dixon, 1979; Shackleton et al., 1980; Ries et al., 1983), Ethiopia (Kazmin, 1979; DeWit and Aguma, 1977; Kazimin et al., 1978, 1979a; Berhe, 1981; Warden et al., 1982), Sudan (Hussein, 1977; Fitches et al., 1983; Abdel Rahman, 1983; Embleton et al., 1983; Vail, 1983), Kenya (Shackleton, 1979;

Vearncombe, 1983b; Price, 1984) and South Sudan (Vail, 1983; Belgian Mineral Exploration 1980). Ophiolite is thrust sheets of ancient oceanic crust and upper portion of mantle rocks that have been uplifted and exposed above sea level and often obducted on top of the continental lithosphere (Haldar, 2020). Although petrological work is yet to be done, however field observation and lithological association suggest that basic, ultrabasic lithologies in general and the associated schists belong to the ophiolite's suits which correlate to the work of Westerhof et al. 2014 in the Karamoja belt of Uganda (Table 3.2). Based on (Church, 1988; Berhe, 1988; Johnson et al. 2004; Stern et al. 2004) division, they belong to the Ingassana, Sekerr, Baragoi and Adola-Moyale complexes to the south of the Arabian Nubian Shield. They are believed to have been tectonically displaced for ~100 km due to severe shortening in South Sudan, Kenya, and SE Ethiopia (Berhe, 1988). According to Vail (1988b), the Sekerr-Karamoja area, including the Kapoeta ophiolites, are a series of metamorphosed volcanic rocks, mafic intrusion, and metasedimentary rocks.

6.3.3 Metasedimentary Sequences

As described above, metasedimentary sequences found to the west of the surveyed area indicates formation in shallow marine environments. The second occurrence of marble is to the east at Napotpot and Kawokono associated with quartzo-feldspathic gneisses, however the latter is intruded by alaskite. As described above, they have been interpreted as deposited along a passive margin to the west. An active outer transform or convergent boundaries located to the east, is defined by the Sekerr ophiolite-island-arc volcano-sedimentary assemblage (Petters 1991). For the marbles, quartzites and quartzo-feldspathic gneisses, Almond (1969) described them as extensive meta-sedimentary units that occur in association with gabbros and ultramafic rocks that correlate with their counterpart near the Uganda-Kenya border (Vail, 1985; Vail et al., 1986). Although it is known that the occurrence of marbles and quartzites is evidence of shallow-water environments, and such rocks form in the inner segment of a passive margins, given the two distinct marble occurrences in the area it is suggested that there must have been two episodes of the evaporite formation in the area or at least two shallow environment setting existed.

During the fieldwork, the observations made found that the marbles and the quartzites are closely associated with certain schists and in some instance with amphibolites. Amphibolites are widespread; in some instances, they are found sandwiched between the marbles and quartzo-feldspathic gneisses (e.g., Figure 5.11A).

6.3.4 Structural Relations and Regional Tectonics

The structural elements identified as mentioned above (N-S, NW-SE, NNW-SSE and NE-SW) suggests that during Kapoeta's geological past, the area has undergone multiple crustal deformation events. Dominant N-S, NW-SE, NNW-SSE the minor and NE-SW structural trends were identified as explained above which gives a clue about the tectonic evolution of the area. Vail (1976b) established that the development of the NW-SE structural trend is caused by tectonic escape of the proto-Conga craton related to W and SW directed thrusting which was generated due to the collision and amalgamation of east and west Gondwana during the E-W compression. The evidence of the crustal shortening is visible in the field observation metavolcano-sedimentary assemblages which are characterised by E, NE to W, SW trending steep angle of dip.

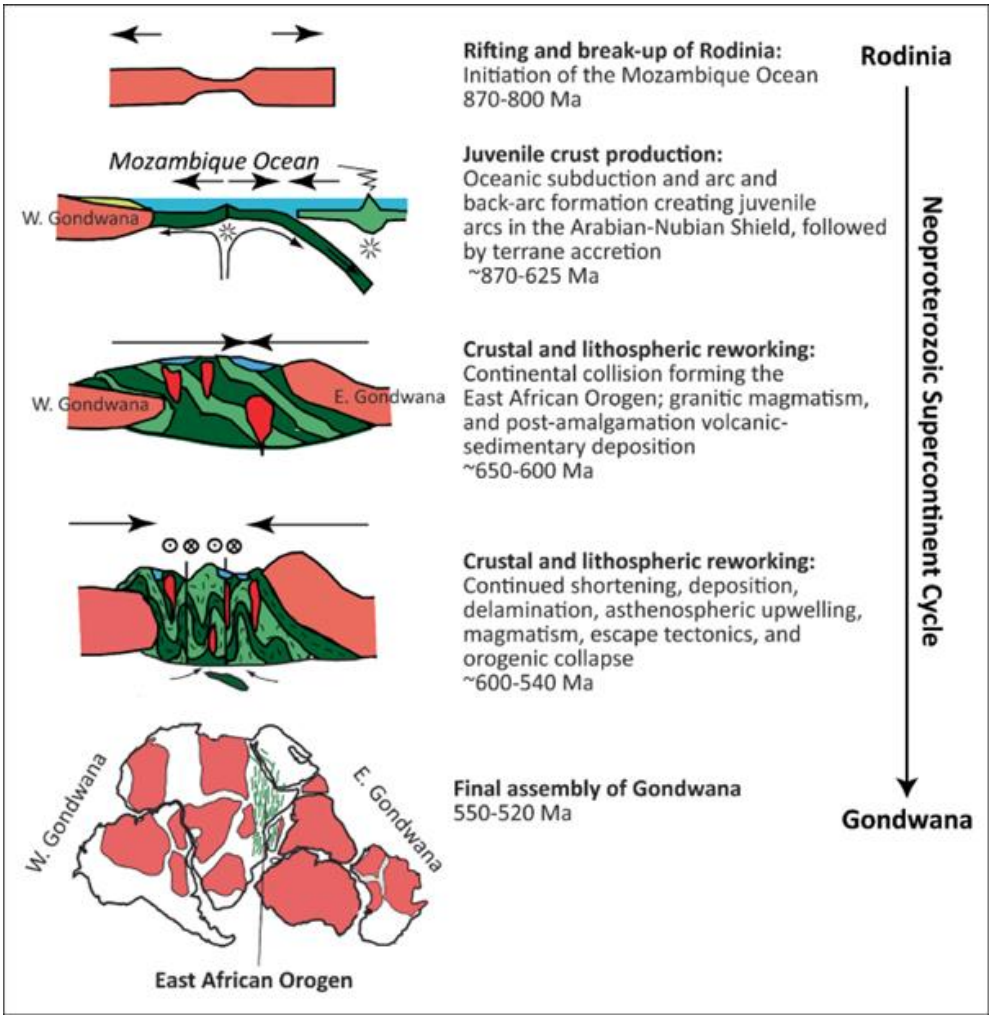

Figure 6.2: Schematic diagram suggesting the evolution of the East African Orogen (Arabian Nubian Shield) (After. Kröner and Stern, 1994).

The area between the Didinga ranges to Dongotona Mountain is affected by the NW-SE trending Chuan tectono-thermal event, which probably overprinted the older structures. Nyangere shear zone is the prominent NW-SE structural feature (Figure 3.2and Figure 5.9). Quaternary to recent unconsolidated

sediments of various thicknesses overlie these basement complexes in some areas, making it difficult to delineate the boundary of most outcrops and trace their continuity.

The tectonic evolution and the resultant Structural elements produced in the study area can be explained through the evolution of W, SW Ethiopia, and the Karamoja Belt of NE Kenya, E and NE Uganda, which are related to the East African Orogen. Researchers have agreed that the EAO evolution came into existence due to rifting and continental break-up and Neoproterozoic closure of the Mozambique Ocean involving continent-continent convergence between East and West Gondwana (Figure 6.2).

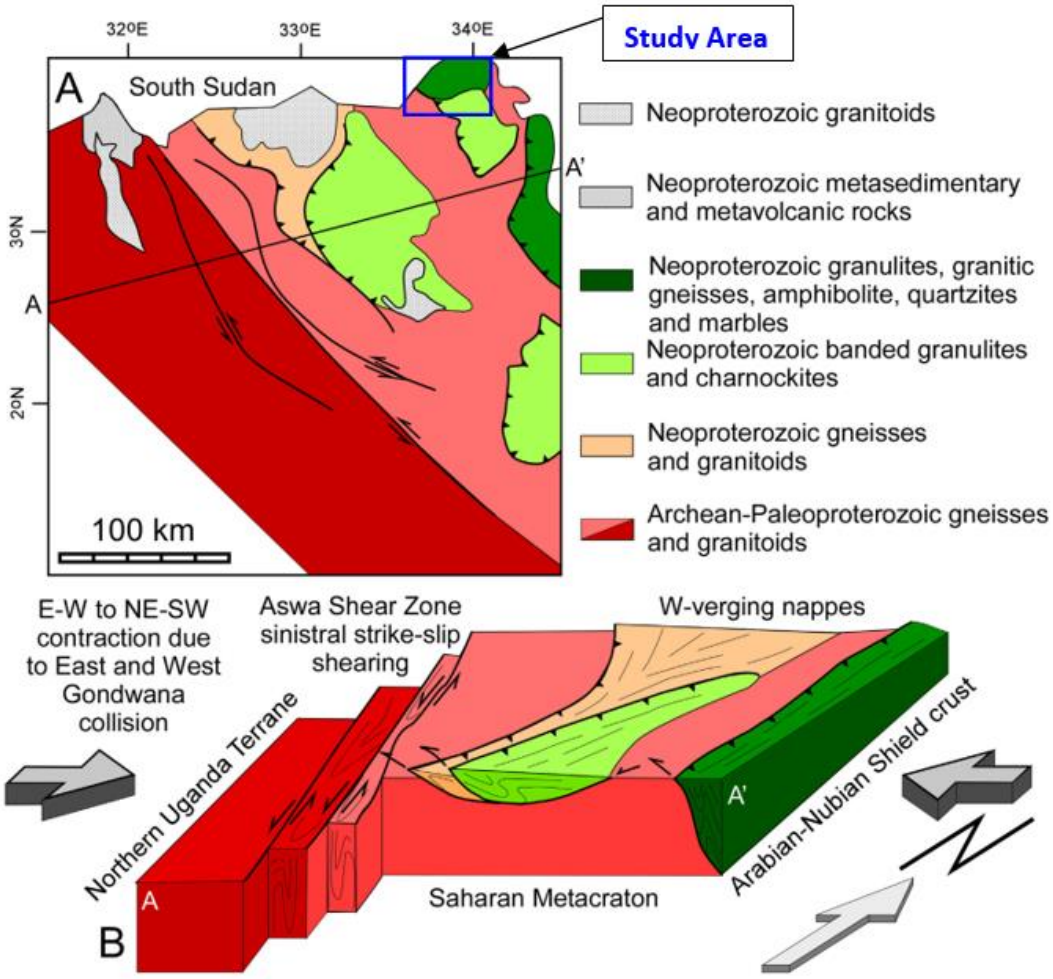

Figure 6.3: ***(A)*** *Geological map showing Aswa Shear Zone and the related structures in northeast Uganda produced from the structural analysis of airborne geophysical data and geological maps published by Westerhof et al. (2014) and Nyakecho and Hagemann (2014) showing the distribution of various lithological units.* ***(B)*** *3D illustration depicting E–W to NE–SW shortening that accompanied Neoproterozoic oblique collision between East and West Gondwana that led to the evolution of the Aswa Shear Zone as an NW-trending sinistral strike-slip shear zone and the related NW-SE (after: Katumwehe et al., 2015).*

The work of Berhe (1988) on the geologic and tectonic evolution of the Pan-African / Mozambique belt in East Africa using regional geologic, tectonic, and geochemistry proposed that the area had

undergone rifting around c.1200 Ma, subsequently followed by the evolution of intra-oceanic arc and associated marginal basins in the north and narrow basins within the sialic basement gneisses. This was followed by continent-continent with severe crustal shortening in South Sudan, Kenya, and SE Ethiopia due to oblique collision from the southeast, causing stacking of crustal blocks along NW trending faults (Figure 6.2). The findings by Westerhof et al. (2014) on the geology and tectonics of the NE Uganda Karamoja area and the research conducted by Katumwehe et al. (2015) on the tectonic origin of the Aswa Shear Zone (ASZ) agree with Berhe (1988) regarding the evolution of the western boundary of the EAO around southern Ethiopia, northern Kenya, and south-eastern South Sudan (Figure 6.3). They concluded that the evolution of the Karamoja Belt and tectonic emplacement of the rocks belonging to the Karasuk Supergroup and West Karamoja Group are related to the E-W compressional event. This was followed by the N-S compression that led to the emplacement of some of the Neoproterozoic in situ granitoids.

6.4 Geochemistry

The results of the geochemical analysis above for major oxides show that most of the samples have a wide range of composition and are generally poor in silica (SiO_2) except for samples AN-1 and B-15, which are granitic, while the rest of the samples are rich in iron (Fe_2O_3). The high concentration of SiO_2 in AN-1 may be related to silicification resulting from faulting.

6.4.1 Protolith of the Metavolcano-sedimentary Assemblages

Several classification diagrams were used to understand the protolith of the various rock types (Figure 5.29). Before processing the data, the wt. % iron (Fe) content was recalculated to fit in, e.g., AFM diagrams. The concentration of Fe obtained from the lab was reported as Fe_2O_3. To convert this concentration to wt. % of FeO, the following expression was used ($FeO=Fe_2O_3 \times 0.8998$). The total Fe was calculated using the formula ($FeO + 0.8998 \times Fe_2O_3$). When plotted using Irvine and Barager (1971), the data indicates the samples are of tholeiite series affinity, which implies crystallisation from a reduced magma showing an initial increase of Fe because of the precipitation of Mg-rich minerals. The TAS diagrams show that most of the samples are of sub-alkaline affinity.

To determine the degree of rock weathering, Nesbitt and Young (1982, 1984) suggested the chemical index of alteration (CIA), which can be obtained using the following expression:

$$CIA = \{Al_2O_3 / (Al_2O_3 + CaO^* + Na_2O + K_2O)\} \times 100 \text{ molar proportion}$$

CaO* stands for CaO in silicate minerals. The CIA values for fresh rocks are approximately 50, and higher values indicate higher degrees of weathering. Values of CIA in the studied rocks vary between 97-12. Three samples indicate a high degree of weathering AN-1, B-15 and B-17 (Table. 5.1).

The geochemistry of trace element analyses indicates that the rocks of the study area contain elements like copper, zinc, Nickel, Cobalt, and chromite, which are of economic significance in modern technology. However, these elements are also transitional elements useful in the classification of rocks. The transitional elements (Cr, Ni, Co, and V) tend to resist dispersion by secondary processes, thus strongly reflecting the chemistry of the original protolith. Their concentration in the samples analysed varies between 2.6 – 110.4 ppm for Ni, 9.6 - 766.1 ppm for Cr, 4 - 55.7 ppm for Co, and 70 – 58.2 ppm for V. The high concertation of Ni and Co are related to olivine, while Cr is an indication of the presence of spinel and clinopyroxene. Generally, the high concentration of these elements indicates a mantle source, limited fractionation, or crystal accumulation. A previous survey by the Belgian Mineral Exploration Mission, (1982), mapped areas of elements anomalies (Figure 5.25) which can be related to lithology and to some degree potential mineralisation. On the other hand, these elements serve as indicators to suggest possible mineralisation in the vicinity.

The geochemical rock classification using the TiO2-Zr diagram can be applied to ancient rocks from greenstone belts (Hallberg, 1985). Furthermore, trace elements have been utilised to characterise the magmatic type and palaeotectonic environment of the Greater Kapoeta terrane. However, discrimination diagrams involving Zr were not used because, during the analysis, it was observed that the concentration of Zr might have undergone partial digestion (dissolution) by the acid media leading to low Zr concentrations.

The Mn10-TiO_2-$10P_2O_5$ and FeO^T -MgO – Al_2O_3 ternary diagrams, according to Mullen (1983) and Pearce et al. (1977) show that the samples analysed belong to an oceanic environment: island arc tholeiite (IAT), ocean island alkaline basalts (OIA) and mid-oceanic ridge basalts (MORB) (Figure 6.4).

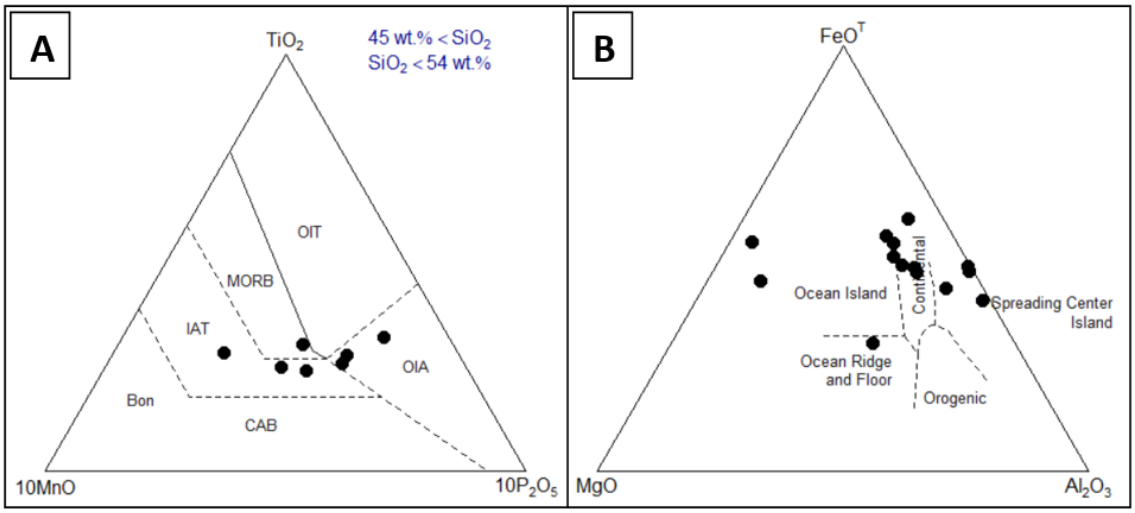

Figure 6.4: Discrimination diagram to infer the tectonic setting of the metavolcanic of Greater Kapoeta according to ***(a)*** *Mullen (1983)* ***(b)*** *Pearce et al. (1977).*

The REEs are considered among the insoluble trace elements and are relatively immobile amidst low-grade metamorphism, weathering, and hydrothermal alteration (Rollinson and Pease, 2021). The chondrite-normalised patterns of the samples' REE generally suggest low fractionation due to HREE depletion and enrichment of LREE (Figure 6.4).

Although there is an absence of petrographic analysis to validate the geochemical data, litho-geochemical and mineralogical proxies to determine, the provenance of gold mineralisation can be used to examine the indicator (pathfinder) minerals and their relation to the gold occurrence. Pathfinder minerals can indicate the occurrence of a particular mineral deposit, the nature of the alteration, or lithology (McClenaghan, 2011). During the field observations, two proxy minerals, quartz (quartz vein) and pyrite, were observed in the field during mapping (Figure 5.17). East of the Anak-Anak stream, quartz reefs were encountered. According to the Belgian Mineral Exploration Mission (1982), gold occurrence in the eluvium was found underlain by N-S trending milky quartz veins, with a grade of 10g/t gold. The legacy data from the Belgian Mineral Exploration Mission (1982) and current findings (Figure 5.25) suggest that certain indicator elements can be utilised to affirm the potentiality for gold mineralisation. This data can also be used indirectly to indicate the possible lithologies. Based on the above proceeding, Cu, Zn, Co, and Cr anomalies mapped by the Belgians are regarded as indicators associated with mafic-ultramafic (serpentinite, talc schist, and chlorite schist) bodies.

Discrimination diagram, REE, and trace element patterns combined with the lithological association described earlier under field observations indicate that the rocks of Greater Kapoeta constitute a mix of transitional environments between the continental shelf, ocean floor (MORB) and island arc settings.

6.4.2 Pyrite Enrichment

Gold is almost always associated with sulphides and sulpharsenides (e.g., Mumin et al., 1994; Oberthür et al., 1997b; Vaughan and Kyin, 2004; Morey et al., 2008; Large et al., 2009; Sung et al., 2009). It is now established that gold can be present within the crystal lattice of sulphides such as pyrite and arsenopyrite as “invisible” (refractory) gold, either as a solid solution or as sub-microscopic particles (Cabri et al., 1989; Cook and Chryssoulis, 1990).

Pyrite is the only sulphide observed in the hand specimen among the metavolcano-sedimentary (A-11; B-10; B-02) and quartz vein samples (XX and Z-1), as shown in Figure 5.17. In the hand specimen, bedrock samples B-10 indicate high pyrite concentration. The iron staining and the dark colour in the quartz veins are the product of oxidation and a sign of a high concentration of iron, which is associated in many cases with gold mineralisation worldwide. The field result requires validation from the thin section analysis to examine the pyrite minerals in the samples.

6.4.3 Pathfinder elements for the gold occurrence

The distribution of trace elements in the samples examined indicate highly variable concentrations of Cu, Co Cr, Ni and Zn in the amphibolites and schists with above-average contents relative to crustal abundance. The geochemical results of the trace elements concentration distribution show an intimate pattern between Cu, Co, Cr and Ni relative to the average concentrations (Table 6.1) in the same sample. Sample (BUNO) shows a very high concentration of 766.1 ppm for Cr, 55 ppm for Co, and 147 ppm for Ni, while Cu and As show a very low content and moderate Zn concentration. The metallurgical-grade chromite ore of (48 to 50%) Cr_2O_3 occurring as lenses in more than 0.5 wide veins extending over several tens of metres in ultramafic sequences with serpentine and talc schist host rocks has already been established (Belgian Mineral Exploration Project, 1982). The unpublished report of the Belgian Mineral Exploration Project (1983) mapped areas of occurrence and anomalous concentrations of Cu, Co, Cr, Ni, and Zn, together with the geochemical data, suggest that these elements are the potential pathfinders for the gold deposit in the area. Furthermore, the map indicates a close association between Cu and Zn anomalies (Figure 5.25). It is worth mentioning here that the gold occurrence indicated in the map comprises current findings and supplementary data from the Belgian Geological Survey work of the 1980s.

Pathfinder elements with indicator minerals combined can provide a means to assess large areas for their mineral potential by excluding potential barren areas from the areas under consideration during exploration studies (Balaram and Sawan 2022). Gold tends to co-exist with many metals, which serve as an indicator that may lead to the discovery of a gold deposit. Examples of elements used as geochemical indicators for gold include Ag, Cu, Pb, Zn, Co, Ni, As, Sb, Te, Se, and mercury. However, typical Au pathfinder elements include As, Cu, Pb, Zn, Sb, Bi, Ag, and W (Reflex Geochemistry). Traditionally, indicator minerals associated with gold mineralisation include pyrite, chalcopyrite, arsenopyrite, bismuthinite magnetite, tellurides, tetrahedrite, pyrite, sphalerite, muscovite, monazite, bastnäsite, quartz, scheelite, wolframite, cassiterite (Korshunova and Charykova, 2019; Nude et al. 2012; McClenaghan and Cabri, 2011). Bayari et al. (2019) found that Mo and Sn are also act as pathfinder elements for gold. Thus, combined indicator minerals and pathfinder elements can give a powerful and cost-effective means to assess large areas for mineral potential (Balaram and Sawan 2022).

Arsenic concentration shows patterns relative to Cu, Co, Cr, Ni and Zn. It is well established that the association between arsenic and gold Au in many gold deposits is related to (I) both being hosted in Fe sulphides (pyrite, marcasite, and arsenopyrite), (II) partly is due to the geochemistry of As, which controls the accumulation of Au (Cline, 2001; Reich et al., 2005; Xing et al., 2019). The behaviour of As in fluid-rock systems remains poorly understood due to a limited understanding of the solid solution

of As in iron sulphide minerals (Reich and Becker, 2006). The concentrations of As and Au in ore-forming fluids are normally relatively low (1–100 ppb Au, 0.10–100 ppm As) (Mikucki, 1998; James-Smith et al., 2010; Goldfarb and Groves, 2015). The upgrading model in (Figure 6.5) indicates that As (and Au) enrichment in arsenian pyrite likely results from a refinement process; low-As fluids can effectively enrich As in pyrite through ongoing hydrothermal alteration.

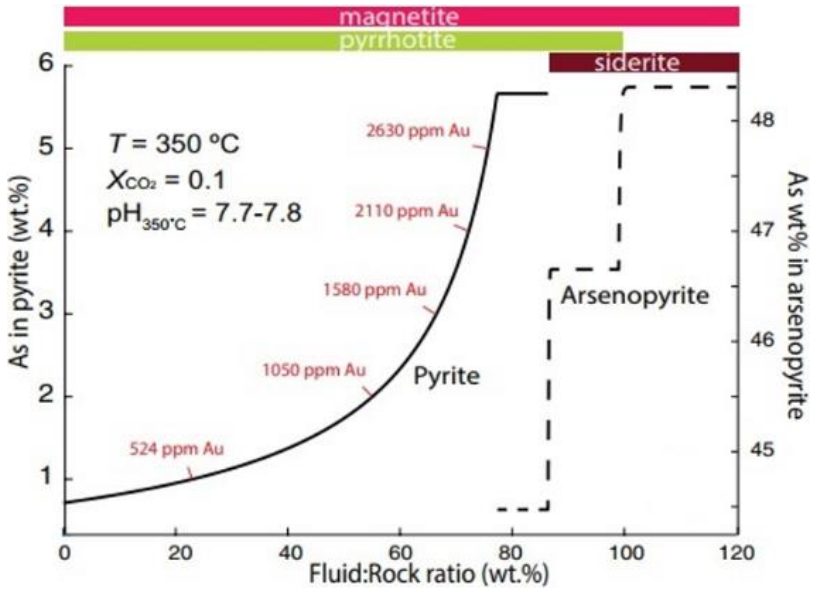

Figure 6.5: Upgrading of arsenic in pyrite and arsenopyrite. Initial fluids have 100 ppm As and ten mol % CO_2. Fluids were equilibrated with sulphur-bearing basalt before reacting with pyrite ores (initial pyrite with an As:S ratio of 0.01). The solid line represents arsenic concentrations in pyrite, and the dashed line, (As) concentrations in arsenopyrite (Xing et al. 2019). The maximum amount of Au for corresponding arsenic concentrations in pyrite is plotted based on the empirical solubility limit of Reich et al. (2005).

It has been reported that a team of scientists from the Helmholtz Centre Potsdam German Research Centre for Geosciences GFZ has now shown experimentally, for the first time, the direct relationship between gold concentration as determined by the content of arsenic in the pyrite (GFZ GeoForschungszentrum Potsdam, 2019). The As concentration in the samples varies greatly from 6.015 – to 0.078 ppm. A higher above average concentration is seen in samples B-15 and AN-1. The high concentration of As corresponds to the low content of the other proposed pathfinder elements in other samples. It shows the relationship between As and the rest of the proposed pathfinder elements. During the current study, four samples showed pyrite enrichment in hand specimens (B-10, quartz vein, marble). The thin section analysis of these samples was not possible because of the COVID-19 restrictions. However, B-10 shows a low As content relative to the concentration in B-3, B-15, AN-1B-14, AN-1A, and NA-2 samples. It is difficult to link the As and the pyrite enrichment and gold mineralisation until the thin section investigation of the pyrite-rich samples is analysed.

Canney and Wing, 1966, found cobalt to be a particularly useful element in geochemical reconnaissance surveys, especially as a pathfinder for Ni-Cu-Co deposits associated with mafic rock.

Cobalt is almost always mined as a by-product of copper and nickel (Smith, 2001; Roberts and Gunn, 2014). The average crustal abundance of Co is approximately 25 ppm, making it one of the least abundant elements (Smith, 2001). Despite this, several geological processes have locally concentrated Co to form economically viable deposits. Such deposits are hosted in diverse rocks ranging from Precambrian to Quaternary age, typically between 0.1 and 0.4 wt. % Co grade.

This study's link between Co and other elements such as Ni, Cr, and Cu indicates mafic-ultramafic systems. The relationship of these elements to gold mineralisation is governed by the factors controlling gold mineralisation in mafic and ultramafic rocks. Because of their high solubility in a wide range of silicate melts, and hydrothermal fluids, gold and associated base and precious metals (Ag, Cu, Mo, Pt, Pd) are transported into the upper crust by metal-rich, basaltic to dacitic magmas and deposited in epithermal and porphyry environments in subduction and collision zones (Hedenquist and Lowenstern, 1994; Simmons and Brown, 2006; Richards, 2011; Kamenetsky and Zelensky, 2020).

Table 6.1: Basic statistics of trace element concentrations of selected metals in analysed samples from Kapoeta.

Samples	Potential Trace Elements (ppm)					
	Cr	Co	Ni	Cu	Zn	As
B-3	88.654	27.361	40.427	2.084	51.66	0.319
B-5	184.255	15.758	55.608	54.505	91.63	1.095
B-10	38.23	30.253	20.426	151.627	99.328	0.333
B-12	238.11	49.141	110.498	81.086	98.568	0.223
B-14	129.781	37.718	41.753	187.652	89.738	0.734
B-15	8.455	3.034	7.914	37.676	27.36	6.015
B-17	37.819	23.457	28.773	1.41	43.907	0.264
B-22	471.382	40.288	99.683	70.622	51.265	0.162
AN-1	9.692	4.814	8.362	23.615	26.581	4.16
AN-1A	2.241	38.622	20.096	44.913	133.689	0.584
BUNO	766.164	55.712	147.28	0.845	46.197	0.078
BUN	5.494	36.071	14.147	0.54	67.241	0.088
BUN-2	79.185	39.223	26.635	45.346	59.672	0.269
NA-2	27.264	4.119	2.672	2.519	15.327	0.62
STDEV	219.025	16.775	44.001	57.750	33.854	1.764
Median	58.71	33.16	27.70	41.29	55.67	0.33
Min	2.241	3.034	2.672	0.54	15.327	0.078
Max	766.164	55.712	147.28	187.652	133.689	6.015
Mean	149.0519	28.96936	44.591	50.31714	64.44021	1.067429

The sample analyses show variation in the concentration of cobalt in the order of 3.03 ppm as the lowest content and 55.71 ppm as the highest. Several samples indicate elevated concentration relative to the average concentration among the samples assessed. These values are also high compared to the crustal abundance. The highest value corresponds with the high content of Cr and Ni in the same sample (e.g., BUNO). Copper compounds are very soluble, and the probability of finding them in high concentrations in residual soil is low. The concentration of Cu in the samples (B-5, B-10, B-12, B-22, and BUN-2) is greater than the average concentration known for basalt, gabbro (40–60 ppm) and

ultramafic rocks (40 ppm) (Wedepohl, 1978) and B-10, B-14, B-22 have higher than average crustal abundance as well.

Based on the above account, it is imperative to deduce that the possible pathfinders are Cu, Co, Ni, and zinc. These elements are either associated with the ultramafic and basic or the metavolcano-sedimentary sequences.

6.4.4 Tectonic Model

According to plate tectonic theory, MORBs come from the depleted mantle, whereas OIBs are generated from the enriched lower mantle, and IABs come from the depleted upper mantle (Pearce et al., 1984; Wilson, 1989). OIB generally originated from the lower mantle, according to the mantle plume hypothesis (Davies & Bunge, 2006; Morgan, 1972; White, 2010). Others suggested that OIB originates from the upper mantle (Anderson, 2000; Ballmer, van Hunen, Ito, Bianco, & Tackley, 2009; Meibom & Anderson, 2004). In fact, the mantle sources of OIB are highly heterogeneous, implying multiple origins, including enriched lower mantle, primitive mantle, ancient recycled oceanic crust (basalt + sediments), depleted asthenospheric mantle (MORB source), depleted oceanic lithosphere, recycled subcontinental lithosphere, and recycled seamounts, etc. (Castillo, 2015; Day, Pearson, Macpherson, Lowry, & Carracedo, 2009; Jackson et al., 2007; Niu & O'Hara, 2003; Niu, 2009; Zindler & Hart, 1986). Prior to the 1990s, a variety of terms was used for gold-only type hydrothermal deposits in metamorphic belts (e.g., Phillips and Powell, 1993). Gebre-Mariam et al. (1995) Groves et al. (1998). Goldfarb et al. (2001, 2005), pointed out that these deposits, whether of Precambrian or Phanerozoic age, had many features in common (details in Goldfarb & Groves 2015). These comprise (I) very late to post-peak metamorphic timing, although, in some locations, still under transpressive stresses of a subduction/active margin setting, and with a few controversial Archean deposits that some authors have argued to exhibit a prograde metamorphic overprint; (II) situated most consistently in a metamorphosed fore-arc or back-arc site (Figure 6.6); (III) formation in broad thermal equilibrium with country rocks as indicated by alteration assemblages and equivalent-temperature wall-rock assemblages, and a lack of telescoped zonation such as that shown by deposits developed under high geothermal gradients; (IV) hydrothermal addition of K, S, CO_2,H_2O, Si, and Au, with variable additions of As, B, Bi, Na, Sb, Te, and W, but low base-metal contents; and (V) supra-lithostatic H_2O–CO_2–CH_4–N_2–H_2S, low-to-moderate salinity ore-forming fluids that may have undergone phase segregation during advection and gold deposition. Based upon these similarities, the deposit group was defined by the now widely accepted term "orogenic gold deposits" (Goldfarb et al. 2001, 2005).

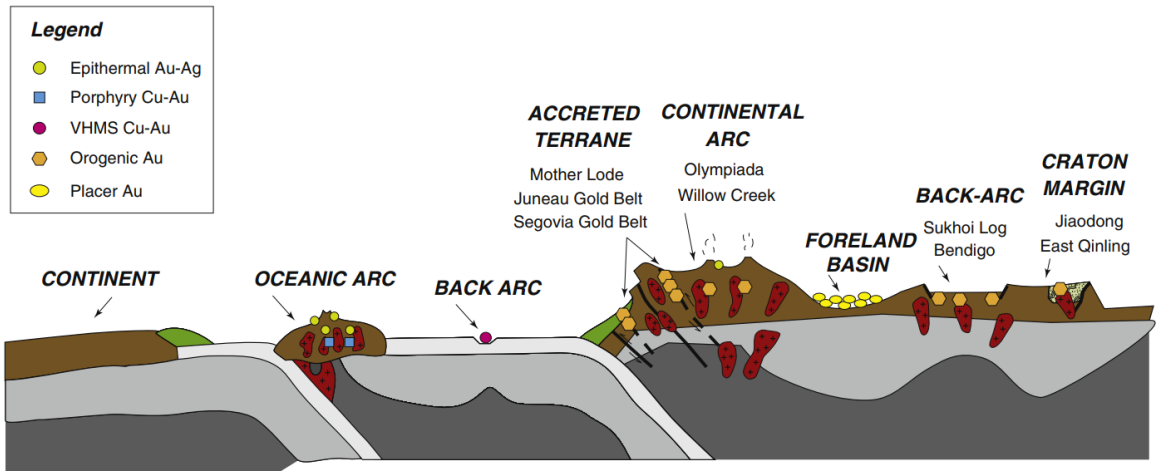

Figure 6.6: Schematic tectonic setting of orogenic and other gold deposit types. The orogenic gold deposits may be hosted in metamorphosed fore-arc and back-arc terranes of active continental margins and along the sheared margins to continental arc batholiths (Goldfarb & Groves 2015).

The tectonic model of Kapoeta is linked to the regional tectonic framework associated with the evolution of the Arabian Nubian Shield and the Mozambique Belt, involving the opening and closing of the Mozambique Ocean during the Neoproterozoic East African Orogen. The geochemical analysis is plotted on the tectonics discrimination diagram in Figure 6.4 to offer a clue to draw the possible progressive phases in the region's evolution. Shackleton (1986) suggests that the Karasuk-Cherangi area has yielded significant structural information that relates to the tectonics of the western Mozambique belt. It has been interpreted that the Karasuk metasedimentary rocks represent a miogeosynclinal environment formed along a stable continental margin to the west (Sahara Metacraton) (Petters, 1991).

The Sekerr ophiolite-island arc and volcano-sedimentary assemblages, which can be followed northward into the eastern South Sudan region of Kapoeta, define the active outer eugeosynclinal volcanic-arc belt that lies to the east (Figure 6.7). Vail (1988b) interpreted the Sekerr-Karamoja ophiolites as a sequence of andesitic meta-volcanic rocks; pillow lavas; gabbros with preserved layering; hornblende schists; and serpentinites with podiform chromite. In southeastern South Sudan, gabbro and pyroxenite fragments are tightly infolded with marbles, hornblende schists and gneissic metasedimentary rocks that probably represent a dismembered island-arc and ophiolite suite (Vail, 1988b). The nature of the rocks argues that the depositional environment of the metasedimentary sequences, which constitutes part of the Karasuk Supergroup, was deposited on a shallow passive continental margin. The deposition of the metasediments was during and in the later phase of rifting and continued during the convergent phase of the Mozambique Ocean. The mafic-ultramafic assemblages were later thrusted together with the Karasuk metasediments over the basement during the closing of the Mozambique Ocean.

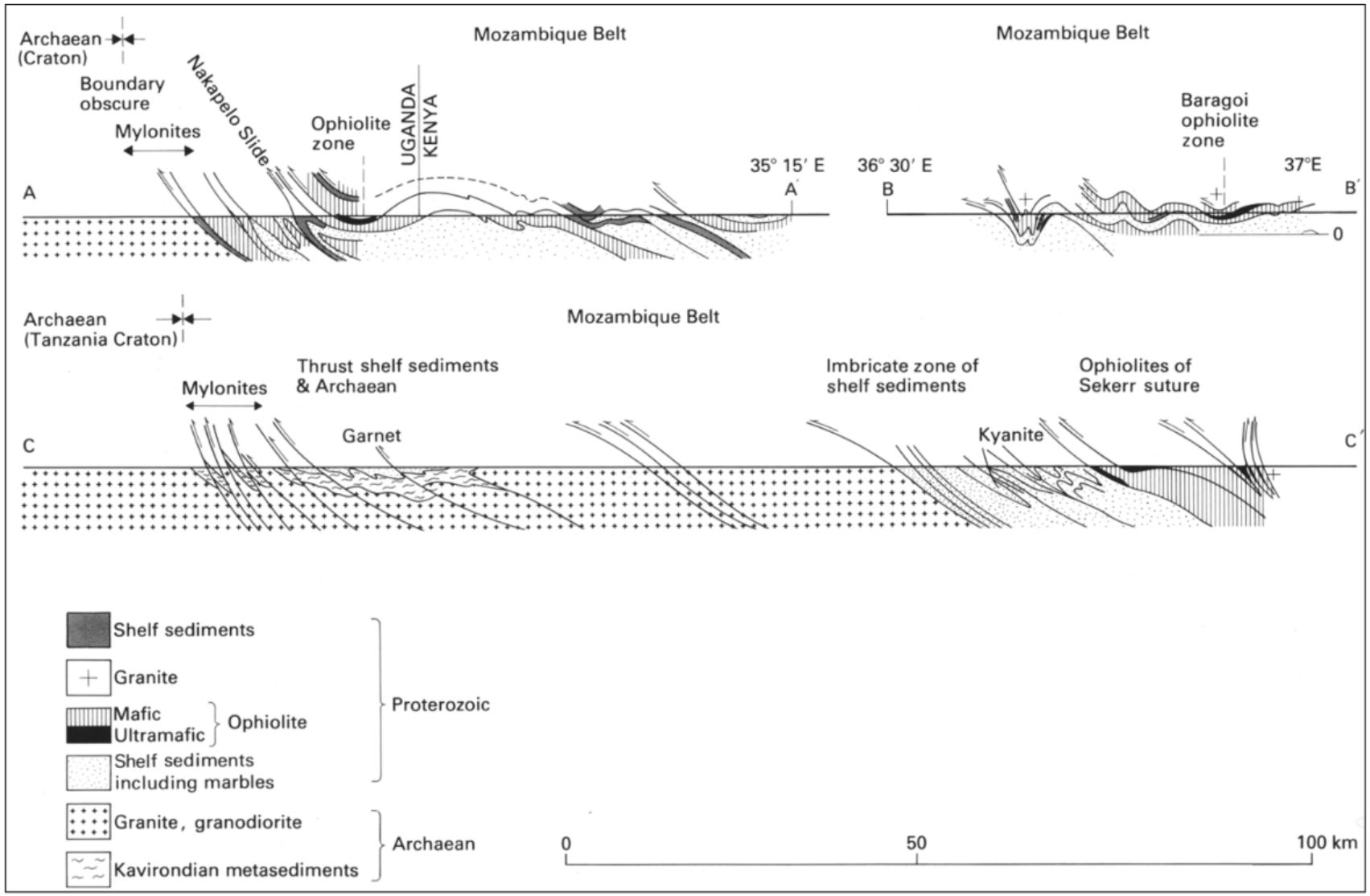

Figure 6.7: Cross-sections through the Northern Mozambique belt. (Modified from Shackleton, 1986)

6.5 Gold Mineralisation

The study aimed at determining the provenance of the alluvial gold mineralisation in the Greater Kapoeta, Didinga Hills and Dongotona Mountains. It shows that the primary source for the gold deposits is generally lithologically and structurally controlled.

Though it is not feasible to provide the genetic model for the gold mineralisation in the area at present, the lithological aspect and structural elements present allow for logical assumptions to be made, and results show that these findings agree with the regional findings of western and southern Ethiopia and the Karamoja belt of western Kenya and eastern Uganda.

6.5.1 Origin of Gold in Greater Kapoeta

As mentioned above, several artisanal working sites were encountered, and other reported sites not covered during this study suggest that there are multiple sources of primary gold in the area. Geologically, Greater is underlain by the Karasuk Supergroup rocks; a Karamoja belt segment and is considered a major gold province in South Sudan. Greenstone assemblages characterise its lithologies. Several gold deposits have been explored and mined in related terranes in East and NE Africa, e.g., Tanzania's Geita Hill Gold deposit, the Adola-Moyale belt of southern Ethiopia and NE Kenya (Sanislav et al., 2015; Tadesse, 1999; Tsige, 2006). According to the geochemical analysis, field observation, and photogeological interpretation of the satellite image of the area, it is suggested that the gold mineralisation of Kapoeta is related to quartz veins hosted in greenstone belts and metavolcano-sedimentary sequences associated with hydrothermal processes. Thus, the limited geochemical data analysed, field evidence, and the regional tectonic history seem sufficient to conclude that the origin of the alluvial deposit of the Kapoeta area is orogenic in nature (Figure 6.6 and Figure 6.7). Orogenic veins are greenstone-hosted gold or mesothermal quartz veins consisting of gold in a massive to wispy nature and multiple persistent quartz veins hosted mainly in regionally metamorphosed rocks (Drew, 2003).

Based on the geochemical analysis, data together with field mapping indicates that the rocks of Kapoeta are categorised as metasedimentary rocks of shallow marine origin and metavolcanics and plutons of oceanic and continental arcs settings. The rocks form the greenstone belt, extending southward in northeastern Uganda and north-western Kenya. Field observations found that these rocks generally form an N-S and NNW-SSE trending shear-controlled terrain. The quartz veins in the area are oriented N-S, NNW-SSE to N-S that are pyrite-bearing, whereas the rest strike NE-SW and NW-SE. These pyrite-bearing quartz veins mainly occur within the shear and faults zones.

Assessment of regional aspects for gold mineralisation in southern and southwestern Ethiopia shows that gold deposits are associated with metamorphosed greenstone belts. The work of Gherbread et

al. (1992) in Lega Dembi concluded that the shear zone contacts between the greenstone belt and the adjacent gneissic terrain are the favourable site for mineralisation. They further found that the gold mineralisation at Lega Dembi is hosted in sheared quartz veins which appear to be syn-kinematic with D_2 deformation and concurrent amphibolite-greenschist facies regional metamorphism (M_2). Dr Kenyon (reference), prospecting the area of Karasuk in the Kenyan portion of Karamoja, identified gold and silver deposits associated with copper mineralisation in quartz veins (Walsh, 1966). These veins are emplaced northeast and east of Kapcholio in western Kenya near the border with Uganda and are hosted in schistose plagioclase amphibolite or talcose schists.

The gold is associated with sulphides (galena, chalcopyrite, and pyrite). Data et al. (2009) in northeastern Uganda reported that the gold in Karamoja is hosted in lenticular bodies in quartz veins in N-S trending shear zones, closely associated with the contact between granitic gneisses and metasedimentary rocks. Arsenopyrite is associated with gold. Tsige (2006) found that the gold deposit of the Adola greenstone belt is hosted by a steeply dipping N-S trending shear zone parallel to the regional strike. The ore mineral includes pyrite, chalcopyrite, galena, and arsenopyrite.

In a greenstone belt of western Ethiopia, the Akobo Gold Exploration Project demonstrated that the gold mineralisation is hosted within the NNW-SSE trending “Surma Shear Zone” characterized by folded and sheared, Neoproterozoic mafic schist, gneisses, ultramafic bodies, metasedimentary schists, marble, and gneisses, that were intruded by late gabbros and granitoids (Jackson et al., 2019; Abebe et al., 2023). Similarly, Ghebrea et al. (1992) concluded that quartz veins, veinlets and/or stringers propagated along N-S trending mesoscale D2 ductile to brittle-ductile shear zones are gold-bearing. These veins are localised within the major shear zone, and their trends may vary. The Karamoja gold district is confined to ductile shear zones. Quartz veins are defined by subparallel emplacement to the shear zones, i.e., they represent shear veins (cf. Hodgson 1989). In all these mines, the ore-hosting structures, including quartz veins, are undeformed, i.e., emplaced during the last deformation event in the area (Nyakecho and Hagemann, 2014).

Though the reworked Archaean basement was given little attention during the current study, the work of Nyakecho and Hagemann (2014) suggests that the Karamoja gold district is hosted either in reworked Archean basement rocks and/or in the upper amphibolite–lower granulite facies rocks of the Neoproterozoic Mozambique fold belt in NE and W Uganda. This fact suggests that the Didinga Hills area is a potential site for gold mineralisation.

From a geological perspective and considering the nature of gold mineralisation in the north Mozambique, the Kawokono deposit differs from regional and local findings. The gold occurrence has been documented in the Kawokono area, and during the current field investigation, tens of artisanal

miners were observed sweeping the area for alluvial deposits (Figure 5.24D). The reason for this occurrence is uncertain, but it is interesting for a further detailed study to be conducted. The Belgium Mineral Exploration Project (BMEP) (1982) investigation revealed that the Kawokono gold deposit is associated with marble and quartzo-feldspathic gneisses intruded by the quartz-rich alaskite. Furthermore, the intrusion of the alaskite resulted in the crystallization of new minerals in the marble, such as forsterite, diopside etc. This characteristic suggests a traditional skarn-type deposit, however, the work of the Belgians found:

(i) Little contact metamorphism,

(ii) No evidence of skarn was observed, though one sample was suspected of showing some features indicating alteration, suggesting possible metasomatism.

The Kawokono deposit requires further detailed investigation to examine the marble contacts with the alaskite. Based on the facts above, the gold deposit of Kapoeta is epigenetic, considering the occurrence in late quartz veins.

6.5.2 The implication of gold mineralisation in the Didinga Hills

The landscape of the land masses is a product of interaction involving three distinct sets of variables: the nature of the underlying rocks, the tectonic regime, and the processes from external sources acting on the surfaces that are primarily controlled by climate.

The Didinga Hills constitute part of the southeastern boundary of the Sahara Metacraton. According to Vail (1988b), the ranges are metasedimentary supracrustal assemblages intruded by late post-tectonic granitoids (Fritz et al. 2013), forming an NW-SE oriented cluster of ridges rising for more than 2000 metres above sea level. On the other hand, the Karasuk Supergroup comprise metavolcano-sedimentary assemblages which appear to have undergone extensive weathering in its geological history. The net erosion rate indicates that the Didinga ranges are more resistant to weathering than the Karasuk lithologies. Thus, during the field investigation, the Didinga Hills reconnaissance survey aimed to understand the occurrence of gold in this area. However, due to insecurity caused by cattle raiding between the Toposa and Didinga tribes, it was impossible to traverse Kapoeta across to the western side of the ranges, where numerous small-scale mining activities were exploiting the alluvial deposits. Observations from the western side of Chukudum show no mention of artisanal gold mining activities in the area. However, the area appears to have the potential for mineralisation, although not necessarily for gold. The occurrence of gold deposits in the Lauro and Vaka area (Figure 5.25) might have been introduced at the contact between the Karasuk Supergroup and the Sahara Metacraton. The role played by the positive relief of the Didinga Hills, and the network of streams sourced from the hills has been important in the distribution of gold deposits in the Kapoeta.

6.5.3 Source of Metal

Numerous studies have attempted to link orogenic gold deposits with a specific source rock type (Frimmel 2008; Pitcairn 2011). Although metabasaltic lithotypes have been proposed to be essential source rocks for orogenic gold deposits, the movement of Au and associated elements (As, Sb, Se, and Hg) from these rocks during alteration and metamorphism is poorly understood (Pitcairn et al. 2015). Gold contents are relatively lower in the higher metamorphic grade rocks. Arsenic content increases proportionally with the metamorphic grade, with the metabasaltic rocks playing the role of a sink rather than a source of this element (Pitcairn et al., 2015). This fact is worth noting though the concentration factor of the As relative to the increased grade of metamorphism is not yet known. Pitcairn et al. (2015) suggest that the most suitable source rocks for fluids and metals are metasedimentary rather than metabasaltic rocks in orogenic gold deposits, as they indicate the mobility of elements enriched in this type of deposit during metamorphism. Based on the above argument, understanding the overall metal source for the orogenic gold deposit is still a matter of research.

6.5.4 Source of Fluid

The study of the fluid source was not part of the scope of this report; however, the following accounts are based on research conducted in similar environments elsewhere in the world. There is still some debate over the appropriate source of orogenic gold ore fluids and the metals they transport (Tomkins, 2013; Goldfarb and Groves, 2015; Wyman et al., 2016; Groves et al., 2020). However, it has been argued that the orogenic gold systems are formed from the crustal fluids produced during the prograde metamorphism to greenschist-amphibolite facies developed at intermediate depths (2–10 km) (Groves et al., 1998, 2003, 2020; Bierlein and Crowe, 2000; Goldfarb et al., 2001, 2005; Phillips and Evans, 2004; Dubé and Gosselin, 2007; Phillips and Powell, 2009, 2010; Tomkins, 2013; Goldfarb and Groves, 2015). Metamorphic fluids are essential in forming orogenic gold deposits (e.g., Groves et al., 1998, 2003). These crustal fluids have a distinct chemistry and were mobilised during the main episodes of orogenesis (Groves et al. 1998). It has been established that orogenic gold deposits are associated with low-salinity, near-neutral, H_2O-CO_2 ± CH_4 bearing fluids that acted as a carrier for the gold as a reduced sulphur complex (Groves et al. 1997).

6.5.5 Structural Control

Several occurrences of orogenic gold are documented in the Arabian-Nubian Shield. According to Johnson et al. (2018), the mineralisation is characterised by native gold or gold-sulphide telluride assemblages disseminated in silicified, brittle-ductile shear zones. The ore mineralogy includes pyrite ± arsenopyrite, ± chalcopyrite ± sphalerite ± tellurides in a matrix of quartz ± carbonate. The hosting

shear zones belong to the episode of transpressional deformation, strike-slip shearing, and shortening that characterised late Cryogenian-Ediacaran, tectonic escape, extension, and orogenic collapse in the Shield.

All mineral deposits are structurally controlled whether on a scale of hundreds of km or a sub-metre scale (Nex, 2017). Generally, based on field geology, the metavolcano-sedimentary assemblages of Kapoeta have a general trend of N-S with local variation to an NNW-SSE orientation with a steep dip. The N-S structural trend is believed to have originated during the late stage of tectonism, which resulted from the interchange of the original E–W grain of the northern Uganda terrain (NUT) into N–S trending features (Westerhof et al., 2014). During the progressive 630−580 Ma event, regional N–S- to NNW–SSE-oriented ductile shear zones (generally sinistral) developed, producing the dominant regional fabric (including a regional N–S-stretching lineation) and controlling the present gross distribution of gneiss groups (Westerhof et al. 2014). It is evident that Au mineralisation in most parts of East Africa, mainly south and southwestern Ethiopia, are associated with N-S and NNW-SSE shear-related quartz veins. Lithological and structural similarities supported by field data suggest a similar origin for mineralisation. The gold might have been forming during or during the late stages of deformation in the region.

Chapter 7

Conclusion

7.1 Conclusion

This study attempts to show the use of an integrated approach (remote sensing, field validation and sample collection, and geochemistry) to explore potential sources for alluvial gold deposits in the Greater Kapoeta area. According to the study's aims and objectives, the following conclusions have been deduced.

I. The result of remote sensing interpretation coupled with field validation shows that the rocks of Greater Kapoeta are composed of juvenile Neoproterozoic lithologies associated with the Karasuk Supergroup of the Mozambique belt and intruded by the alkaline lithologies of the Neogene age. The Tertiary extrusive related to the East African Rift system overlain the Karasuk Supergroup rocks mainly to the east of the study area. The Karasuk Supergroup assemblages constitute the metavolcano-sedimentary assemblages, mafic and ultramafic lithologies. The lithotypes that define the Karasuk Supergroup include gneisses, marbles, quartzites, schists, meta-basalts, meta-rhyolite, and acidic intrusions (alaskite and granites). The metasedimentary assemblages constitute rocks deposited in a shallow marine environment associated with passive margins. The metavolcanic sequences, gabbro, and the ultramafic represent part of the dismembered ophiolite suit of Sekerr-Karamoja ophiolites described by many researchers in the border region of Karamoja of eastern and Uganda and Pokot region of western Kenya.

   There is a need for detailed geological mapping of the entire area underlain by the Karasuk Supergroup lithologies.

II. According to objective number two, four structural orientations are documented using satellite imageries (Landsat 8 Oli, Landsat 7 ETM and SRTM-DEM) and field validation. The structural trends include N-S, NW-SE, NNW-SSE and NW-SE directions. The NS, NW-SE and NNW-SSE shear trends are the dominant elements documented. Foliation among the gneissic bodies and schistosity shown by the schist are common and well-developed. These Karasuk Supergroup lithologies exhibit high-angle dip.

III. The petrographic study was not possible due to COVID-19 circumstance which led to loss of the samples meant for thin sections in the preparation, however, attempt to use the reserved samples is set and the process to convene soon and the result shall be incorporated, prior to publication of this paper.

IV. Geochemical analyses show that most lithologies belong to an island arc, continental arc and mid-oceanic ridge sequences dominated by sub-alkaline tholeiite series. The concentration pattern of the indicator elements in the samples suggests that Cu, Co, Cr, Ni and Zn plus pyrite enrichment are the potential pathfinders for the gold mineralisation in the area.

More geochemical studies of the metavolcano-sedimentary assemblages and associated intrusions in the area are necessary to comprehensively understand the geological, tectonic and mineralisation potential of the different rock types in the area in relation to the regional framework.

V. Based on objective number five (5), the investigation results suggest that the gold deposits of Kapoeta are lithologically and structurally controlled. The metavolcano-sedimentary lithologies and the oxidised pyrite-rich quartz veins are the potential host for the mineralisation. The NW-SE, NNW-SSE and N-S trending shears constitute the structural control. Based on the remote sensing interpretation, field observations and geochemical data indicates that the gold mineralisation of Kapoeta is orogenic with a strong epigenetic component. However, a syngenetic origin cannot be ruled out. The host lithologies may vary from quartz veins to schists, amphibolites, quartzo-feldspathic gneisses, ultramafic and marbles.

7.2 Recommendation

Kapoeta is a vibrant district in terms of geological resources, most of which are beyond the scope of this research. Thus, the following observations are valid.

(I) Geological operations require security for the success of their objectives. The government should look for ways to work out the security issues related to cattle rustling that hinder the free movement of researchers around the area.

(II) Government should consider how to develop industrial minerals, e.g., marble which shows promising quantity and quality for high-grade cement production; the country desperately needs cement to meet its infrastructure development goals.

8. References

Abdel Rahman, E. M. 1983. The geology of mafic-ultramafic masses and adjacent rocks south of the Ingessana igneous complex, Blue Nile Province, E. Sudan. Unpublished M. Phil, thesis: Portsmouth Polytechnic, Portsmouth, gland 210 p.

Abdel-Rahman, E. M., Matheis, G., Schandelmeier, H., Karfis, M. A., Gadir, I., El Khedir, M., 1993. Evolution of the Keraf back-arc basin: Constraints on the Nubian Shield margin. In: Thorweihe, U., Schandelmeier, H. (Eds.), Geoscientific Research in NE Africa. Balkema, Amsterdam, pp. 93–98.

Abdelsalam, M. G., Gao, S. S. & Liegeois, J.-P. 2011. Upper mantle structure of the Saharan Metacraton. J. Afr. Earth Sci. 60 (5), 328–336.

Abdelsalam, M. G., Abdel-Rahman, M., El-Faki, E.-F. M., Al-Hur, B., El-Bashier, F.-R. M., Stern, R. J. & Thurmond, A. K. 2003. Neoproterozoic deformation in the northeastern part of the Saharan Metacraton, northern Sudan. Precambrian Res. 123, 203–221.

Abdelsalam, M. G., Dawoud, A.S., 1991. The Kabus ophiolitic melange, Sudan, and its bearing on the W boundary of the Nubian Shield. Journal Geological Society, London 148, 83–92.

Abdelsalam, M. G., Liegeois, J.-P. & Stern, R. J. 2002. The Sahara Metacraton. J. Afr. Earth Sci. 34, 119–136.

Abdelsalam, M. G, Stern R. J. 1993. Structural styles of late Proterozoic sutures in The Arabian-Nubian Shield: The Nakasib suture, Red Sea Hills, Sudan. J. Geol. Soc. London In press.

Abdelsalam, M. G., Stern, R.J., Schandelmeier, H., Sultan, M., 1995. Deformational history of the Keraf Zone in NE Sudan, revealed by Shuttle Imaging Radar. Journal Geology 103, 475–491.

Abdel Salam, M. G., Stern, R.J., 1996. Sutures and Shear Zones in the Arabian-Nubian Shield. Journal of African Earth Sciences, vol. 23, pp 289–310.

Abdelsalam, M. G., Stern, R.J., Copeland, P., Elfaki, E.M., Elhur, B., Ibrahim, F.M., 1998. The Neoproterozoic Keraf suture in NE Sudan: Sinistral transpression along the eastern margin of West Gondwana. Journal Geology 106, 133–148.

Abdelsalam, M. G., Stern, R.J., 1999. Mineral exploration with satellite remote sensing imagery: examples from the Neoproterozoic Arabian Shield. J. Afr. Earth Sci. 28(4a).

Abrams M, Brown D, Lepley L, Sadowski R. 1983. Remote sensing of porphyry copper deposits in Southern Arizona. Ecol. Geol., 78: 591– 604.

Achieng, J., Mutua, J., Mibei, G., Olaka, L., & Waswa, A. K. 2017. Mapping of Hydrothermal Minerals Related to Geothermal Activities Using Remote Sensing and GIS: Case Study of Paka Volcano in Kenyan Rift Valley. International Journal of Geosciences, 08(05), 711–725. https://doi.org/10.4236/ijg.2017.85039

Adde, A. E. 1984. Gold Prospection in the Southern Sudan Based on Heavy Minerals, M. Sc. Thesis, Brussels University.

Adde, A. E. 2002. Mineral and Petroleum Resources of South Sudan. Proceedings of the workshop on Natural Resources and their Conservation in South Sudan. Friedrich Ebert Stiftung.

Adiri, Z., El Harti, A., Jellouli, A., 2016. Lithological mapping using Landsat 8 OLI and Terra ASTER multispectral data in the Bas Drâa inlier, Moroccan Anti Atlas. J Appl Remote Sens 10:016005.

Afenya, P. M. 2000. Gold mineralisation models and their use ln the processing of gold ores. VI SHMMT I XVIII ENTMME - 2000 - Rio de J aneiro/Brazil.

Ahmed, S. and Amin, B. 2014. Lithological mapping and hydrothermal alteration using Landsat 8 data: a case study in Ariab mining district, red sea hills, Sudan. Intl. J. Basic and Appld. Sci., 3(3), 199-208.

Ali, A. Pour, A. 2014. Lithological mapping and hydrothermal alteration using Landsat 8 data: a case study in Ariab mining district, red sea hills, Sudan, Int. J. Basic Appl. Sci. 3 (3) (2014), doi:10.14419/ijbas. v3i3.2821.

Almond, D. C. 1962a. Explanation of the geology of Sheet 15 (Kitgum). Geol. Surv Uganda, Entebbe, Rept. 8. 55p.

Almond, D. C. 1962b. Explanation of the Geology of Sheet 10 (Kaabong). Geol. Surv Uganda, Entebbe. Report. 8.

Almond, D. C., 1969. Structure and metamorphism of the Basement Complex of northeast Uganda. Overseas Geology and Mineral Resources, vol. 10, pp 146-163.

Almond, D. C., Ahmed, F. 1987. Ductile Shear Zones in the Northern Red Sea Hills, Sudan, and their implications for crustal collision. Geol. Journ. vol. 22, Thematic Issue, 175-184.

Alonso-Contes, C. A. 2011. Lineament mapping for groundwater exploration using remotely sensed imagery in a karst terrain: Rio Tanama and Rio de Arecibo basins in the northern karst of Puerto Rico. 79.

Amakawa, H., 1991. Isotopic compositions of Ce, Nd and Sr in ferromanganese nodules from the Pacific and Atlantic Oceans, the Baltic and Barents Seas, and the Gulf of Bothnia Earth Planet. Sci. Lett. 105, 554–565.

Amer Reda, Kusky Timothy, Ghulam Abduwasit. 2010. Lithological mapping in the Central Eastern Desert of Egypt using ASTER data. Journal of African Earth Sciences. Vol. 56, pp. 75–82

Andrew. G., Auden, J. B. and Wright, E. P. 1955. Geological map of southern Sudan. Scale 1:200001)0. Geol. Surv. Sudan, Khartoum.

Anderson, D. L., 2000. The thermal state of the upper mantle; No role for mantle plumes. Geophysical Research Letters, 27(22), 3623–3626, doi:10.1029/2000gl011533.

Anenburg, M., Katzir, Y., Rhede, D., Jöns, N. and Bach, W. 2015. Rare earth element evolution and migration in plagiogranites: a record preserved in epidote and allanite of the Troodos ophiolite. Contributions to Mineralogy and Petrology, 169, 25.

Baglow N., Elepu D., Koistinen T., Kuivasaari T., Kärkkäinen N., Lehtonen M. I., Manninen T., Marimira E., Mäkitie H., Nyakecho C., Saalmann K., Virransalo P. & Staudt M. 2012b. Explanation of the Geology of Sheets NB-36-15, NA-36-3, -4, -7 and -8 (Didinga, Kaabong, Lodwar, Aloi and Moroto) 1:250,000, Department of Geological Survey and Mines, Uganda.

Baguma, Z. M. A. 2001. Mineral potential mapping for gold in the Kaabong area, Uganda, using GIS, International Institute for Aerospace Survey and Earth Sciences Enschede, The Netherlands.

Bahiru, E. A. and Woldai, T. 2016. Integrated Geological Mapping Approach and Gold Mineralisation in Buhweju Area, Uganda. Ore Geology Reviews, 72, 777-793.

Bakor, A. R., Gas, I. G. & Neary, C. R. 1976. Jabal al Wask, northwest Saudi Arabia, an Eocambrian back-arc ophiolite. Earth and Planetary Science Letters, 30,1-9.

Bakos K. L., and Gamba P., 2011. Hierarchical hybrid decision tree fusion of multiple hyperspectral data processing chains", IEEE Transactions on Geoscience and Remote Sensing, 49(1), pp. 388-394.

Balaram. V., Sawant. S. S., 2022. Indicator Minerals, Pathfinder Elements, and Portable Analytical Instruments in Mineral Exploration Studies. Minerals 2022, 12, 394. https://doi.org/10.3390/ min12040394

Ballmer, M. D., van Hunen, J., Ito, G., Bianco, T. A., & Tackley, P. J. 2009. Intraplate volcanism with complex age-distance patterns: A case for small-scale sub lithospheric convection. Geochemistry, Geophysics, Geosystems, 10, Q06015.

Basem A. Zoheir, Peter R. Johnson, Richard J. Goldfarb, Dietrich D. Klemm. 2019. Orogenic gold in the Egyptian Eastern Desert: Widespread gold mineralisation in the late stages of Neoproterozoic orogeny. Department of Geology, Faculty of Science, Benha University, 13518 Benha, Egypt. Gondwana Research 75, 184-217.

Bao, Z. W., Zhao, Z. H., 2008. Geochemistry of Mineralisation with Exchangeable REY in the Weathering Crusts of Granitic Rocks in South China. Ore Geology Review, 33: 519–535.

Bau, M., Schmidt, K., Koschinsky, a., Hein, J., Kuhn, T., Usui, a., 2014. Discriminating between different genetic types of marine ferro-manganese crusts and nodules based on rare earth elements and yttrium. Chem. Geol. 381, 1–9. doi: 10.1016/j.chemgeo.2014.05.004.

Bauernhofer A. H., Hauzenberger C. A., Wallbrecher E., Hoinkes G., Muhongo S., Mathu E. M. 2008 Pan-African deformation in SE Kenya and NE Tanzania: geotectonic implications for the development of the north-central Mozambique Belt. African Journal of Science and Technology (AJST), Scienceand Engineering Series. 9:50–71.

Bauernhofer A. H., Hauzenberger C. A., Handler R., Wallbrecher E., Hoinkes G., Muhongo S., Mathu E. M. 2008b. 40Ar/39Ar cooling ages of Pan-African structures from the Mozambique Belt in SE Kenya: implications from the cooling history. African Journal of Science and Technology (AJST), Science and Engineering Series. 10:1–19.

Bayari, E.; Foli, G. L.; Gawu, S. K. Y. 2019. Geochemical and pathfinder elements assessment in some mineralized regolith profiles in Bole-Nangodi gold belt in north-eastern Ghana. Environ. Earth Sci. 2019, 78, 268.

Bédard, J. H. 2006. Trace element partitioning in plagioclase feldspar. Geochimica et Cosmochimica Acta, 70, 3717–3742.

Berhe, S. M. 1990. Ophiolites in Northeast and East Africa: implications for Proterozoic crustal growth. J. Geol. Soc., London 147(1), 41–57.

Belgian Mineral Exploration Mission, 1983. Progress report covering activities between April 15 and May 1983. Kapoeta., South Sudan. Democratic Republic of Sudan

Belgian Mineral Exploration Mission, 1982. Progress report covering activities between July 1981 and July 1982. Kapoeta., South Sudan. Democratic Republic of Sudan.

Belgian Mineral Exploration Mission, 1981. Progress Report covering activities between July 1980 and July 1981.

Belgian Mineral Exploration Mission, 1980. Progress report covering activities between October 1979 and May 1980. Kapoeata-Nagishot. South Sudan. Democratic Republic of Sudan.

Bellot Nina, Boyet Maud, Doucelance Régis, Bonnand Pierre, Savov Ivan, Plank Terry, Elliott Tim. 2018. Origin of negative Cerium anomalies in subduction-related volcanic samples: constraints from Ce and Nd isotopes. Chemical Geology, Elsevier, 2018, 500, pp.46-63. ff10.1016/j.chemgeo.2018.09.006ff. ffhal-02110867.

Belluco E., Camuffo M., Ferrari S., Modenese L., Silvestri S., Marani A., and Marani M., 2006. Mapping salt-marsh vegetation by multispectral and hyperspectral remote sensing", Remote Sensing of Environment, 105, pp. 54-67.

Berhe, S. M. 1981. Application of Remote Sensing in tectonic and metallogenic studies, Western Ethiopia. Unpublished M. Sc thesis. Leicester University Leicester.

Berhe, S. M. 1988. The geologic and tectonic evolution of the Pan African/Mozambique belt in East Africa. PhD thesis, Open University, Milton Keynes, UK.

Berhe, S. M. 1987. Application of Remote Sensing to tectonic and metallogenic studies in NE Africa. Symp Proc. "Remote Sensing for Exploration. Reno. Nevada 1,383-391.

Berhe, S. M., 1990. Ophiolites in Northeast and East Africa: implications for Proterozoic crustal growth. J. Geol. Soc. London 147, 41–57. https://doi.org/10.1144/ gsjgs.147.1.0041.

Berhe, S. M. & Rothery, D. A. 1986. Interactive processing of satellite images for structural and lithological mapping in northeast Africa. Geological Magazine, W, 393-403.

Berman, M., Phatak, A., Traylen, A., 2012. Some invariance properties of the minimum noise fraction transform. Chemometr. Intell. Lab. Syst. 117, 189–199.

Bertels, L., Deronde, B., Kempeneers, P., Provoost, S., Tortelboom, E., 2005. Potentials of airborne hyperspectral remote sensing for vegetation mapping of spatially heterogeneous dynamic dunes, a case study along the Belgian coastline; International Conference on Nature Resporation Practices in European Coastal Habitats, Koksijde, Belgium.

Bierlein, F. P., & Crowe, D. 2000. Phanerozoic Orogenic Lode Gold Deposits. Reviews in Economic Geology, 103 - 139.

Bingen, B., Jacobs, J., Viola, G., Henderson, I.H.C., Skara, Ø., Boyd, R., Thomas, R.J., Solli, A., Key, R.M., Daudi, E.X.F., 2009. Geochronology of the Precambrian crust in the Mozambique belt in NE Mozambique and implications for Gondwana Assembly. Precambrian Research 170, 231–255.

Bieseler, B., Diehl, A., Jöns, N., Lucassen, F. and Bach, W. 2018. Constraints on cooling of the lower ocean crust from epidote veins in the Wadi Gideah section, Oman Ophiolite. Geochemistry, Geophysics, Geosystems, 19, 4195–4217.

Boardman, J. W., and Kruse, F. A., 1994. Automated spectral analysis: a geological example using AVIRIS data, north Grapevine Mountains, Nevada: in Proceedings, ERIM Tenth Thematic Conference on Geologic Remote Sensing, Environmental Research Institute of Michigan, Ann Arbor, MI, p. I-407 - I-418.

Boyle, R. W. 1979. The geochemistry of gold and its deposits. Bull. geol. Surv. 280, 584.

Bruning, J. N. 2008. Digital processing and data compilation approach for using remotely sensed imagery to identify geological lineaments in hard-rock terrains: an application for groundwater explorations in Nicaragua. 144.

Cabanis, B. and Lecolle, M. 1989. Le diagramme La/10-Y/ 15-Nb/8: un outfil pour la discrimination de series volcaniques et la mise en evidence des processus de mélange et/ou de contamination crustale. C.R. Acad. Sci. (Ser. II) 309, 2023–2029.

Cabri L. J, Chryssoulis S. L, DeVilliers J. P. R, Laflamme J. H. G, Buseck P. R. 1989. The nature of “invisible” gold in arsenopyrite. Can Mineral 27:353–362.

Caddey, S. W., Bachman, R. L., Campbell, T. J., Reid, R. R., and Otto, R. P., 1991. The Homestake Gold Mine, An Early Protozoroic Iron-Formation-Hosted Gold Deposit, Lawrence County, South Dakota, in Geology and Resources of Gold in the United States, USGS Bulletin 1857, Washington: United States Government Printing Office

Cahen, L., Snelling, N. J., Delhal, T., Vail, J. R. 1984. The geochronology and evolution of Africa. London: Oxford Science.

Canney, F. C.; Wing, A. Lawrence. 1966. Cobalt; useful but neglected in geochemical prospecting. Economic Geology.Vol. 61. (1). 198–203. doi: https://doi.org/10.2113/gsecongeo.61.1.198.

Carranza, E. J. M.; Sadeghi, M. 2010. Predictive mapping of prospectivity and quantitative estimation of undiscovered VMS deposits in Skellefte district (Sweden). Ore. Geol. Rev., 38, 219–241.

Carranza, E. J. M. 2011. Analysis and mapping of geochemical anomalies using logratio-transformed stream sediment data with censored values. J. Geochem. Explor., 110, 167–185.

Castillo, P. R. 2015. The recycling of marine carbonates and sources of HIMU and FOZO ocean island basalts. Lithos, 216–217, 254–263.

Chen, C., 2000. Comparison of principal component analysis and minimum noise fraction transformation for reducing dimensionality of hyperspectral imagery. Journal of Geographica Research, 33, 163 – 178.

Cheng, Q. 2012. Singularity theory and methods for mapping geochemical anomalies caused by buried sources and for predicting undiscovered mineral deposits in covered areas. J. Geochem. Explor., 122, 55–70.

Chernet, T., Hart, W.K., Aronson, J. L., Walter, R. C., 1998. New age constraints on the timing of volcanism and tectonism in the northern Main Ethiopian Rift - southern Afar transition zone (Ethiopia). Journal of Volcanology and Geothermal Research 80, 267e280.

Church W. R. 1988. Ophiolites, sutures, and micro-plates of the Arabian-Nubian Shield. In The Pan-African Belt of Northeast Africa and Adjacent Areas, ed. S EIGaby, RO Greiling, pp. 289-316. Braunschweig: View eg.

Clark, L., 1967. Differential retrogressive metamorphism in granulites of the Karasuk group, Karamoga, Uganda. Geol. Mag., 104: 289-297.

Clarke, D. S.; Govett, G.J.S. 1990. Southwest Pacific epithermal gold: A rock-geochemistry perspective. J. Geochem. Explor., 35, 225–240.

Cline, J. S., 2001. Timing of gold and arsenic sulfide mineral deposition at the Getchell Carlin-type gold deposit, north-central Nevada. Econ. Geol. Bull. Soc. Econ. Geol. 96, 75–89.

Cohen, D. R. Bowell, R. J. 2014. Exploration Geochemistry. Treatise on Geochemistry 2nd Edition.

Collins, A. S.; Pisarevsky, S. A., 2005. Amalgamating eastern Gondwana: The evolution of the Circum-Indian Orogens". Earth-Science Reviews. 71 (3–4): 229–270.

Collins, A.S., 2006. Madagascar and the amalgamation of Central Gondwana. Gondwana Research 9, 3–16.

Cook, N. J, Chryssoulis, S. L. 1990. Concentration of “Invisible gold” in the common sulfides. Can Mineral 28:1–16

Cox, K. G., Bell, J. D and Pankhurst, R. J. 1979. The Interpretation of Igneous Rocks. George, Allen and Unwin, London.

Craig, J. R.; Vokes, F.M.; Solberg, T.N. 1998. Pyrite: Physical and chemical textures. Miner. Depos. 34, 82–101.

Data, G., Olarka, P. & Nyakecho, C. 2009. Gold Prospects in Uganda: Metallic Mineral Fact Sheets, Department of Geological and Mines, Uganda.

Day, J. M. D., Pearson, D. G., Macpherson, C. G., Lowry, D., & Carracedo, J.-C. 2009. Pyroxenite-rich mantle formed by recycled oceanic lithosphere: Oxygen-osmium isotope evidence from Canary Island lavas. Geology, 37, 555–558.

Davies J. H, Bunge H-P. 2006. Are splash plumes the origin of minor hotspots? Geology 34:349–52

De Waele, B., Johnson, S.P., Pisarevsky, S.A., 2008. Palaeoproterozoic to Neoproterozoic growth and evolution of the eastern Congo Craton: its role in the Rodinia puzzle. Precambrian Research 160, 127–141.

DeWit, M. J. and Abera Aguma 1977. Geology of the ultramafic and associated rocks of Tulu Dimtu, Welega. Eth. Inst. Geol. Surv_ Report No. No. 57.

Drew, L. J., 2003, Low-sulfide quartz-Au Deposit model: U.S. Geological Survey Open-File Report 03-077, available online at http:/pubs.usgs.gov/of/2003/of03-077/index.html.

Dixon, T. H., Batiza, R., 1979. Petrology and geochemistry of lavas in the northern Mariana: implications. for the origin of island arc basalts. Contrib. to Mineral. Petrol. 70, 167–181. doi:10.1007/BF00374446.

Dubé, B., and Gosselin, P. 2007. "Greenstone-hosted Quartz-Carbonate Vein Deposits," in Mineral Deposits of Canada: A Synthesis of Major Deposit-Types, District Metallogeny, the Evolution of Geological Provinces, and Exploration Methods: Geological Association of Canada, Mineral Deposits. Editor W. D. Good fellow (India: Division, Spec. Publ.), 5, 49–73.

Elepu D., Härmä P., DE Kock G. S., Koistinen T., Kuivasaari T., Kyagulanyi D., Kärkkäinen N., Lehtonen M. I., Manninen T., Mäkitie H., Saalmann K. & Staudt M. 2012. Explanation of the Geology of Sheets NA-36-11 and NA-36-12 (Mbale and Kapenguria) 1:250,000, Department of Geological Survey and Mines, Uganda.

Elliott, T., Plank, T., Zindler, A., White, W., Bourdon, B., 1997. Element transport from slab to volcanic front at the Mariana arc. J. Geophys. Res. 102, 14991. doi:10.1029/97JB00788.

Embleton, J. C. B., Hughes, D. J., Klemenic, P. M., Poole, S. and Vail, J. R. 1983. A new approach to the stratigraphy and tectonic evolution of the Red Sea Hills, Sudan Pull. Fac. Earth. Scl. King Abdul Aziz University. Jeddah, Kingdom of Saudi Arabia 6,101-12.

Farahbakhsh, E., Chandra, R., Olierook, H. K. H., et al. 2018. Computer vision-based framework for extracting geological lineaments from optical remote sensing data. ArXiv181002320 Cs.

Fitches, W. R., Graham, R. H., Hussein, I. M., Ries, A. C., Shackleton, R. M. and Price, R. C. 1983. The late Proterozoic ophiolite of Sol Hamid, NE Sudan. Prec. Res. 19, 385-411.

Frei, D., Liebscher, A., Franz, G. and Dulski, P. 2004. Trace element geochemistry of epidote minerals. Pp. 553–606 in: Epidotes. (Liebscher, A. and Franz, G., editors). Reviews in Mineralogy and Geochemistry, 56. Mineralogical Society of America and the Geochemical Society, Washington, DC,

Frei, M., Jutz, S. L., 1989. Use of Thematic Mapper data for the detection of gold bearing formations in the eastern Desert of Egypt. In: Proceedings of the 7th thematic conference on remote sensing for ore exploration geology II, pp. 1157–1172.

Frey, F. A., 1983. Rare earth element abundances in upper mantle rocks. In: Henderson, P. (Ed.), Rare Earth Element Geochemistry. Elsevier, Amsterdam, pp. 256–259.

Frey, F. A., Green, D. H., Roy, S. D., 1978. Integrated models of basalt petrogenesis: a study of quartz tholeiites to olivine melilites from southeastern Australia utilising geochemical and experimental petrological data. J. Petrol. 19, 463–513.

Frey, F. A., and Green, D.H. 1974. The mineralogy, geochemistry, and origin of lherzolite inclusions in Victorian basanites. Geochim. Cosmochim. Acta, 38, 1023-1059.

Frimmel HE. 2008. Earth's continental crustal gold endowment. Earth Planet Sci Lett. 267:45–55.

Fritz. H; M. Abdelsalam; K. A. Ali; B. Bingen; A. S. Collins; A. R. Fowler; W. Ghebreab; C.A. Hauzenberger; P. R. Johnson; T. M. Kusky, P. Macey; S. Muhongo; R. J. Stern; G. Viola; 2013., Orogen styles in the East African Orogen: A review of the Neoproterozoic to Cambrian tectonic evolution, Pages 65-106.

Fritz, H., Tenczer, V., Wallbrecher, C. A., Hauzenberger, E., Hoinkes, G., Muhongo, S., Mogessie, A., 2005. Central Tanzanian tectonic map: a step forward to decipher

Proterozoic structural events in the East African Orogen. Tectonics 24, TC6013. Hepworth, J. V., 1967. The photo-geological recognition of ancient orogenic belts in Africa. Q. JI Geol. Soc. Lond., vol. 491, pp 253-292.

Frutuoso, R. 2015. Mapping hydrothermal gold mineralisation using Landsat 8 data. A case of study in Chaves license, Portugal. 85.

Gad, S., 2002. Exploration for mineralized granites in Central Eastern Desert, Egypt, M.Sc. Thesis, Faculty of Science, Aswan, South Valley University, Egypt, 118pp.

Garson, S. & Shalaby, I. M. 1976. Precambrian-lower Palaeozoic plate tectonics and metallogenesis in the Red Sea region. Geological Association of Canada Special Paper, 14, 574-596.

Gasmi, A., Gomez, C., Zouari, H. 2016. PCA and SVM as geo-computational methods for geological mapping in the southern of Tunisia, using ASTER remote sensing data set. Arab J Geosci 9: https:// doi.org/10.1007/s12517-016-2791-1.

Ghebreab, W., Yohannes, E., Giorgis, L. W. 1992. The Lega Dembi gold mine: an example of shear zone-hosted mineralisation in the Adola greenstone belt, Southern Ethiopia. Journal of African Earth Sciences, Vol. 15, No. 3/4, pp. 489-500.

Githenya, L. K., Kariuki, P. C., & Waswa, A. K. 2019. Application of Remote Sensing in Mapping Hydrothermal Alteration Zones and Geological Structures as Areas of Economic Mineralisation in Mwitika-Makongo Area, SE Kenya. Journal of Environment and Earth Science. https://doi.org/10.7176/JEES/9-11-03

Goetz, A. F. H. Rock, B. N. Rowan, L. C. 1983. Remote Sensing for Exploration: An Overview. Economic Geology, Vol. 78, pp. 573-590.

Goldfarb R. J, Groves D. I. 2015. Orogenic gold: common or evolving fluid and metal sources through time. Lithos. 233:2–26.

Goldfarb, R. J., Baker, T., Dube', B., Groves, D. I., Hart, C. J. R., Gosselin, P., 2005. Distribution, character, and genesis of gold deposits in metamorphic terranes. In: Economic Geology 100th Anniversary, pp. 407–450.

Goldfarb, R. J., Groves, D. I., Gardoll, S., 2001. Orogenic gold and geologic time; a global synthesis. Ore Geol. Rev. 18, 1–75.

Goryachev, N.A.; Pirajno, F. 2014. Gold deposits and gold metallogeny of Far East Russia. Ore Geol. Rev. 59, 123–151.

Govett, G. J. S. .1983. Handbook of Exploration Geochemistry. Vol. 3: Rock Geochemistry in Mineral Exploration, Amsterdam: Elsevier.

Govett, G. J. S and Nichol, D. I. 1979; Lithogeochemistry in mineral exploration; Geophysics and Geochemistry in the search of Metallic ores; Geological Survey of Canada, Economic geology Report 31, p. 339-362.

Gray, J. E.; Goldfarb, R. J.; Detra, D. E.; Slaughter, K. E. 1991. Geochemistry and exploration criteria for epithermal cinnabar and stibnite vein deposits in the Kuskokwim River region, southwestern Alaska. J. Geochem. Explor., 41, 363–386.

Green, T. H. 1980. Island arc and continent-building magmatism: A review of petrogenetic models based on experimental petrology and geochemistry. Tectonophys., v.63, pp.367-385.

Green, A. A., Berman, M., Switzer, P., and Craig, M. D., 1988. A transformation for ordering multispectral data in terms of image quality with implications for noise removal: IEEE Transactions on Geoscience and Remote Sensing, v. 26, no. 1, p. 65-74.

Groves, D. I., Santosh, M., and Zhang, L. 2020. A Scale-Integrated Exploration Model for Orogenic Gold Deposits Based on a mineral System Approach. Geosci. Front. 11, 719–738. doi: 10.1016/j.gsf.2019.12.007.

Groves, D. I.; Goldfarb, R. J.; Gebre-Mariam, M.; Hagemann, S. G.; Robert, F. 1998. Orogenic gold deposits: A proposed classification in the context of their crustal distribution and relationship to other gold deposit types. Ore Geol. Rev. 13, 7–27.

Groves, D. I.; Goldfarb, R. J.; Robert, F.; Hart, C.J.R. 2003. Gold Deposits in Metamorphic Belts: Overview of Current Understanding, Outstanding problems, future research, and exploration significance. Econ. Geol. 98, 1–29.

Groves, D. I., Goldfarb, R. J., Santosh, 2015. The conjunction of factors that lead to the formation of giant gold provinces and deposits in non-arc settings. Geoscience Frontiers (in press).

Groves, D. I.; Vielreicher, R. M.; Goldfarb, R. J.; Condie, K.C. 2005. Controls on the heterogeneous distribution of mineral deposits through time. Geol. Soc. Lond. Spec. Publ. 248, 11–14.

Grunsky, E. C. 2002. R: a data analysis and statistical programming environment—an emerging tool for the geosciences. Computers & Geosciences 28, 1219–1222.

Gupta, R. P. 2003. Remote Sensing Geology. 3rd Edition, Springer-Verlag, Berlin, 655. http://dx.doi.org/10.1007/978-3-662-05283-9

Gupta, R. P. 1991. Remote Sensing Geology. Springer-Verlag.

Harlan, S. S.; Vielreicher, R. M.; Mortensen, J. M.; Bradley, D.C.; Goldfarb, R. J.; Snee, L. W.; Till, A. B. 2017. Geology and timing of ore formation in the willow creek gold district, Talkeetna mountains, Southern Alaska. Econ. Geol. 112, 1177–1204.

Hedenquist, J. W.; Lowenstern, J. B. 1994. The role of magmas in the formation of hydrothermal ore deposits. Nature 1994, 370, 519–527.

Henderson, P., 1984. Rare Earth Element Geochemistry. Elsevier, Amsterdam. 510

Herbert, S. Woldai, T. Carranza, E. J. M. van Ruitenbeek, F. J. 2014. Predictive mapping of prospectivity for orogenic gold in Uganda J. Afr. Earth Sci., 99, pp. 666-693

Hepworth, J. V. and MacDonald, R. 1966. Orogenic belts of northern Uganda basement. Nature, Lond., Vol. 210, pp 281-284

Hepworth, J. V. 1961a. The geology of the southern West Nile, Uganda, with particular reference to the charnockites and to the development of the Albert Rift. PhD. Thesis, Univ. Leeds.

Hepworth, J. V. 1961b. Okollo. Sheet 19 (Part of) & 20. (NA. 36, G II (Part of) & H. I). Geological Survey of Uganda, Entebbe.

Hepworth, J. V. 1964. Explanation of the geology of Sheets 19, 20, 28 and 29 (Southern West Nile). Report. Geol. Surv. Uganda, Entebbe 10.

Hepworth, J. V. 1967. The Photogeological recognition of ancient orogenic belts in Africa. Q. Jl. Geol. Soc. Lond., V. 491, pp 253 – 292.

Hepworth, J. V. 1972. Charnockitic granulites of some African cratons. 24th Internat. Geol. Congr. Canada, Montreal, Sect. 1, 126–134.

Hepworth, J. V. & Macdonald, R. 1966. Orogenic belts of the northern Uganda basement. Nature 210, 726–727.

Hole, M., Saunders, A., Marriner, G., Tarney, J., 1984. Subduction of Pelagic Sediments – Implications for the Origin of Ce-Anomalous Basalts From the Mariana Islands 141, 453–472. doi:10.1144/gsjgs.141.3.045.

Holmes, A., 1951. The sequence of Precambrian orogenic belts in the south and Central Africa: Rep.18thSess. Int. Geol. Congr., GB, 1948, part 14, pp. 254-269.

Hronsky, J. M. A.; Groves, D. I. 2008. Science of targeting: Definition, strategies, targeting and performance measurement. Aust. J. Earth Sci., 55, 3–12.

Hunting Geology and geophysics Limited. 1961. An airborne geophysical survey of Uganda, Area A (Karamoja). Hunting Surveys Ltd., London.

Hunting Geology and Geophysics Limited. 1980. Mineral Exploration of the Juba Area HGG report to Ministry of Commerce, Industry and Supply, Southern Region Government Democratic Republic of Sudan.

Hunting Geology and Geophysics Ltd, 1979. Mineral Exploration of Juba Area-Final Report

Hunting Geology and Geophysics Limited. 1976. Mineral Exploration in Southern Sudan; Preliminary survey to establish priority areas. HGG report to Ministry of Commerce, Industry and Supply, Southern Region Government Democratic Republic of Sudan.

Hussein, I. M. 1977. Geology of the Halaib area of the northern Red Sea Hills, Sudan, with special reference to the Sol Hamed basic complex. Unpublished M. Phil_ Thesis. Portsmouth Pol chnic, 175 pp.

Ibrahim Ahmad Ali Bany Yaseen. 2018. Geochemical Exploration for Gold and Associated Elements in the Granite Rocks at Wadi Al Marsad, Southwest Jordan. Research Journal of Environmental and Earth Sciences 10(1): 1-15. DOI:10.19026/rjees.10.5853.

Ihaka, R. & Gentleman, R. 1996. R: a language for data analysis and graphics. Journal of Computational and Graphical Statistics 5, 299–344.

Irvine T. N., Baragar W. R. A. 1971. A guide to the chemical classification of the common volcanic rocks. Can J Earth Sci 8:523–548.

Jackson, M. G., Hart, S. R., Koppers, A. A., Staudigel, H., Konter, J., Blusztajn, J., Russell, J. A. 2007. The return of subducted continental crust in Samoan lavas. Nature, 448, 684–687.

James-Smith, J., Cauzid, J., Testemale, D., Liu, W., Hazemann, J.L., Proux, O., Etschmann, B., Philippot, P., Banks, D., Williams, P., Brugger, J., 2010. Arsenic speciation in fluid inclusions using micro-beam X-ray absorption spectroscopy. Am. Mineral. 95, 921–932.

Javhar Aminov, Chen Xi, Bao Anming, Jovid Aminov, Yunus Mamadjanov, Latipa Tuerhanjiang. 2019. Automatic lineament extraction from radar and optical imagery for geological mapping in the Pamir Mountains: a comparative study. Geophysical Research Abstracts Vol. 21, EGU2019-16873.

Jenner, G.A., 1996. Trace element geochemistry of igneous rocks: geochemical nomenclature and analytical geochemistry, in Wyman, D.A., ed. Trace Element Geochemistry of Volcanic Rocks: Applications For Massive Sulphide Exploration: Geological Association of Canada, Short Course Notes, V. 12, p. 51-77.

Jensen, J. R. 1986. Introductory Digital Image Processing: A Remote Sensing Perspective. Prentice-Hall, Englewood Cliffs, New Jersey, USA, 379 p.

Johnson, P. R., Woldehaimanot, B., 2003. Development of the Arabian-Nubian Shield. Perspectives on accretion and deformation in the northern East African Orogen and the assembly of Gondwana. In. Yoshida, M., Windley, B.F., Dasgupta, S. (Eds.). Proterozoic East Gondwana, Supercontinent Assembly and Breakup. Geological Society, London, Special Publication 206, pp. 290–325.

Johnson, P. R., Andresen, A., Collins, A. S., Fowler, A. R., Fritz, H., Ghebreab, W., Kusky, T., Stern, R. J., 2011. Late Cryogenian-Ediacaran history of the Arabian-Nubian Shield: a review of depositional, plutonic, structural, and tectonic events in the

closing stages of the northern East African Orogen. Journal of African Earth Sciences 61, 167–232.

Johnson P. R., Zoheir B. A., Ghebreab W., Stern R. J., Barrie C. T., Hamer R.D. 2017. Gold-bearing volcanogenic massive sulfides and orogenic-gold deposits in the Nubian Shield. SOUTH AFRICAN JOURNAL OF GEOLOGY• Volume 120.1 Page 63-76 • DOI:10.2113/gssajg.120.1.63

Kamenetsky, V. S.; Zelenski, M. 2020. Origin of noble-metal nuggets in sulfide-saturated arc magmas: A case study of olivine-hosted sulfide melt inclusions from the Tolbachik volcano (Kamchatka, Russia). Geology, 48, 620–624.

Kasmin, V. Shiferaw, A. Balcha, T. 1978. The Ethiopian basement: Stratigraphy and possible manner of evolution. - Geol. Rdsch. Stuttgart. Vol. 67 (2): pp. 531-546.

Katumwehe, A. B. Abdelsalam, M. G. Atekwana, E. A. Dávila, L. D. 2015. Extent, Kinematics and Tectonic Origin of the Precambrian Aswa Shear Zone in Eastern Africa. Gondwana Research. http://dx.doi.org/10.1016/j.gr.2015.03.007.

Kazmin, V., Berhe, S. M. and Teffera, M. 1979a. Basement structure of western Ethiopia and its bearing on the pre-Upper Proterozoic tectonic plan in East Africa. Sinet (Eth. J. Sc1.12, (2), 129-36.

Kaufmann, H., 1988. Mineral exploration along the Aqaba–Levant structure by use of TM data; concepts, processing, and results. Int. J. Remote Sensing 9, 1639–1658.

Kebede T, Koeberl C, Koller F. 1999. Geology, geochemistry, and petrogenesis of intrusive rocks of the Wallagga area, western Ethiopia. J Afr Earth Sci.29: 715-734

Kennedy, W. Q., 1964. The structural differentiation of Africa in the Pan-African (±500 m.y.) tectonic episode. Leeds Univ. Res. Inst. Afr. Geol. Annu. Rep. 8, 48–49.

Key, R. M., Charsley, T. J., Hackman, B. D., Wilkinson, A. F. & Rundle, C. C. 1989. Superimposed Upper Proterozoic Collision controlled Orogenies in the Mozambique Belt of Kenya: Precambrian Res. 44, 197–225.

Korshunova, V.A.; Charykova, M. 2019. Mobile Forms of Gold and Pathfinder Elements in Surface Sediments at the Novye Peski Gold Deposit and in the Piilola Prospecting Area (Karelia Region). Minerals, 9, 34.

Kröner, A. Stern, R. J. 2004. Pan-African Orogeny. Encyclopedia of Geology, vol. 1, Elsevier, Amsterdam.

Kröner, A.; Muhongo, S.; Sommer, H.; Vogt, M. 2003. The East African Orogen: Accretion versus Collision. EGS - AGU - EUG Joint Assembly, Abstracts from the meeting held in Nice, France.

Kröner, A., 1977. The Precambrian geotectonic evolution of Africa: € plate accretion vs. plate destruction. Precambrian Research 4, 163–213.

Kujjo, C. P., 2010. Application of remote Sensing for gold exploration in the Nuba Mountains, Sudan. MSc Thesis, Bowling Green State University. Unpublished.

Kujjo, C. P. 2019. Mineral Exploration and Sustainable Development: A Case study in the Republic of South Sudan. Theses and Dissertations--Earth and Environmental Sciences. 64.

Kusky, T.M., Ramadan, T.M, 2002. Structural controls in the Neoproterozoic Allaqi suture: an integrated field, Landsat TM, and radar C/X SIR SAR images. Journal of African Earth Sciences 35, 107–121.

Küster D, Liégeois J. P, Matukov D, 2008. Zircon geochronology and Sr, Nd, Pb isotope geochemistry of granitoids from Bayuda Desert and Sabaloka (Sudan): evidence for a Bayudian event (920-900 Ma) preceding the Pan-African orogenic cycle (860-590 Ma) at the eastern boundary of the Saharan Metacraton. Precambrian Res 2008; 164: 16-39.

Kwaku, S. A., 1986. Geochemical Analysis and Interpretation of Stream Sediments Data from Southern Sudan. M. Sc. Thesis, Brussels University.

Langford, R. L., 2015. Temporal merging of remote sensing data to enhance spectral regolith, lithological and alteration patterns for regional mineral exploration. Ore Geol. Rev., 68, 14– 29.

Large R. R., Danyushevsky L.V., Hollit C., Maslennikov V., Meffre S., Gilbert S., Bull S., Scott R., Emsbo P., Thomas H., Foster J.., 2009. Gold and trace element zonation in pyrite using a laser imaging technique: implications for the timing of gold in orogenic and Carlin-style sediment- hosted deposits Economic Geology, 104, pp. 635-668

Lattin, J.M., J.D. Carroll and PE Green, 2004. Analysing Multivariate Data. Thomson Brooks/Cole, Singapore, Pages: 556.

Lavreau, J. 1974. Etat des connaissances sur les series gneissiques du Haut Zaire Septentrional. Mus. Roy. Afr. Centr. Tervuren (Belg), Dept. Geol. Min. Rapp. Ann. Pp 77-78.

Le Bas, M. J., Le Maitre, R. W., Streckeisen, A., and Zanet tin B., 1986. Chemical Classification of Volcanic Rocks Based on the Total Alkali–Silica Diagram, J. Petrol., vol. 27, pp. 745–750.

Lee. M. Dana; William A Morris; Jeff Harris; G. E. Leblanc. 2010. A network extraction tool for mineral exploration: A case study from the Wopmay Orogen, Northwest Territories, Canada. Journal of Exploration Geophysics 43(2):116-124. DOI: 10.1071/EG11045.

Leggo, P. J., 1974. A geochronology study of the Basement Complex of Uganda. Q. J.I. Geo. Soc. Lond, V. 130 pp 263-277

Leggo, P. J., Aftalion, M. & Pidgeon, R. T. 1971. Discordant zircon U-Pb ages from the Uganda basement. Nature Phys. Sci. 231, 81–84.

Ling Peng; Zhongming Zhao; Linli Cui; Lu Wang., 2004; Remote sensing study based on IRSA Remote Sensing Image Processing System," Geoscience and Remote Sensing Symposium, 2004. IGARSS '04. Proceedings. 2004 IEEE International, vol.7, 4829-4832.

Lundegrrdh, P. H. 1947. Den ultrabasiska gabbron i Roslagen. Sveriges Geol. Unders. C 484.

MacDonald, R., 1961. Explanation of the geology of sheet 36. (Nabilatuk). Rep. Geol. Surv. Uganda No. 5

MacDonald, R. 1955. Preliminary account of the geology of Sheet K IV, NW Karamoja. Geol. Surv. Uganda, Entebbe, Records for 1953.

MacDonald, R. 1961. Explanation of the geology of Sheet 36 (Nabilatuk). Geol. Surv. Uganda, Entebbe, Rept. 6.57 p.

MacDonald, R. 1963a. Compilation Sheet Jinja (1:250 000). Unpubl. Compiled Geol. Map Sheet NA-36-15 Jinja (1:250 000). Geol. Surv. Uganda.

MacDonald, R. 1963b. The Charnockite basement Complex in northern West Nile District, Uganda, and its relations to the Western Rift. Unpubl. PhD. Thesis, Univ. London.

MacDonald, R. 1964a. Charnockites" in the West Nile district of Uganda: A systematic study in the Groves' type area. 22nd Int. Geol. Congr. 13, 227–249.

MacDonald, R. 1964b. Explanation of the Sheets 3, 4, 11 and 12. Geol. Surv. Uganda, Entebbe.

MacDonald, R. 1966. Manuscript map for the geology of Uganda. Unpubl. Report. Dept. Land Surveys, Entebbe.

MacDonald, R. 1967. Rift faulting in the Murchison Falls National Park, Uganda (interim version). Unpubl. Rept. Geol. Surv. Uganda, Entebbe.

Madani, A. A. 2001. Selection of the optimum Landsat Thematic Mapper bands for automatic lineaments extraction, Wadi Natash area, South-eastern Desert, Egypt. 6.

Marsh, J. S., 1991. REE Fractionation and Ce Anomalies in Weathered Karoo Dolerite. Chemical Geology, 190: 189–194

Mars, J. C. and Rowan, L. C. 2006. Regional Mapping of Phyllic- and Argillic-Altered Rocks in the Zagros Magmatic arc, Iran, Using Advanced Spaceborne Thermal Emission and Reflection Radiometer (ASTER) Data and Logical Operator Algorithms. Geosphere, 2, 161-186.

Mathew Tagwai Gregory and Ariffin Kamar Shah, 2018. Remote Sensing Technique for Lineament Extraction in Association with Mineralisation Pattern in Central Belt Peninsular Malaysia. Journal of Physics Conference Series 1082(1):012092. DOI: 10.1088/1742-6596/1082/1/012092.

McCall, G. J. H., 1964. The geology of the Sekerr area. Rep. Geol. Surv. Kenya, 65.

McClenaghan, M.B. 2005. Indicator mineral methods in mineral exploration. Geochem. Explor. Environ. Anal. 5, 233–245.

McClenaghan, M.B.; Cabri, L.J. 2011. Review of gold and platinum group element (PGE) indicator minerals methods for surficial sediment sampling. Geochem. Explor. Environ. Anal. 11, 251–263.

McDonough, W.F. and Sun, S.-S. 1995. Composition of the Earth. Chemical Geology 120: 223-253. doi: 10.1016/0009-2541(94)00140-4.

Meibom, A., & Anderson, D. L. 2004. The statistical upper mantle assemblage. Earth and Planetary Science Letters, 217, 123–139.

Whitehouse, M.; Sakellaris, G. 2016. Boron, sulphur and copper isotope systematics in the orogenic gold deposits of the Archaean Hattu schist belt, eastern Finland. Ore Geol. Rev. 77, 133–162.

Mikucki, E. J., 1998. Hydrothermal transport and depositional processes in Archean lode gold systems: a review. Ore Geol. Rev. 13, 307–321.

Middlemost, E. A. K. 1994. Naming Materials in the Magma/Igneous Rock System. Earth-Science Reviews, 37, 215-244. http://dx.doi.org/10.1016/0012-8252(94)90029-9.

Mohamed G. Abdelsalama, Jean-Paul Lie'geois, Robert J. Stern, 2002. The Saharan Metacraton. Journal of African Earth Sciences. Vol. 34 pp 119–136

Morgan W. J. 1972. Plate motions and deep mantle convection. In Studies in Earth and Space Sciences, ed. R Shagam, RB Hargraves, WJ Morgan, FB Van Houten, CA Burk, et al., pp. 7–22. Boulder, CO: Geol. Soc. Am.

Molnár, F.; Mänttäri, I.; O'Brien, H.; Lahaye, Y.; Pakkanen, L.; Bo, J.; Käpyaho, A.; Sorjonen-Ward, P.

Morey A. A, Tomkins A. G, Bierlein F. P, Weinberg R. F, Davidson G. J. 2008. Bimodal distribution of gold in pyrite and arsenopyrite: examples from the Archean Boorara and Bardoc shear systems, Yilgarn Craton, Western Australia. Econ Geol 103:599–614

Mosley, P. 1993. Geological evolution of the late Proterozoic "Mozambique Belt" of Kenya. Tectonophysics 221, 223–250.

Mumin, A. H., Fleet, M. E., Chryssoulis, S. L., 1994. Gold mineralisation in As-rich mesothermal gold ores of the Bogosu-Prestea mining district of the Ashanti Gold Belt, Ghana: remobilization of "invisible" gold. Miner. Deposita 29 (6), 445–460.

Munyati, C., 2004. Use of Principal Component Analysis (PCA) of remote sensing images in wetland change detection on the Kafue Flats, Zambia. Geocarto Int., 19: 11-22.

Nakamura, N. 1974. Determination of REE, Ba, Fe, Mg, Na and K in carbonaceous and ordinary chondrites. Geochimica et Cosmochimica land, Acta 38, 757–773.

NASA. Available from: htp://www2.jpl.nasa.gov/srtm/

Nex Paul, 2017.

Niu, Y., & O'Hara, M. J. 2003. Origin of ocean island basalts: A new perspective from petrology, geochemistry, and mineral physics considerations. Journal of Geophysical Research: Solid Earth, 108(B4), 2209–2227.

Niu, Y., & O'Hara, M. J. 2009. MORB mantle hosts the missing Eu (Sr, Nb, Ta and Ti) in the

continental crust: New perspectives on crustal growth, crust–Mantle differentiation and chemical structure of oceanic upper mantle. Lithos, 112, 1–17.

Nude, P. M.; Asigri, J. M.; Yidana, S. M.; Arhin, E.; Foli, G.; Kutu, J. M. 2012. Identifying Pathfinder Elements for Gold in Multi-Element Soil Geochemical Data from the Wa-Lawra Belt, Northwest Ghana: A Multivariate Statistical Approach. Int. J. Geosci. 3, 62–70.

Nyakecho, C. Hagemann S. G. 2014. An overview of gold systems in Uganda. Australian Journal of Earth Sciences 61. 59-88. DOI: 10.1080/08120099.2013.831773.

Oberthür, T., Weiser, T., Amanor, J.A., and Chryssoulis, S.L., 1997. Mineralogical siting and distribution of gold in quartz veins and sulphide ores of the Ashanti mine and other deposits in the Ashanti belt of Ghana: Genetic implications: Mineralium Deposita, v. 32, p. 2–15.

Omer Adam M Gibla, Mohammed Ahmed Hassan El-Tayeb, Abd EL-Salam Abdalla Dafa Alla, Esraa Omer Adam Mohammed., 2016. Groundwater salinity in bara basin. International Journal of Multidisciplinary Research and Development. Vol 3; Issue 6; P. 57-64

Omwenga, B. 2018. Use of Space-borne imageries in Mapping of Hydrothermal Alteration Zones and Geological Structures in the Eburru Geothermal Complex, Kenya. 14.

Pacifici, F.; Longbotham, N.; Emery, W. J. 2014. The Importance of Physical Quantities for the Analysis of Multitemporal and Multiangular Optical Very High Spatial Resolution Images". IEEE Transactions on Geoscience and Remote Sensing. 52 (10): 6241–6256. Bibcode:2014ITGRS.52.6241P. doi:10.1109/TGRS.2013.2295819.

Paul Makenzi, 2005. Natural Resource Management in the Didinga Hills: A Baseline Study from Budi County, South Sudan. DCG Report No. 39. P. 66

Pazand, K.; Hezarkhani, A.; Ataei, M.; Ghanbari, Y. 2011. Application of multifractal modelling technique in systematic geochemical stream sediment survey to identify copper anomalies: A case study from Ahar, Azarbaijan, Northwest Iran. Chem. der Erde Geochem., 71, 397–402.

Pearce, J. A., 2008. Geochemical fingerprinting of oceanic basalts with applications to ophiolite classification and the search for Archean oceanic crust. Lithos 100, 14-48.

Pearce, J. A., Harris, N. B., Tindle, A. G., 1984. Trace element discrimination diagrams for the tectonic interpretation of granitic rocks. J. Petrol. 25, 956–983.

Pearce, J. A., 1975. Basalt geochemistry used to investigate past tectonic environment in Cyprus: Tectonophysics, v. 25, p. 41-67.

Pearce, J. A. & Cann, J. R. 1973: Tectonic setting of basic volcanic rocks determined using trace element analyses. Earth Planet. Sei. Letters 19, 290-300.

Peccerilo, A., Taylor, S.R., 1976. Geochemistry of Eocene calc-alkaline volcanic rocks from Kastamonu area, Northern Turkey. Contributions to Mineralogy and Petrology, 58, Pp. 63-81.

Peter R. Johnson & Beraki Woldehaimanot, 2003. Development of the Arabian-Nubian Shield: perspectives on accretion and deformation in the northern East African Orogen and the assembly of Gondwana. Geological Society, London, Special Publications, vol. 206, pp. 289-325.

Petters, S. W. 1991. Regional geology of Africa. Lecture notes in Earth Sciences. Springer-Verlag. Berlin Heidelberg. ISBN 3-540-54528-X. pp. 722.

Phillips G. N, Evans K. A. 2004. Role of CO2 in the formation of gold deposits. Nature. 429:860–863.

Phillips, G. N., and Powell, R. 2010. Formation of Gold Deposits: a Metamorphic Devolatilization Model. J. Metamorph. Petrol. 28, 689–718. doi:10.1111/j.1525- 1314.2010.00887.x.

Phillips, G. N., and Powell, R. 2009. Formation of Gold Deposits: Review and Evaluation of the Continuum Model. Earth-Science Rev. 94, 1–21. doi:10.1016/ j. earscirev.2009.02.002.

Pierre-Simon Ross; Jean H. Bédard. 2009; Magmatic affinity of modern and ancient subalkaline volcanic rocks determined from trace-element discriminant diagrams. Canadian Journal of Earth Sciences., Vol. 44. P 11 https://doi.org/10.1139/E09-054

Pieter Vermeesch; Victoria Pease. 2021. A genetic classification of the tholeiitic and calc-alkaline magma series.

Pin, C., Poidevin, J. L., 1987. U–Pb zircon evidence for a Pan African granulite facies metamorphism in the Central African Republic. A new interpretation of the high-grade series of the northern border of the Congo Craton. Precambrian Research 36, 303–312.

Pitcairn IK, Craw D, Teagle DAH. 2015. Metabasalts as sources of metals in orogenic gold deposits. Miner Depos. 50:373–390.

Pitcairn K. 2011. Background concentrations of gold in different rock types. Appl Earth Sci. 120:31–38.

Pitfield, E. J. P., Stylesn, T. M., Taylorn, D.C., Keyn, M. R., Bauern, W., Ralisonn, A. V., 2009. Gold deposit styles and placer gold characterisation in northern and east-central Madagascar. In: Conference Paper Conference: 10th Biennial SGA Meeting at: Townsville, Australia, p. 3.

Plouffe, A. 2001. The glacial transport and physical partitioning of mercury and gold in till: Implications for mineral exploration with examples from central British Columbia, Canada. Geol. Soc. Lond. Spec. Pub, 185, 287–299.

Pohl, W. & Horkel, A.D. 1980. Notes on the geology and mineral resources of the Mtito Andei - Taita area (southern Kenya). - Mitt, oesterr. geol. Ges. Vienna. 73: 135-152.

Pour, A. B., Hashim, M., Makoundi, C., and Zaw, K. 2016. Structural Mapping of the Bentong-Raub Suture Zone Using PALSAR Remote Sensing Data, Peninsular Malaysia: Implications for Sediment-hosted/Orogenic Gold Mineral Systems Exploration: Structural mapping of the Bentong-Raub Suture Zone, Malaysia. Resour Geol v.66, p.368-385. https://doi.org/10.1111/rge.12105.

Pour, A. B. and Hashim, M., 2014. Alteration Mineral Mapping using ETM+ and Hyperion Remote Sensing Data at Bau Gold Field, Sarawak, Malaysia. In IOP Conference Series: Earth Environ. Sci., 18, 12–149.

Pour, A. B., Hashim, M., 2012. The application of ASTER remote sensing data to porphyry copper and epithermal gold deposits. Ore Geol. Rev. 44, 1–9.

Price, R. C. 1984. Late Precambrian mafic-ultramafic complexes in Northeast Africa. Unpublished PhD thesis. the Open University. Milton Keynes, pp 325.

Prost, G. L., 2002. Remote Sensing for Geologists: A Guide to Image Interpretation, CRC Press, 2002, 2nd edn.

Rajendran, S., Nasir, S., 2014a. Hydrothermal altered serpentinized zone and a study of Ni magnesioferrite–magnetite–awaruite occurrences in Wadi Hibi, Northern Oman Mountain: discrimination through ASTER mapping. Ore Geol. Rev. 62, 211–226.

Rajendran, S., Nasir, S., 2014b. ASTER spectral sensitivity of carbonate rocks—study in Sultanate of Oman. Adv. Space Res. 53, 656–673.

Rajendran, S., Nasir, S., 2014c. ASTER mapping of limestone formations and study of caves, springs, and depressions in parts of Sultanate of Oman. Environ. Earth Sci. 71, 133–146.

R Development Core Team. 2005. R: a language and environment for statistical computing. Vienna: R Foundation for Statistical Computing. http://www.R-project.org.

Ren, D. and Abdelsalam, M. G., 2001. Optimum index factor (OIF) for ASTER data: examples from the Neoproterozoic Allaqi Suture, Egypt. Proc. Geol. Soc. Am., p. 123.

Reich, M., Becker, U. 2006. First-principles calculations of the thermodynamic mixing properties of arsenic incorporation into pyrite and marcasite. Chemical Geology 225, 278–290.

Reich, M., Kesler, S.E., Utsunomiya, S., Palenik, C.S., Chryssoulis, S.L., Ewing, R.C., 2005. Solubility of gold in arsenian pyrite. Geochim. Cosmochim. Acta 69, 2781–2796.

Ries, A., Vearncombe, J.R., Price, R.C., Shackleton, R.M., 1992. Geochronology and geochemistry of the rocks associated with a late Proterozoic ophiolite in West Pokot, NW Kenya. J. Afr. Earth Sci. 14 (1), 25-36.

Ries, A. C., Shackleton, R. M., Graham, R. H. and Fitches, W. R. 1983. Pan African structures, ophiolites, and melange in the Eastern Desert of Egypt: a traverse at 26° N. J. Geol. Soc. Lond. 140,75-95.

Richards, J. A. 2022. Remote Sensing Digital Image Analysis. Springer Cham. Sixth Edition. Pages 263-367 DOI https://doi.org/10.1007/978-3-030-82327-6

Richards, J. A. 2013. Remote sensing digital image analysis: an introduction, Fifth edition. Springer, Berlin.

Richards, J. P. 2011. Magmatic to hydrothermal metal fluxes in convergent and collided margins. Ore Geol. Rev., 40, 1–26.

Roberts, S., Gunn, G., 2014. Cobalt, in: Gunn, G. (Ed.), Critical Metals Handbook. John Wiley & Sons, Ltd., pp. 122–149. https://doi.org/http://doi.wiley.com/10.1002/ 9781118755341.

Rollinson Hugh R. 1993. Using Geochemical data: Evaluation, presentation, and interpretation. Longman Scientific and technical- John Wiley and Sons, Inc., New York

Rollinson Hugh, Pease, Victoria. 2021. Using Geochemical Data To Understand Geological Processes. Cambridge University Press. Second Edition. pp 1- 177. https://doi.org/10.1017/9781108777834.

Rowan, L.C., Wetlaufer, P.H., Goetz, A.F.H., Billingsley, F.C., Stewart, J.H., 1974. Discrimination of rock types and detection of hydrothermally altered areas in south central Nevada by the use of computer enhanced ERTS images. U.S. Geol. Surv. Prof. Pap. 883, 35.

Rowan L. C, Goetz AFH, Ashley R. P. 1977. Discrimination of hydrothermally altered and unaltered rocks in visible and near infrared multispectral images. Geophy., 42 (3): 522–535.

Rowan, L. C., Goetz, A. F.H., Ashley, R.P., 1979. Discrimination of hydrothermally altered and unaltered rocks in the visible and near infrared. Geophysics 42, 533–535.

Rowan, L. C., Trautwein, C. A., Purdy, T. L., 1991. Maps showing association of linear features and metallic mines and prospects in the Butte 18 by 28 quadrangle, Montana. U.S. Geol. Surv. Misc. Invest. Ser. Map I-2050-B.

Rowan C. Lawrence.; Simon J. Hook, Michael J. Abrams.; John C. Mars. 2003. Mapping Hydrothermally Altered Rocks at Cuprite, Nevada, using the Advanced Spaceborne Thermal Emission and Reflection Radiometer (ASTER), A New Satellite-Imaging system. Economic Geology. Scientific Communications. Vol. 98, 2003, pp. 1019–1027.

Rudnick, R. L. 1992. Restites, Eu anomalies and the lower continental crust. Geochimica et Cosmochimica Acta, 56, 963-970. https://doi.org/10.1016/0016-7037(92)90040-p

Sabins, F. 1999. Remote Sensing for mineral exploration, Ore Geology Review, 14, 157-183 Sploos, L.L. & Speed, RC 1974. Relationship of cratonic and continental margin tectonic episodes. In:

Dickinsen, E. (Ed): Tectonics and sedimentation. Spec. Publ. Soc. Econ. Paleont. Min., 22, 98 - 119.

Sabins, F., 1997. Remote Sensing: Principles and Interpretation, third ed., 494pp

Saggerson, E. P. & Turner, L. M. 1972 24th Inst. Geol. Congr. Montrea Satyanarayana Chanagala, Appala Raju Uppala, Yedukondalu Kamatham and M. Ravi Kumar., 2012; Information Extraction through Multispectral Data processing in Remote Sensing Image Evaluation‖, International Journal of Graphics & Image Processing, Vol. 2, issue 3, pp:224-228, ISSN: 2249 – 5452.

Sanislav, I. V., Braysh aw, M., Kolling, S. L., Dirks, P. H. G. M., Cook, Y. A. and Blenkinsop, Thomas ORCID: https://orcid.org/000 0-0 0 0 1-9 6 8 4-0 7 4 9 2 0 1 7. The structural history and mineralization controls of the world-class Geita Hill gold deposit, Geita Greenstone Belt, Tanzania. Mineralium Deposit a 5 2 (2), p p. 2 5 7-2 7 9. 1 0.1 0 0 7/s0 0 1 2 6-0 1 6-0 6 6 0-1 file

Schoneveld, L. and O'Neill, H. S. C. 2019. The influence of melt composition on the partitioning of trace elements between anorthite and silicate melt. Contributions to Mineralogy and Petrology, 174, 13. https://doi.org/10.1007/s00410-019-1548-8

Schowengerdt, Robert. 2007. Remote Sensing: Models and Methods for Image Processing. Elsevier Inc. p. 337. ISBN 0-12-369407-8.

Sedrettea, S. and Rebaïb, N. 2016. Automatic extraction of lineaments from Landsat ETM+ images and their structural interpretation: Case Study in Nefza region (Northwest of Tunisia). J Res Environ Earth Sci v.4, p.139-145.

Shackleton, R. M. 1979. Precambrian tectonics of northeast Africa. In: Evolution and Mineralisation of the Arabian-Nubian shield. Vol 2, pp. 1-6. Pergamon Press. (Inst. Appl. Geol. Bull. 3, 1.6.)

Shackleton, R. M. 1986. Precambrian collision tectonics in Africa. In: Collision tectonics Geol. Soc. London, Spec. Publ. 19, 329–349.

Shackleton, R. M. 1993. Tectonics of the Mozambique Belt in East Africa. Geol. Soc. London, Spec. Publ. 76, 345–362.

Shackleton, R. M. 1994. The final collision zone between East and West Gondwana, where is it? J. Afr. Earth Sci. 23, 271–287.

Shackleton, R. M. & Ries, A. C. 1984. The relation between regionally consistent stretching lineations and plate motions. J. Struct. Geol. 6, 111–117.

Shackleton, R. M., Ries, A. C., Graham, R. M. and Fitches, W. R. 1980. Late Precambrian ophiolitic melanges in the eastern desert of Egypt. _Nature 285,472-74

Shahtahmassebi A., Yang N., Wang K., Moore N., Shen Z., 2013. Review of shadow detection and de-shadowing methods in Remote Sensing. Chin. Geogr. Sci. Vol,23: Pp 403–420.

Shand, S. J., 1943. The eruptive rocks: 2nd edition, John Wiley, New York, 444 p.

Shanti M, Roobol MJ. 1979. A late Proterozoic ophiolite complex at Jabal Ess in northern Saudi Arabia. Nature 279:488 91.

Schwartz, G. M. 1944. The host minerals of native gold, Economic Geology, 39 (6): 371-411.

Shawky, Mahinaz M. El Arafy., Reda, El Zalaky. Mohamed., Elarif Taha. 2019. Validating (MNF) Transform to Determine the Least Inherent Dimensionality of ASTER Image Data of Some Uranium Localities at Central Eastern Desert, Egypt. Journal of African Earth Sciences vol. 149, pp. 441–450.

Si Mhamdi, H., Raji, M., Maimouni, S., and Oukassou, M., 2017. Fractures network mapping using remote sensing in the Paleozoic massif of Tichka (Western High Atlas, Morocco). Arab J Geosci v.10: https://doi.org/10.1007/s12517-017-2912-5.

Smith, C. G., 2001. Always the bridesmaid, never the bride: cobalt geology and resources. Transactions of the Institution of Mining and Metallurgy Section B-Applied Earth Science 110, B75–B80. https://doi.org/10.1179/aes.2001.110.2.75.

Simmons, S. F.; Brown, K. L. 2006. Gold in magmatic hydrothermal solutions and the rapid formation of a giant ore deposit. Science 2006, 314, 288–291.

Smythe D. J, Brenan J. M. 2015. Cerium oxidation state in silicate melts: combined fO2 temperature and compositional effects. Geochim Cosmochim Acta 170:173–187

Stern, R. J., Nielsen KC, Best E, Sultan M, Arvidson RE, Kröner A. 1990. The orientation of late Precambrian sutures in the Arabian-Nubian shield. Geology 18:1103 6.

Stern, R. J., 1994. Arc assembly and continental collision in the Neoproterozoic East African Orogen — implications for the consolidation of Gondwanaland. Annual Reviews of Earth and Planetary Sciences 22, 319–351.

Stern, R. J., 2002. Crustal evolution in the East African Orogen: a neodymium isotopic perspective. Journal of African Earth Sciences 34, 109–117.

Stern, R. J. 2004. Subduction Initiation: Spontaneous and Induced. Earth Planet. Sci. Lett. 226, 275–292.

Sultan, M., Arvidson, R. E., Sturchio, N. C., 1986. Mapping of serpentinites in the Eastern Desert of Egypt using Landsat Thematic Mapper data. Geology 14, 995–999.

Sun, S.-s., and McDonough. W. F., 1989. Chemical and isotopic systematics of oceanic basalts: implications for mantle composition and processes. Geological Society, London, Special Publications 1989; v. 42; p. 313-345. doi:10.1144/GSL.SP.1989.042.01.19.

Sung, Y.-H., Brugger, J., Ciobanu, C.L., Pring, A., Skinner, W., Nugus, M., 2009. Invisible gold in arsenian pyrite and arsenopyrite from a multistage Archaean gold deposit: Sunrise Dam, Eastern Goldfields Province, Western Australia. Mineralium Deposita 44, 765–791. http://dx.doi.org/10.1007/s00126-009-0244-4

Sutherland, D. G. 1985. Geomorphological controls on the distribution of placer deposits. J. geol. Soc. London, Vol. 142, 1985, pp. 727-737, 5 figs. Printed in Northern Ireland.

Tomkins, A. G. 2013. On the source of orogenic gold. Geology 41, 1255–1256.

Tadesse. S, 1999; Geology and Gold Mineralization in the Pan African Rocks of the Adola Area, Southern Ethiopia. Gondwana Research, V. 2, No. 3, pp. 439-447

Tang Wenchun and Zhu Huipai. 2008. The geochemical characters and genesis of trace elements in epithermal minerals from the Xinkongmao Gold Deposit [J]. Journal of Mineralogy and Petrology. 28, 64−70 (in Chinese with English abstract).

Toteu, S. F., 1990. Geochemical characteristics of the main petrographical and structural units of northern Cameroon: implication for Pan-African evolution. Journal African Earth Sciences 4, 615– 624.

Toteu, S. F., Michard, A., Bertrand, J. M., Rocci, G., 1987. U/Pb dating of Precambrian rocks from the northern Cameroon, orogenic evolution, and chronology of the Pan-African belt of central Africa. Precambrian Research 37, 71–87.

Toteu, S. F., Van Schmus, W. R., Penaye, J., Nyobe, J. B., 1994. U-Pb and Sm-Nd evidence for Eburnian and Pan-African high-grade metamorphism in cratonic rocks of southern Cameroon. Precambrian Research 67, 321–347.

Traore, M., Wambo, J. D.T., Ndepete, C.P., Tekin, S., Pour, A.B., Muslim, A. M., 2020. Lithological and alteration mineral mapping for alluvial gold exploration in the southeast of birao area, central african republic using landsat-8 operational land imager (oli) data. J. Afr. Earth Sc. 170, 103933.

Tsige, L. 2006. Metamorphism and Gold Mineralisation of the Kenticha-Katawicha Area: Adola Belt, Southern Ethiopia. Journal of African Earth Sciences, 45, 16-32. https;//doi.org/10.1016/j.jafrearsci.2006.01.002

University of Maryland Institute for Advanced Computer Studies. 2008. Atmospheric Correction. Archived from the original on 7 September 2008.

Vail, J. R. 1976. Location and geochronology of the igneous ring complexes and related rocks in northeast Africa. Geol. Jb., B 20, page 97-114

Vail, J. R., 1978. Outline of the geology and mineral deposits of the Democratic Republic of Sudan and adjacent areas. Overseas Geol. Miner. Resour. London, 49, p. 1-67.

Vail, J. R., 1983. Pan-African crustal accretion in north-east Africa. Journal of African Earth Sciences, Vol. I, No. 3/-t, pp. 285 to 29.

Vail, J. R. 1985. Relationship between tectonic terrains and favourable metallogenic domains in the central Arabian-Nubian shield. Trans. Instn. Min. Metall. (Sect. B: Appl. earth Sci.), 94: BI-B5.

Vail, J. R., 1988b. Tectonics and evolution of the Proterozoic basement of northeastern Africa. In S. E1 Gaby, R.O. Greiling (eds.). The Pan-African belt of north-east Africa and adjacent areas, pp. 195-226. Braunschweig: Vieweg.

Vail, J. R. 1989a. Whither the Kibaran in NE Africa. IGCP no. 255 Newsletter/Bulletin 2: 93-97.

Vail, J.R. 1989b. Ring complexes and related rocks in Africa. J. Afr. Earth Sci. 8: 19-40.

Vail, J. R., Hughes, D.J., Abdel Magid, A. E. M., Abdel Rahman, E. M. and Toum, I. M. 1986. Geology of southern Blue Nile Province, Sudan. Bulletin of the Geology and Mineral Resources Department, Republic of the Sudan, 37: 1-32.

Vaughan, J. P.; Kyin Aung. 2004. Refractory gold ores in Archaean greenstones, Western Australia: Mineralogy, gold paragenesis, metallurgical characterization and classification. Mineralogical Magazine. Vol. 68(2): pp. 255-277. DOI: 10.1180/0026461046820186.

Vearncombe, J. R. 1983a. A proposed continental margin in the Precambrian of Western Kenya. International Journal of Earth Sciences, Geol. Rundschau 72 (2), 663–670.

Vearncombe, J. R. 1983b. A dismembered ophiolite from the Mozambique Belt, West Pokot, Kenya. J. Afr. Earth Sci. 1 (2), 133–143.

Viola, G., Henderson, I. H. C., Bingen, B., Thomas, R. J., Smethurst, M. A., de Azavedo, S., 2008. Growth and collapse of a deeply eroded orogen: insights from structural, geophysical and geochronological constraints on the Pan-African evolution of NE Mozambique. Tectonics 27, TC5009.

Walsh, J. 1966. Geology of the Karasuk Area. Degree Sheet 18, S. W. Quarter, and Part of Degree sheet 17. S. E. Quarter. Report No. 72. Ministry of Natural Resources, Wildlife, and tourism geological survey of Kenya. Republic of Kenya.

Warden, A. J. Kazmin, V., Kiesel, W. & Pohl, W. 1982. Some geochemical data of the mafic-ultramafic complex at Tulu Dimitri, Ethiopia and their genetic significance. Sitzungsberichten der Osterreichischen Akademie der Wissenschaften Mathem. -naturw, 191-5, 111-131

Wedepohl, K. H. 1978. Handbook of Geochemistry 11, Sections 73, B-G. Springer-Verlag.

Westerhof, A. B. P., Harma, P., Isabirye, E., Katto, E., Koistinen, T., Kuosmanen, E., Lehto, T., M. I. Lehtonen, M. I., Makitie, H., Manninen, T., Manttari, I., Pekkala, Y., Pkki, J., Saalmann, K., Virransalo, P., 2014. Geology and geodynamic development of Uganda with explanation of the 1:1,000,000 scale geological map. Geological Survey of Finland Special Paper 55, 387p.

White, W. M., 2010. Oceanic Island basalts and mantle plumes: the geochemical perspective. Annual Review of Earth and Planetary Sciences, 38(1), 133–160, doi:10.1146/annurev-earth-040809-152450.

White, W. M., 2005. Geochemistry 1st Edition.

Whiteman, A. J. 1971. The Geology of the Sudan Republic. Clarendon Press, Oxford, 290 p. London.

Whiteman, A. J., 1966. Geology and Scenery of Sudan. Sudan Notes and Records, Vol. 47, pp. 137-144 Published by University of Khartoum

Williams C. E. F. 1966. The geological map of Karamoja area, 1:250,000, Department of Geological Survey and Mines, Uganda.

Wilson, M., 1989. Igneous Petrogenesis. Oxford University Press, Oxford.

Winter, John D. (John DuNann). 2001. An introduction to igneous and metamorphic petrology/by John D. Winter. p. cm. Includes bibliographical references and index. ISBN 0-13-240342-0 1.

Wold Svante., Esbensen Kim., Geladi Paul. 1987. Principal Component Analysis. Elsevier Science Publishers B.V., Amsterdam - Printed in The Netherlands. Chemometrics and Intelligent Laboratory Systems, vol. 2, pp. 37-52.

Woodhead, J. D., 1989. Geochemistry of the Mariana arc (western Pacific): Source composition and processes. Chem. Geol. 76, 1–24. doi:10.1016/0009-2541(89)90124-1.

Wyman D. A, Cassidy K. F, Hollings P. 2016. Orogenic gold and the mineral systems approach: Resolving fact, fiction, and fantasy. Ore Geol Rev. 78:322–335.

Xing, Y., Brugger, J., Tomkins, A., Shvarov, Y., 2019. Arsenic evolution as a tool for understanding formation of pyritic gold ores. Geology 47, 335–338. https://doi.org/ 10.1130/G45708.1.

Yibas, B. Reimold, W.U., Anhaeusser, C.R., Koeberl, C. 2003. Geochemistry of the mafic rocks of the ophiolitic fold and thrust belts of southern Ethiopia: constraints on the tectonic regime during the Neoproterozoic (900–700 Ma). Precambrian Research 121 (2003) 157–183.

Youngson, J. H., Craw, D., Falconer, D. M., 2006. Evolution of Cretaceous–Cenozoic quartz-pebble conglomerate gold placers during basin formation and inversion, southern New Zealand. Ore Geology Reviews. 28, 451-474. doi:10.1016/j. oregeorev. 2005.02.004 (this volume).

Yousif. M, Henselowsky. F, Bubenzer. O. 2018. Palaeohydrology and its impact on groundwater in arid environments: Gebel Duwi and its vicinities, Eastern Desert, Egypt. CATENA 171:29–43 https://doi.org/10.1016/j.catena.2018.06.028.

Yuan Jinguo and Niu Zheng. 2008. Evaluation of Atmospheric Correction Using FLAASH. International Workshop on Earth Observation and Remote Sensing Applications. Pp. 06.

Zhang, J.; Deng, J.; Chen, H. Y.; Yang, L. Q.; Cooke, D.; Danyushevsky, L.; Gong, Q.J. 2014. LA-ICP-MS trace element analysis of pyrite from the Chang'an gold deposit, Sanjiang region, China: Implication for ore-forming process. Gondwana Res. 26, 557–575.

Zheng Jie, Yu Dalong, Wu Wenming, and Yang Zhongqin. 2011. Typomorphic characteristics of arsenopyrite in the Bake gold deposit, eastern Guizhou Province [J]. Geoscience. 25, 750−758 (in Chinese with English abstract).

Zhong S., Seltmann R., Qu H., and Song Y. 2019. Characterization of the zircon Ce anomaly for estimation of oxidation state of magmas: a revised Ce/Ce method. Mineral. Petrol., 113, 755–763.

Zindler, A., & Hart, S. 1986. Chemical geodynamics. Annual Review of Earth and Planetary Sciences, 14, 493–571.

Zoheir, B. A., 2012. Microchemistry and stable isotope systematics of gold mineralisation in a gabbro-Ako T. A., Vishiti A., Ateh K.I., Kedia A.C., and Suh C.E., 2015. Mineral Alteration and Chlorite

Geothermometry in Platinum Group Element (PGE)-Bearing Meta-ultramafic Rocks from Southeast Cameroon. J. Geosci. Geomat. 3, 96–108.

Zuo, R. 2011. Identifying geochemical anomalies associated with Cu and Pb–Zn skarn mineralisation using principal component analysis and spectrum–area fractal modelling in the Gangdese Belt, Tibet (China). J. Geochem. Explor., 111, 13–22.

Zuo, R.; Wang, J.; Chen, G.; Yang, M. 2015. Identification of weak anomalies: A multifractal perspective. J. Geochem. Explor., 148, 12–24.

9.1 Appendix II: List of samples and their locations

Latitude	Longitude	Name	Description	none	Thin Section	Geochem-A	Remarks
4° 8' 43.1514"	33° 34' 38.517"	Diorite	DIDI-1				
4° 4' 58.6302"	33° 45' 29.5266"	Syenite	Not sampled				Security Concern
4° 39' 16.5018"	33° 40' 3.8814"	Meta Rhyolite			X	X	
4° 39' 3.855"	33° 39' 42.9978"	Grey Gneiss	Not sampled				Highly weathered
4° 41' 27.1206"	33° 46' 3.0174"	Amphibolite					
4° 43' 1.1964"	33° 45' 51.7212"	Amphibolite					
4° 39' 5.0292"	33° 40' 23.2572"	Marble					
4° 36' 28.8828"	33° 41' 22.7868"	Marble					
4° 36' 27.6618"	33° 41' 24.0786"	Quartzite	B-20				
4° 32' 53.2356"	33° 44' 9.657"	Amphibolite					
4° 32' 56.0472"	33° 44' 20.2704"	Marble					
4° 36' 52.9524"	33° 41' 17.1564"	Marble					
4° 35' 51.0216"	33° 41' 45.2076"	Marble					
4° 35' 48.6306"	33° 41' 49.1742"	Quartzite					
4° 41' 20.5938"	33° 40' 9.7788"	Quartzite	QTZ-1				Amp+Qtz Vein?
4° 39' 11.2134"	33° 39' 51.771"	Schist					
4° 39' 15.642"	33° 39' 52.977"	Meta Rhyolite					
4° 39' 18.7662"	33° 39' 59.85"	Quartz Vein	XX		X		
4° 44' 29.8926"	33° 41' 47.799"	Marble					
4° 44' 2.0538"	33° 42' 57.8442"	Amphibolite					
4° 43' 40.1196"	33° 43' 3.0576"	Schist	B-1		X		Qtz-Felds-Schist
4° 45' 20.9946"	33° 37' 50.7576"	Marble					
4° 41' 29.3928"	33° 45' 59.3814"	Gabbro	B-14		X	X	

4° 32' 5.3226"	33° 39' 20.0118"	Amphibolite					
4° 45' 23.583"	33° 40' 5.16"	Amphibolite Schist			X	X	
4° 45' 23.364"	33° 40' 5.2854"	Amphibolite Schist	AN-1A		X	X	Garnet inclusion
4° 45' 25.5816"	33° 40' 3.7812"	Schist			X		
4° 45' 14.4"	33° 38' 20.0"	Quartzite	B-16				Inclusion of muscovite
4° 45' 13.3668"	33° 38' 22.455"	Amphibolite			X	X	
4° 45' 30.1752"	33° 40' 3.5184"	Schist					
4° 40' 36.5808"	33° 49' 5.4516"	Gneiss	Not sampled				
4° 43' 6.1104"	33° 45' 40.6506"	Chlorite Schist	BUN				
4° 43' 6.5094"	33° 45' 41.1078"	Amphibolite	BUN 2		X	X	porphyritic texture
4° 43' 9.1776"	33° 45' 46.3026"	Talc Schist	Not sampled				Highly weathered
4° 36' 16.9554"	33° 55' 15.9342"	Marble					
4° 34' 38.8992"	34° 0' 4.6188"	Basalt					
4° 34' 25.827"	34° 0' 48.6072"	Basalt					
4° 29' 48.246"	34° 4' 40.2774"	Rhyolite					
4° 38' 5.7588"	33° 52' 40.8138"	Gneiss	Not sampled				
4° 37' 18.5154"	33° 55' 32.9124"	Gneiss	Not sampled				
4° 43' 42.294"	33° 43' 3.3162"	Schist					
4° 39' 16.6098"	33° 39' 53.2584"	Meta Rhyolite					
4° 39' 22.8204"	33° 40' 17.3208"	Amphibolite					
4° 14' 10.5468"	33° 4' 51.6612"	Granulite	IS-2				Isoke
4° 41' 29.3928"	33° 45' 59.3814"	Gabbro	Not sampled				
4° 38' 20.3784"	33° 51' 54.1224"	Marble	A-11		X		
4° 39' 4.734"	33° 40' 23.7174"	Amphibolite	B-10		X	X	
4° 45' 33.8"	33° 40' 08.2"	Meta Rhyolite	AN-1		X	X	Alteration zone
4° 45' 33.8"	33° 40' 08.2"	Meta Rhyolite	B-15		X	X	Alteration zone

4° 33' 03.7"	33° 43' 29.8"	Marble	NA-1				Brown
4° 32' 56.1"	33° 44' 20.3"	Marble	Z-2				Tafoni like texture
4° 36' 52.6"	33° 41' 16.8"	Marble					Tafoni like texture
4° 39' 18.5"	33° 40' 00.8"	Quartz Vein	B-13		X		
4° 13' 56.8"	33° 28' 08.7"	Basalt	LO-2				Lotak hill
4° 13' 56.8"	33° 28' 09.5"	Granulite	LO-1				Lotak hill
4° 35' 48.7674"	33° 41' 48.786"	Quartzite	B-23				Lokwamur
4° 43' 39.2592"	33° 43' 12.2154"	Amphibolite	B-5		X	X	Meta gabbro
4° 36' 28.3926"	33° 41' 24.4212"	Marble	B-21				Lopala
		Basalt	A5				Rhyolite present
		Basalt	A6				
		Basalt	A7				